Alma Mater Studiorum - Università di Bologna

DOTTORATO DI RICERCA IN

CHIMICA

Ciclo 35

Settore Concorsuale: 03/B1 - FONDAMENTI DELLE SCIENZE CHIMICHE E SISTEMI INORGANICI

Settore Scientifico Disciplinare: CHIM/03 - CHIMICA GENERALE E INORGANICA

DESIGN AND CHARACTERIZATION OF POLYMORPHS AND CO-CRYSTALS OF ORGANIC MOLECULAR SEMICONDUCTORS

Presentata da: Inês De Oliveira Martins

Coordinatore Dottorato

Luca Prodi

Supervisore

Enrico Modena

Co-supervisore

Lucia Maini

Esame finale anno 2023

This page intentionally left blank

Que sei eu do que serei, eu que não sei o que sou?
Ser o que penso? Mas penso ser tanta coisa!

– Álvaro de Campos – Tabacaria

This page intentionally left blank

Acknowledgements

This PhD was without a doubt a challenge and an adventure. During these 3 years, I met a lot of people that helped to make this journey more pleasant and for whom I'm very grateful.

First, I would like to thank Polycrystalline and the Molecular Crystal Engineering group in the Department of Chemistry, University of Bologna for receiving me as a PhD student. I am very grateful in particular to the UHMob project, a European Commission-funded H2020-MSCA project since it gave me the opportunity for collaboration and networking, essential to grow as a scientist.

I would like to express my gratitude to my supervisors Dr Enrico Modena and Prof. Lucia Maini for their support and guidance. And for being always present throughout these 3 years to help me and give me advice.

During my PhD, I had the privilege of doing my secondments at TU Graz and at the University of Cambridge and for that, I am thankful to Prof Roland Resel and Prof Henning Sirringhaus.

I am grateful to everyone from the Molecular Crystal Engineering group for always being kind and creating a good environment.

To all my UHMob project colleagues, Priya, Martina, Rahul, Christos, Nicholas, Ann Maria, Federico, Lamiaa, Nemo, Marco, Mindaugas, Kripa, Lucia, and Alessandro thank you for making the project meetings something to look forward to and for all the good and fun memories we created together.

Moving to a new country was easier because of my friends from Bologna, Bhavana, Priya, Nidhi, Stefano and Leo for whom I will be forever grateful. I want to thank Priya for being such a good colleague and friend that always listens to my complaints about everything and nothing and for always being down for a drink and good times, without you everything would have been more difficult. I want to express how very very grateful I am to Nidhi, who was always there for me during the good and the bad times, you made my time in Bologna so much more fun just by being potatoes, thank you for being my friend and my family during these 3 years.

Finally, I want to thank everyone that kept me sane and always supported me, even from afar. Obrigada aos meus manos do coração Mónica e Hugo por me darem tanta força nesta recta final.

Um enorme obrigado aos meus amigos que mesmo longe estiveram sempre perto e me ouviram e apoiaram sempre durante estes 3 anos. Ao Fernas por fazer com que o meu tempo em Cambridge fosse menos solitário e por estar sempre disponível para um episódio de love island, um dia destes abrimos o nosso pub. Ao Chico por todas as palavras de carinho e apoio, se consegui superar este desafio deve-se muito a ti e a toda a força que me deste. E um grande obrigado à Emma, a minha BFF para a vida que me apoia em tudo, me motiva e acredita em mim mais do que eu acredito em mim própria, tudo se torna mais fácil com o teu apoio, não há fuso horário que nos separe.

Por último, quero agradecer muito à minha família, à minha mãe, ao meu pai e à minha irmã que estão sempre presentes e certificam-se sempre que estou bem. Um obrigado muito especial à minha mãe que me dá força para nunca desistir.

Abstract

In the last decades, organic semiconductors (OSCs) have attracted a lot of attention due to their possible employment in solution-processed optoelectronic and electronic devices, such as organic field-effect transistors (OFETs). One of the big advantages of solution processing is the possibility to process into flexible substrates at low cost. Organic molecular materials tend to form polymorphs, which can exhibit very different conductive, luminescent, and mechanical properties. In most cases, the control of the crystal structure is decisive to maximize the performance of the final devices. Although organic electronics have progressed a lot, n-type organic semiconductors still lag behind p-type, presenting some challenges such as air instability and poor solubility.

Bis(naphthalene diimide) (NDI) derivatives are a particularly interesting family of organic materials. NDIs possess high electron affinity, good charge carrier mobility, and excellent thermal and oxidative stability, making them promising candidates for applications in organic electronics, photovoltaic devices, and flexible displays. Recently, the structure-properties relationship and the polymorphism of these molecules have gained considerable attention.

In the first part of this thesis, NDI-C6 thermal behavior was extensively explored which revealed two different thermal behaviors depending on the annealing process. This study allowed to define the stability ranking of the NDI-C6 bulk forms and to determine the crystal structure of Form γ at 54°C from powder. Additionally, the polymorphic and thermal behavior of thin films of NDI-C6 was also explored. It was possible to isolate pure Form α, Form β, and Form γ in thin films and a new metastable form was found, called Form ε. It was also possible to determine the stability ranking of the NDI-C6 crystal phases in thin films. OFETs with bottom gate, top contact geometry were fabricated having different polymorphs as active layer, unfortunately the performance was not ideal mainly due to the bad morphology of the thin films.

During the second part of this thesis, core-chlorinated NDIs with fluoroalkyl chains were studied. Initially, the focus was on the polymorphism of CF_3-NDI that revealed a solvate form with a very interesting molecular arrangement suggesting the possibility to form charge transfer co-crystals. In the last part of the thesis, the synthesis and characterization of CT co-crystal with different NDI

derivatives ($C_3F_7Cl_2$-NDI, $C_3F_7Cl_4$-NDI, CF_3Cl_4-NDI, and $C_4F_9Cl_4$-NDI), and acceptor and as donor BTBT and ditBu-BTBT were explored.

Abbreviations

2D	Two dimensions
2PR	Isopropanol
A	Acceptor
ACN	Acetonitrile
ACT	Acetone
AFM	Atomic force microscopy
ATR-FTIR	Attenuated Total Reflection-Fourier Transform Infrared
BHH-BTBT	Bis(hydroxy-hexyl)[1]benzothieno[3,2-b][1]benzothiophene
BTBT	[1]Benzothieno[3,2-b][1]benzothiophene
CF_3Cl_4-NDI	4,5,9,10-tetrachloro-2,7-bis(2,2,2-trifluoroethyl)benzo[lmn][3,8]phenanthroline-1,3,6,8(2H,7H)-tetraone
$C_3F_7Cl_2$-NDI	N,N′-bis-(heptafluorobutyl) - 2,6 - dichloro - 1,4,5,8-naphthalene tetracarboxylic diimide
$C_3F_7Cl_4$-NDI	4,5,9,10-tetrachloro-2,7-bis(2,2,3,3,4,4,4-heptafluorobutyl)benzo[lmn][3,8]phenanthroline-1,3,6,8(2H,7H)-tetraone
$C_4F_9Cl_4$-NDI	4,5,9,10-tetrachloro-2,7-bis(2,2,3,3,4,4,5,5,5-nonafluoropentyl)benzo[lmn][3,8]phenanthroline-1,3,6,8(2H,7H)-tetraone
CHF	Chloroform
CSD	Cambridge Structural Database
CT	Charge transfer
D	Donor
DCM	Dichloromethane
ditBu-BTBT	2,7-ditert-butyl-[1]benzothieno[3,2-b]benzothiophene
DMF	Dimethylformamide
DMSO	Dimethyl sulfoxide
DSC	Differential Scanning Calorimetry
EGA	Evolved Gas Analysis
ETA	Ethyl acetate

ETH	Ethanol
GIXRD	Grazing incidence X-ray diffraction
H2O	Water
HOMO	Highest occupied molecular orbital
HSM	Hot-stage microscopy
HT	High temperature
LUMO	Lower unoccupied molecular orbital
MET	Methanol
MSPD	Material Science and Powder Diffraction
NDI	Naphthalene tetracarboxylic diimide
NDI-C6	N,N0-bis(n-hexyl)naphthalene-1,4,5,8-tetracarboxylic diimide
NMR	Nuclear magnetic resonance
NTE	Negative thermal expansion
ODTS	Octadecyltrichlorosilane
OFET	Organic field effect transistor
OLED	Organic light emitting diode
OPV	Organic photovoltaic
OSC	Organic semiconductor
PASCal	Principal Axis Strain Calculator
PSD	Position Sensitive Detector
PSI	Paul Scherrer Institute
PTE	Positive thermal expansion
PXY	P-xylene
RFID	Radio frequency identification
RT	Room temperature
SCXRD	Single crystal X-ray diffraction
SIP	Surface-induced phase
SS	Solid solution
TBAF	Tetrabutylammonium fluoride
TGA	Thermogravimetric Analysis

THF	Tetrahydrofuran
TOL	Toluene
VT-XRPD	Variable temperature X-ray powder diffraction
VT-XRR	Variable temperature X-ray reflectivity
XRD	X-ray diffraction
XRPD	X-ray powder diffraction
XRR	X-ray reflectivity

This page intentionally left blank

Table of contents

This page intentionally left blank

Chapter 1: Introduction

Organic semiconductors

Semiconductors are essential in all recent technology, being one of the main materials present in transistors and diodes, which are part of all electronic devices. [1,2] The way we communicate today would not be possible without semiconductors, communication and data processing became easier and faster due to the evolution of semiconductor technology. [2–4] A semiconductor can be easily described as a material with an electrical conductivity between the metals and insulators, its conductivities can vary over several orders of magnitude since it is possible to control it by doping with impurities. Moreover, the electrical conductivity of a semiconductor material increases with increasing temperature, which is a behavior opposite to that of a metal, and it also changes due to the absorption of light. This allows semiconductors to be used for amplification, switching and energy conversion. [2,3]

Current conduction in a semiconductor is obtained by the movement of free electrons and holes and by doping the material, the number of charge carriers, i.e., electrons and holes, greatly increases. When a semiconductor has mainly free holes (hole transporters) it is known as p-type, and when it contains mostly free electrons (electron transporters) it is called n-type. [2,5,6]

The first time these properties were described in a material was in 1833 by Michael Faraday, being the earliest study of semiconductors. Faraday observed the increase of electrical conductivity with the increase of temperature in silver sulfide. [3,7]

From then on, the advances made in micro-electronics allowed a revolution in our day-to-day lives and it is unknown when/if these advances will stop or how will continue to impact our lives in the future.[7] Currently, inorganic semiconductors still are the base of the semiconductor technology, with silicon as the main element since it is a simple semiconductor with easily manipulated properties by proper materials processing, and it has a stable insulating oxide. [7,8] But lately, new fields of organic electronics and optoelectronics using organic semiconductors have arisen, what could possibly have an effect on our lives similar to the introduction of the semiconductor technology due to the new possible applications. [8–10]

The field of organic electronics got a great amount of attention after the Nobel Prize in Chemistry was awarded to Alan J. Heeger, Alan G. MacDiarmid, and Hideki Shirakawa in 2000 for the discovery and development of conductive polymers, more precisely the unprecedent high electrical conductivity of polyacetylene when doped with halogens. [1,9,11,12]

Organic semiconductors have several properties that cannot be achieved with inorganic materials, such as flexibility, transparency, expendability, lightweight, adaptability to low temperature processing, low cost and molecular design to tune electrical properties. [1,8,13,14] These qualities led to a huge interest in research of organic field-effect transistors (OFETs), organic light-emitting diodes (OLEDs) and organic photovoltaic devices (OPVs) and opened the opportunity of new applications and processing. [8,10]

An OFET is a versatile electronic device that amplifies and switches electrical signals, it can be applied to radio-frequency identification tags (RFIDs)/memories, flexible active-matrix displays, electronic paper, electronic skin and chemical/biological sensors. [6,9,10,13,15]

Oppositely to inorganic semiconductors, the solid-state structure of organic semiconductors is based on soft, van der Waals bonding and dipole-dipole interactions between individual molecules. [16–18] Organic semiconductors are π-conjugated systems, i.e., their π-orbitals overlap and form a network of highly delocalized π-systems, this gives them unique electrical and optical properties that can be tuned via structural modifications. Organic semiconductors can be divided in two big families: one based on small molecules or oligomers with well-defined structures, and the second based in highly conjugated polymers. [1,5,8,13,19,20]

Small molecule organic semiconductors have demonstrated high charge carrier mobilities due to their ability to form ordered structures which allows the overlap of the orbitals, being the preferred packing motifs to obtain higher performance the herringbone and 2D π-stacking motifs. Another factor that makes this type of materials attractive is the possibility of being efficiently purified. In contrast, polymers are attractive for large area electronics and have shown high performance in both single-component devices and devices produced with blends. [21]

Small molecule organic semiconductor's structure is normally formed by a π-conjugated core, heteroatoms, substituents, and side chains. The electronic properties can be tuned by varying the conjugated core, heteroatoms, and substituents, while the side chains are important to improve

solubility, which is essential for inexpensive processing techniques by solution methods, but they can also affect the molecular packing or alter the torsion conformation of the core. [10,20]

π-conjugated materials have been in the spotlight of research and a lot of new concepts have been uncovered due to the relationship between molecular structure and their semiconducting properties (π-electronic structure), with the main focus on the study of the band gap energy. [5,19]

The band gap energy represents the energy separation between the highest occupied molecular orbital (HOMO) and the lowest unoccupied molecular orbital (LUMO), in an ideal system the individual HOMO and LUMO energy levels would blend to form bands analogous to the valence and conduction bands of the inorganic semiconductors, respectively. The HOMO and LUMO levels are strongly influenced by the molecular arrangement and packing, consequently the band gap energy can be controlled by crystal engineering. [19,22] Hereupon, the field of organic electronics can be considered the merge of synthetic strategies from organic chemistry to charge transport theories from physics. [1]

Contrarily to inorganic semiconductors that have low band gaps and where free charges can be created by thermal excitation from a valence band to a conduction band, in organic semiconductors the conductivity is extrinsic and comes from the injection of charges at electrodes, by matching the work function of the injecting electrode to the HOMO in the case of hole injection, or in the case of electron injection to the LUMO. The charge transport does not depend on the actual ability of the materials to transport charges but on the ease of charge injection from electrodes. [5,22,23]

Charge transport of molecular semiconductors depends on the ability of the charge carriers to pass from one molecule to another, consequently the charge transport properties are strongly related to their molecular structure, nonetheless it is the packing of individual moieties that determines the overlap of neighboring orbitals and defines pathways for charge transport. [16,18,24]

In organic semiconductors, the charge transport is often defined as a hopping process where the charge carrier mobility is usually thermally activated and the wavefunction of the charge is localized on a single molecule, which can be described by Marcus theory. [18,25,26] In some cases, in high mobility organic semiconductors, carriers can exhibit thermally activated behavior at lower temperature, in other words incoherent hopping transport, and coherent band transport at higher temperatures. [18,21]

The presence of electronic states in the band gap of the organic semiconductors can lead to the formation of traps that will consequently trap the charge carriers and obstruct their transport what will stop the organic semiconductors from reaching their intrinsic mobility. Hereupon it is easy to understand how the charge transport is sensitive to traps within the bulk. In the case of p-type materials the charge transport benefits from their low ionization potential since it makes the thermodynamically unfavorable to fill the traps. On other hand, n-type materials benefit from a large electron affinity which disfavor the filling of the traps. [27,28]

Some widely studied p-type semiconductors include oligoacenes such as pentacene, [29–31] oligothiophenes such as dihexylsexithiophene [32,33] and thienoacenes, such as [1]benzothieno[3,2-b][1]benzothiophene (BTBT)[34,35]. In the case of n-type semiconductors the most prominent material is the family of rylene diimides (RDIs) and their homologues such as pyromellitic diimides (PMIs), 1,4,5,8-naphthalenediimides (NDIs), perylene tetracarboxylic diimides (PDIs). [36,37]

The performance of organic semiconductors, more specifically OFETs performance, has improved enormously in the last decades, with mobilities larger 30 $cm^2V^{-1}s^{-1}$ observed in printed p-type small molecular semiconductors. [6,21,38] However the performance of n-type semiconductors still falls behind when compared with their p-type counterparts, much due to the difficulty in finding n-type semiconductors that have both high charge-carrier mobility and ambient stability. [13,39,40] What makes the search for high performance n-type semiconductors so challenging is the large injection barrier of electron between the work function of conventional metals and the LUMO of the semiconductor and the instability of organic radical anions in the presence of oxygen and water, or various electron traps on the interfaces around a directing channel [41,42] To get an ideal n-type semiconductor it is necessary strong intermolecular orbital overlap, air stability, phase stability, ease of synthesis and high electron affinities to facilitate charge injection, which can be achieved by introducing electron-withdrawing groups or heteroatoms in the molecular structure. Overall, among the most important features for n-type OSCs are LUMO energy levels and morphology of semiconducting film. Nonetheless some of these characteristics are not intrinsic to the material itself, but are strongly influenced by device configuration and processing. [40,41,43]

Naphthalene Diimides

Among the investigated n-type organic materials, those based on rylene diimides (RDIs) have become one of the most promising classes of compounds, since their performance under ambient conditions is close to that of p-type organic semiconductor. There are various classes of RDIs, such as pyromellitic diimides (PMIs), 1,4,5,8-naphthalenediimides (NDIs), perylene tetracarboxylic diimides (PDIs) and other larger diimides (Figure 1). [36,37] Naphtalene diimides are the smallest homologue of the RDIs and possess high electron affinity, a relatively deep lowest unoccupied molecular orbital (LUMO) due to the strong electron withdrawing properties of the imide groups, good charge carrier mobility, and good chemical, photochemical, thermal and oxidative stability, making them promising materials for organic electronics. [44–48]

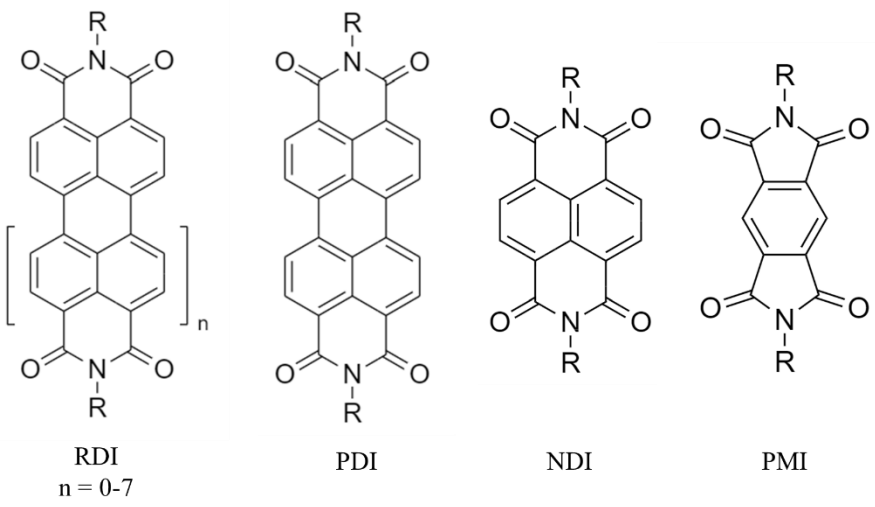

Figure 1 – Chemical structure of various compounds of the rylene diimides family.

The utilization of the RDIs homologues in n-type organic thin film transistors (OTFTs) goes back to 1995 when Dodabalapur et al. published mobilities of ~10^{-3} $cm^2V^{-1}s^{-1}$ for perylene tetracarboxylic dianhydride (PDA). [49] Still in 1995 the group of Horowitz used PDI derivatives as n-type semiconductor in TFTs. [50] The use of NDA as semiconductor in devices was reported in 1996 by Katz, Dodabalapur and coworkers with n-type mobilities of 0.003 $cm^2V^{-1}s^{-1}$. [37,51]

So far, NDIs have proved to be the most successful air-stable n-type material, this is mainly because NDIs are neutral, chemically robust, have high melting points and a planar conjugated bicyclic structure, which leads to strong $\pi - \pi$ interactions. This allowed NDI derivatives to be

used as functional materials since their electronic and physical properties are more suited to applications than PMIs and PDIs. [36,45,52]

All the NDIs derivatives can be easily synthesized from commercially available naphthalene tetracarboxylic dianhydrides (NDAs), which has also been used as a precursor for the production of industrially relevant pigments, making it easy to functionalize this class of aromatic molecules. [39,53] It is well known that the introduction of flexible side chains at the imide nitrogen atoms enables control over physical properties, such as molecular packing, self-assembly capability, and solubility. For this several different types of side chains can be used, namely alkylated, conjugated, ionic and fluoroalkylated side chains This substitution is referred as "side-chain engineering" and it is an important strategy to optimize the performance of solution-processed organic semiconductors, since the active semiconducting components are planar aromatic units that have a strong tendency to aggregate via π-stack making them very poorly soluble. [37,39,44,52]

Nevertheless, until 2000, NDIs had only been functionalized at the imide N-position without chemical modifications at the core positions (X,Y) reported up to that date. However, the situation changed when the Würthner group reported in 2002 core-substituted NDIs (cNDIs) by placing heteroatom substituents at the NDI core (Figure 2). [36,45]

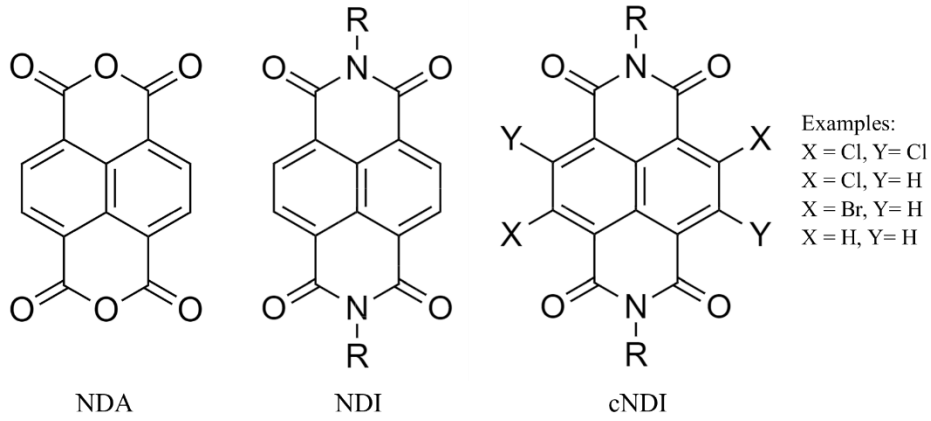

Figure 2 -Chemical structure of aromatic diimide structures.

Core functionalization allows the electronic properties of cNDIs to be tuned by changing the reduction potential and thus LUMO levels can be lowered. In addition, NDI functionalization varies the absorption and emission properties, allowing derivatives to act as either donors or acceptors in a controlled manner. [36,37,44]

Even though NDIs have proved to be among the most promising n-type semiconductors, the electrical performance of OTFTs based on rylene diimides rapidly degrades in air. Generally, air instability is not related to degradation of intrinsically chemically unstable neutral materials but occurs due to the vulnerability of the corresponding radical anions to reaction with atmospheric H_2O or O_2. [48,54]

To improve the ambient stability, two different molecular design strategies can be used. One is by introducing strong electron withdrawing substituents such as -CN, -Cl, -Br and -F in the core region, since these substituents lower the LUMO levels significantly, ideally below the LUMO level of the most atmospheric trapping oxidants, minimizing the atmospheric trapping. This leads to enhancing their resistivity to ambient oxidations by providing an effective barrier for water and oxygen penetration. A low LUMO level also reduces the electron injection barrier, which allows efficient and stable electron injection and transport.[54–58] The other molecular design approach is to introduce fluorinated substituents at the imide nitrogen, such as fluoroalkyl chains, allowing the formation of self-segregated densely packed chains to provide a kinetic barrier to the diffusion of ambient oxidants, preventing moisture and oxygen penetration into the organic layer. The introduction of fluorinated alkyl chains produces a dense molecular packing without disturbing the planarity of $\pi - \pi$ orbital overlap. [39,54,55] In 2000, the group of Katz demonstrated ambient stable n-channel devices with a NDI derivative with fluorinated side chains reaching mobilities greater than 0.1 $cm^2V^{-1}s^{-1}$ and excellent on/off current ratios in the order of 10^5, since then a lot of progress have been done with this class of materials [37,59]

NDIs and their derivatives have been widely used as building block for electronic and optoelectronic devices such as organic light-emitting diodes, supercapacitors, OTFTs and solar cells. [39,44,54,60–62]

Besides the applications in electronic and optoelectronic devices, all the attractive properties of NDI derivatives, especially the possibility of tuning the properties by functionalization of the NDI molecules also makes them a good candidate for several sensing applications. Substituted and water-soluble NDIs have been used as material for selective fluorescence sensing of Cu^{2+} ions and biological thiols in aqueous medium, fluorescent sensors for pH determination in physiological liquids and gas sensors to detect NH_3 and amines have also been explored. [47,63–65]

Polymorphism

The term polymorphism was first used in the context of crystallography by Mitscherlich around 1822, when different crystal structures of the same compound in several arsenate and phosphate salts were recognized. [66–68] Nowadays, the definition accepted by the scientific community is the one described by McCrone. According to McCrone, polymorphism is the ability of any element or compound to crystallize as more than one distinct crystal species. [66,68–70] Different polymorphs have different van der Waals interactions and hydrogen bonds and consequently different free energies what can cause different physical properties such as solubility, chemical stability, melting point, density, etc. These differences are only observed in the solid state and disappear in the melt and vapor state [66,69]

Polymorphism can be divided into two different categories, packing and conformational polymorphism. In packing polymorphism, the molecules have almost the same conformation but are packed into different three-dimensional structures and have different intermolecular interactions. Conformational polymorphism is a mechanism where conformationally flexible molecules can fold into different shapes due to the possible rotation around single bonds in a molecule, leading to different three-dimensional structures. [69,71] In addition, when two different polymorphs crystallize from the same solution under the same conditions, they are called concomitant polymorphs. [71]

The first example of polymorphism in organic compounds was observed in benzamide, for which two different polymorphs were discovered by Liebig and Wohler in 1832. The discovery of the two polymorphs was only based on visual evaluation of the different morphologies between the crystals: needle and block. Interestingly, the crystal structure of the metastable form II of benzamide was determined only in 2005 by powder diffraction since it was not possible to obtain crystals suitable for single crystal X-ray diffraction [67,71–73]

Organic molecules easily exhibit polymorphs but only one form is stable at room temperature and atmospheric pressure and it is important to learn about the relative stability of each phase under different ranges of temperature, pressure and other conditions. [66,74]

The relative stability of polymorphs depends on their free energies, and the one with the lowest free energy at a certain pressure and temperature is termed the thermodynamically stable form

while the other polymorphs are called metastable forms. The metastable forms, that are less stable due to the energy relationship, will be energetically driven to transform into the most stable form, although kinetic factors may prevent the transformation. [66,69,71] To describe the thermodynamic behavior of polymorphs, two types of graphic representation can be used, namely energy-temperature diagrams and pressure-temperature diagrams. For organic molecules the most commonly used is the energy-temperature diagram which considers the stability at atmospheric pressure since it contains a lot of information in a compact form and the data needed to produce it is more easily accessible experimentally. [66,69,74]

Using the diagrams mentioned above, it is possible to distinguish two different polymorphic behaviors: enantiotropic or monotropic, Figure 3. A pair of polymorphs is named enantiotropic when the transition temperature, point which the two polymorphs can undergo solid-solid transformation, is below the melting point of the two polymorphs. Instead, if the transition temperature is above the melting points, we are in the case of the monotropic relation that means one polymorph is more stable at all temperatures below the melting point. In this case the transition point is considered a virtual transition point since it lies above the melting point of both polymorphs. [66,69,71,74]

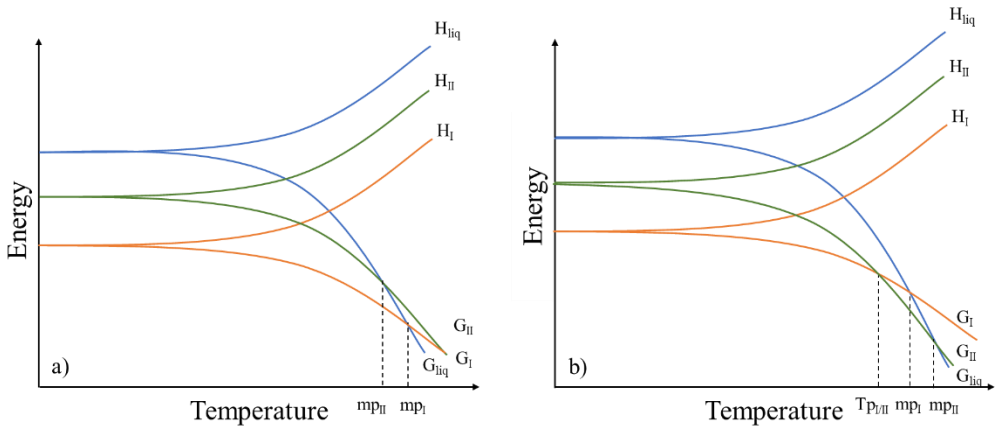

Figure 3 – Energy/temperature diagrams with an example of a) a monotropic system and b) an enantiotropic system. Where G is the Gibbs free energy and H the enthalpy [66]

To determine if the relationship between two polymorphs is monotropic or enantiotropic, thermal characterization such as hot stage microscopy (HSM), differential scanning calorimetry (DSC) or differential thermal analysis (DTA) can be used. [71]

To determine the different crystal structures of the polymorphs single crystal and powder X-ray diffraction (SCXRD and XRPD respectively) are the preferred techniques, but complementary information are obtained by spectroscopy such as, Fourier transform infrared spectroscopy (FTIR), Raman spectroscopy, solid-state nuclear magnetic resonance spectroscopy (ssNMR), atomic force spectroscopy (AFM), scanning electron microscopy (SEM), along with others. [66,69]

To search for polymorphs a broad range of crystallization techniques are used, since different polymorphs are stable in different environments what means that polymorphs can be obtained by adjusting the external conditions. [75,76] The action of searching for polymorphs with different crystallization methods is generally known as polymorph screening. Some of the methods used for crystallization include crystallization from melt and solution crystallization, where several parameters can be changed and explored such as solvents (including solvent mixtures), temperature, stirring, cooling rate, antisolvent, slurrying. [75,77] By identifying the conditions necessary to obtain a specific crystal phase it becomes easier to obtain or avoid the crystallization of a certain polymorph, this control allows to study and explore metastable forms.

Polymorphism is important and has an impact on almost all scientific disciplines since, like mentioned above, different crystal structures will cause different properties of a material. In the case of organic semiconductors, polymorphism can have a huge impact on the charge carrier mobility and because of the difficulty on controlling polymorphism, it is normally considered a disadvantage when these materials show polymorphic behavior and in some cases it leads to abandonment of their study. [53] Nonetheless, in the recent years, polymorphism started to be perceived more as an advantage than a problem, much due to advances made in controlling it, leading to exploitation of new properties of materials and obtaining novel functional materials. [53,67,78]

Surface induced polymorphism

As mentioned before organic semiconductors are widely used in the field of organic electronics and a lot of attention has been put into OFET fabrication. Therefore, it is of great importance to study polymorphism in the thin film geometry since the charge transport mainly happens in the semiconductor-insulator interface within a few molecular layers [34,74,79]

Although polymorphism has been widely studied in bulk, polymorphism in thin films is still poorly understood and a systematic approach to study, identify, and characterize surface induced phases (SIPs) is not yet reported and only a small number of systems have been studied. [74,79–81] Nonetheless, it is known that the surface can play a crucial role during nucleation or crystallization as the surface lowers the activation energy barriers, acting as a catalyst for heterogeneous crystallization, however it should be considered that most of the time the SIPs have a kinetic origin. Moreover, organic molecular materials can crystallize into new crystal forms different from any bulk phase in the proximity of a surface, there are also evidences that surfaces can stabilize metastable phases. [79,82–84] The metastable forms can be trapped during crystallization by varying the parameters used during the crystallization, this is possible because crystallization from solution usually follows Ostwald's rule of stages that states that the solute crystallizing out of a solution will crystallize first as the least thermodynamically stable polymorph, which then converts to the next least stable, and so on to the most stable form. [80]

These new crystal forms, called thin film phases, surface mediated phases or surface-induced phases (SIP) can only be obtained when the material is in contact with a surface. The first observation of SIP phases was in films of pentacene where the SIP, although less energetically favorable than the bulk, is stabilized in the vicinity of a surface. In the case of pentacene different SIPs were also obtained by changing the nature of the substrate. [34,80,84–86] The structural differences between SIPs and bulk phases of π-conjugated molecules are normally related to small changes in the tilt angle, in a manner that the two phases are similar but distinct from each other, and they have been referred as distorted bulk. Recently a more general definition of these phases defines any phase grown at a surface as surface mediated phases, this definition includes the distorted bulk phases, and surface selected phases. Where the surface selected phase does not show a relation with the bulk phases, and it is considered an authentic new structure. [34,81]

SIPs normally contain multiple molecules per unit cell and are present only until a certain film thickness, above that thickness the bulk form grows on top of the SIP, generating a film with two or more coexisting phases. [34,87] Moreover, a SIP extends within the film plane and out-of-plane, meaning that a monolayer structure or surface reconstruction are not considered a substrate-induced polymorph. [88,89]

Thin film crystals are usually prepared by drop casting, spin coating or physical vapor deposition that can promote the growth of different crystal structures. Several parameters such as solvent, concentration of solute and temperature can be varied to explore the possibility of different crystal forms. For example, it has been reported that lower concentration and/or higher temperatures normally lead to a less densely packed structure. [84,90,91] In addition, interfaces and surfaces can also influence the crystal structure obtained and due to this reason several strategies to control morphology and polymorphism of the thin-films have been created, such as nanoscale confinement, lateral confinement, epitaxially grown monolayers used as template, solution shearing and partial de-wetting. [80,92] Several post deposition treatments have also been used to control polymorphism in thin films, such as solvent annealing or thermal annealing. [79]

To solve the crystal structures of surface mediated phases it is quite difficult since the conventional single crystal or powder X-ray diffraction methods cannot be applied while successful results have been reported for grazing incidence X-ray diffraction (GIXRD). Nevertheless, solving crystal structures by GIXRD can be challenging because the amount of scattering material in the sample is small what causes a weak signal to noise ratio, and it is not as straightforward to index the peaks as in the case of bulk and single crystal Bragg reflections. [29,88]

GIXRD is a method for studying the structure and composition of thin films and surfaces by analyzing the diffraction patterns produced when X-rays are scattered at a shallow angle of incidence. In GIXRD, the X-rays penetrate the material at a shallow angle, grazing the surface, and interacting with the atoms in the top few layers, producing diffraction patterns that reveal information about the film's crystal structure, orientation, and roughness.

Additionally, surface-enhanced Raman spectroscopy and computational approaches such as molecular dynamics simulations (MD) have been combined with GIXRD to obtain the structural information of SIPs. [74,93]

Charge transfer complexes

Organic charge-transfer (CT) complexes are multicomponent systems with a specific stoichiometric ratio consisting of an electron rich donor (D) and an electron deficient acceptor (A), which normally are unipolar semiconductors in their pristine form.[94,95] Within the complex, the HOMO and LUMO levels are offset to promote a transfer of charge from the D to the A, creating a hybrid band structure and resulting in a smaller effective bandgap and partial ionicity. The transfer of charge from D to A is the process responsible for the formation of a D–A pair. [95,96]

Charge transfer transition is derived from the electronic coupling between the HOMO of D and the LUMO of A, and can be characterized by the degree of charge transfer (ρ), that can range from neutral (ρ = 0) to the fully ionized form (ρ = 1) and it greatly depends on the overlap between the frontier molecular orbitals (FMO) of the D and A and also on their chemical structure. [94,97]

Recently molecular CT co-crystals of donor and acceptor OSCs have attracted much attention as an optoelectronic material with applications as ambipolar organic field effect transistors (which can transport holes and electrons simultaneously), biocomponent ferroelectrics, photoconductors, [98] strain sensors, [99] light detectors [100] and photovoltaics. [101,102] However, this type of materials is not new and they were firstly studied focusing on metallic high conductivity or superconductivity originating from organic CT salts. [102,103] The ambipolar transport behavior was only first discovered in 2004 by T. Hasegawa et al in bis(ethylenedithio)tetrathiafulvalene (BEDT-TTF) - 2,5-difluoro- 7,7,8,8-tetracyanoquinodimethane (F2TCNQ) co-crystal at low temperature. [104,105] Then in 2012, Brèdas and co-workers first predicted the ambipolar charge-transport in in dibenzotetrathiafulvalene (DBTTF) – tetracyanoquinodimethane (TCNQ) complex by theoretical calculations, in the following year Pan et al. proved it experimentally. Hu et al. reported that the molar ratio of cocrystal (perylene:TCNQ 1:1) shows n-type behavior, while the other stoichiometric cocrystal (perylene:TCNQ 3:1) exhibits ambipolar. [102,103]

The CT co-crystals self-assemble into crystalline or supramolecular structures and usually show significantly different and novel physical properties rather than the simple combination of the properties of the corresponding pristine components. [106] However developing and controlling the self-assembly of such supramolecular materials is challenging since the donor and acceptor molecules can have different and low solubility which promote the self-aggregation separately instead of D-A cocrystal. Moreover, structural mismatch between different components can also

represent a big challenge. [102,106–108] Some strategies utilized to enhance the D-A assembly and electronic interaction between D and A are shape complementarity, halogen bonding and co-crystallization of strong D-A pairs for example strong electron withdrawing moieties on the acceptor, such as fluorine and strong electron donating moieties on the donor, such as thiophenes. [101,102,106,109] In addition, air-stable ambipolar CT semiconductors, much like n-type semiconductors, are very uncommon largely due to the high LUMO levels which easily result in degradation or even absence of charge-transport characteristics under ambient conditions. Therefore it is extremely important to study and develop new air-stable ambipolar and n-type materials since they are essential unit blocks in organic electronics. [103]

The ordered assembly and aggregation of D-A organic solid co-crystal strongly depends on the supramolecular interactions, including van der Waals, π-π interactions and halogen/hydrogen bonding. [110] Like in single component organic molecular crystals, in CT complexes there is a strong relationship between the crystal structure and the electronic, optical, and charge transport properties of the system. This relationship is even stronger in the case of CT co-crystals since D-A organic cocrystals are typically divided into two main families with very distinct charge transport properties. One which shows segregated stacking (…-D-D-D-… and …-A-A-A-…), where the molecules form separated D and A stacks and normally display high electrical conductivity, and one which shows a mixed stack (…-D-A-D-A-…), where the D and A molecules pack in an alternate way along the stack and usually are insulators or semiconductors, Figure 4. [94,97,110]

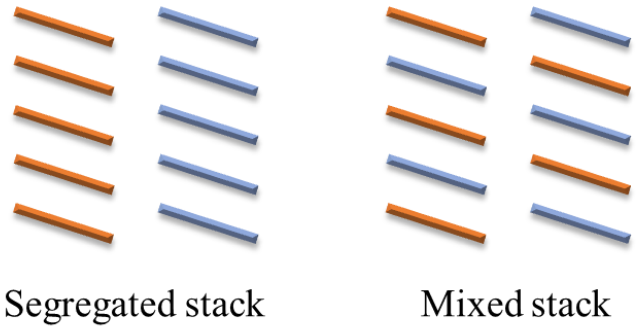

Figure 4 – Crystalline packing of 1:1 charge-transfer complexes for segregated stack and mixed stack motifs

Similar to single component systems, CT co-crystals can exhibit several polymorphic forms that possess the same donor and acceptor molecules in the same ratio and show very different

properties. For example, BEDT-TTF−TCNQ crystallizes in two triclinic (β′ and β″) phases with and a monoclinic phase. The crystals of β′ and of the monoclinic phase (both with mixed stack) have semiconducting properties while the crystals of β″ (characterized by a segregated stack) show a metallic behavior. [95,97] Furthermore, polymorphism becomes more complex when the crystal is formed by molecules that have different chemical identities, and besides the dispersive intermolecular interactions other forces are present. Thus the range of crystal forms of CT systems can be significantly extended since the same D and A can crystalize with different stoichiometries of the two species, this phenomenon is called stoichiomorphism. [97,111]

Although a lot of studies have been done on polymorphism control in crystals based on monomolecular compounds, the polymorphism of D-A systems and the control of the orientation of the CT complexes on substrates have been rarely reported and it is not easily achieved, due to the complicated highly ordered crystalline state. [112]

Aim of the thesis

This work is part of the UHMob-Ultra-high Charge Carrier Mobility to Elucidate Transport Mechanisms in Molecular Semiconductors project, a European Training Network (ETN) with the goal of gaining a fundamental understanding of charge transport mechanisms in molecular semiconductors. To achieve this objective best-performing and well-characterized materials were studied by 15 early-stage researchers (ESRs), of which I was part of, by a complementary set of methods, including field effect transistors but also optical methods such as terahertz spectroscopy, field-induced time-resolved microwave conductivity. The 15 PhD students involved in the UHMob project also explored the coupling of molecular semiconductors with the vacuum electromagnetic field.[113]

My contribution to the project was mainly focused on the study of bulk and surface-induced polymorphism of molecular semiconductors in order to obtain the best-performing semiconductor. It is known that substrate induced polymorphism is largely observed for molecular semiconductors, but its origin remains unknown, and this field continues relatively unpublished.

I focused my project on NDI derivatives, a well-known class of n-type semiconductors, in particular on NDI-C6 (N,N'-bis(*n*-hexyl)naphthalene-1,4,5,8-tetracarboxylicdiimide) a well-known compound which shows different crystal forms and CF_3-NDI (4,5,9,10-tetrachloro-2,7-bis (2,2,2-trifluoroethyl)benzo[lmn][3,8]phenanthroline-1,3,6,8(2H,7H)-tetraone) which was synthesized by BASF, one of the partners of the project. The NDI-C6 was chosen as benchmark to train my skills and competences, but it turned out to be very interesting and its study covered a major part of the project. It was also the main compound studied during my secondments. The first secondment was at the Technische Universität Graz (TUGraz), to characterize thin films, while the second secondment was at the University of Cambridge, where devices with different polymorphs as active layers were manufactured. Unfortunately, my stay at the TUGraz took place during the pandemic and work was extremely slowed down. During the last part of my thesis, I studied the CF_3-NDI, and during the bulk polymorph screening they showed a strong propensity to form charge transfer co-crystals. The last part of my thesis I explored the possibility to obtain CT co-crystal with $C_3F_7Cl_2$-NDI, $C_3F_7Cl_4$-NDI, CF_3Cl_4-NDI, and $C_4F_9Cl_4$-NDI.

References

(1) Schneider, J. A.; Perepichka, D. F. 1. Design Principles for Organic Semiconductors. In *Advanced Materials*; van de Ven, T., Soldera, A., Eds.; De Gruyter, 2019; pp 1–50. https://doi.org/10.1515/9783110537734-001.

(2) Rahman, A. A Review on Semiconductors Including Applications and Temperature Effects in Semiconductors. **2014**, *7* (1), 21.

(3) Jenkins, T. A Brief History of ... Semiconductors. *Phys. Educ.* **2005**, *40* (5), 430–439. https://doi.org/10.1088/0031-9120/40/5/002.

(4) Keyes, R. W. Physical Limits of Silicon Transistors and Circuits. *Rep. Prog. Phys.* **2005**, *68* (12), 2701–2746. https://doi.org/10.1088/0034-4885/68/12/R01.

(5) Coropceanu, V.; Cornil, J.; da Silva Filho, D. A.; Olivier, Y.; Silbey, R.; Brédas, J.-L. Charge Transport in Organic Semiconductors. *Chem. Rev.* **2007**, *107* (4), 926–952. https://doi.org/10.1021/cr050140x.

(6) Gao, X.; Hu, Y. Development of N-Type Organic Semiconductors for Thin Fi Lm Transistors : A Viewpoint of Molecular. **2014**, 3099–3117. https://doi.org/10.1039/c3tc32046d.

(7) Ferry, D. K. *Semiconductors (2nd Edition)*; IOP Publishing, 2019. https://doi.org/10.1088/978-0-7503-2480-9.

(8) Ostroverkhova, O. *Handbook of Organic Materials for Optical and (Opto)Electronic Devices*; Woodhead Publishing Limited, 2013. https://doi.org/10.1533/9780857098764.

(9) Dhar, J.; Salzner, U.; Patil, S. Trends in Molecular Design Strategies for Ambient Stable N-Channel Organic Field Effect Transistors. *J. Mater. Chem. C* **2017**, *5* (30), 7404–7430. https://doi.org/10.1039/C6TC05467F.

(10) Mei, J.; Diao, Y.; Appleton, A. L.; Fang, L.; Bao, Z. Integrated Materials Design of Organic Semiconductors for Field-Effect Transistors. *Journal of the american chemical society* **2013**, *135* (18), 6724–6746. https://doi.org/10.1021/ja400881n.

(11) Nordén, B. Advanced Information - The Nobel Prize in Chemistry 2000. 16.

(12) Chiang, C. K.; Fincher, C. R.; Park, Y. W.; Heeger, A. J.; Shirakawa, H.; Louis, E. J.; Gau, S. C.; MacDiarmid, A. G. Electrical Conductivity in Doped Polyacetylene. *Phys. Rev. Lett.* **1977**, *39* (17), 1098–1101. https://doi.org/10.1103/PhysRevLett.39.1098.

(13) Usta, H.; Facchetti, A.; Marks, T. J. N-Channel Semiconductor Materials Design for Organic Complementary Circuits. *Acc. Chem. Res.* **2011**, *44* (7), 501–510. https://doi.org/10.1021/ar200006r.

(14) Self-Assembled Supramolecular Materials in Organic Electronics. In *Supramolecular Materials for Opto-Electronics*; Koch, N., Ed.; Royal Society of Chemistry: Cambridge, 2014; pp P001–P004. https://doi.org/10.1039/9781782626947-FP001.

(15) Berggren, M.; Nilsson, D.; Robinson, N. D. Organic Materials for Printed Electronics. *Nature Mater* **2007**, *6* (1), 3–5. https://doi.org/10.1038/nmat1817.

(16) Fratini, S.; Nikolka, M.; Salleo, A.; Schweicher, G.; Sirringhaus, H. Charge Transport in High-Mobility Conjugated Polymers and Molecular Semiconductors. *Nat. Mater.* **2020**, *19* (5), 491–502. https://doi.org/10.1038/s41563-020-0647-2.

(17) Facchetti, A. Semiconductors for Organic Transistors. *Materials Today* **2007**, *10* (3), 28–37. https://doi.org/10.1016/S1369-7021(07)70017-2.

(18) Schweicher, G.; Olivier, Y.; Lemaur, V.; Geerts, Y. H. What Currently Limits Charge Carrier Mobility in Crystals of Molecular Semiconductors? *Isr. J. Chem.* **2014**, *54* (5–6), 595–620. https://doi.org/10.1002/ijch.201400047.

(19) Costa, J. C. S.; Taveira, R. J. S.; Lima, C. F. R. A. C.; Mendes, A.; Santos, L. M. N. B. F. Optical Band Gaps of Organic Semiconductor Materials. *Optical Materials* **2016**, *58*, 51–60. https://doi.org/10.1016/j.optmat.2016.03.041.

(20) *Large Area and Flexible Electronics*; Mario Caironi, Yong-Young Noh, Eds.; Wiley-VCH Verlag GmbH & Co. KGaA, 2015.
(21) Ostroverkhova, O. Organic Optoelectronic Materials: Mechanisms and Applications. *Chem. Rev.* **2016**, *116* (22), 13279–13412. https://doi.org/10.1021/acs.chemrev.6b00127.
(22) Juve, G. Organic Semiconducting Oligomers for Use in Thin Film Transistors. *XRDS* **2011**, *17* (4), 58–59. https://doi.org/10.1145/1961678.1961690.
(23) Köhler, A.; Bässler, H. *Electronic Processes in Organic Semiconductors*.
(24) Wang, C.; Dong, H.; Jiang, L.; Hu, W. Organic Semiconductor Crystals. *Chem. Soc. Rev.* **2018**, *47* (2), 422–500. https://doi.org/10.1039/C7CS00490G.
(25) Friederich, P.; Meded, V.; Poschlad, A.; Neumann, T.; Rodin, V.; Stehr, V.; Symalla, F.; Danilov, D.; Lüdemann, G.; Fink, R. F.; Kondov, I.; von Wrochem, F.; Wenzel, W. Molecular Origin of the Charge Carrier Mobility in Small Molecule Organic Semiconductors. *Adv. Funct. Mater.* **2016**, *26* (31), 5757–5763. https://doi.org/10.1002/adfm.201601807.
(26) Hutchison, G. R.; Ratner, M. A.; Marks, T. J. Intermolecular Charge Transfer between Heterocyclic Oligomers. Effects of Heteroatom and Molecular Packing on Hopping Transport in Organic Semiconductors. *J. Am. Chem. Soc.* **2005**, *127* (48), 16866–16881. https://doi.org/10.1021/ja0533996.
(27) Bronstein, H.; Nielsen, C. B.; Schroeder, B. C.; McCulloch, I. The Role of Chemical Design in the Performance of Organic Semiconductors. *Nat Rev Chem* **2020**, *4* (2), 66–77. https://doi.org/10.1038/s41570-019-0152-9.
(28) Haneef, H. F.; Zeidell, A. M.; Jurchescu, O. D. Charge Carrier Traps in Organic Semiconductors: A Review on the Underlying Physics and Impact on Electronic Devices. *J. Mater. Chem. C* **2020**, *8* (3), 759–787. https://doi.org/10.1039/C9TC05695E.
(29) Schiefer, S.; Huth, M.; Dobrinevski, A.; Nickel, B. Determination of the Crystal Structure of Substrate-Induced Pentacene Polymorphs in Fiber Structured Thin Films. **2007**, 10316–10317. https://doi.org/10.1021/ja0730516.
(30) Klauk, H.; Gundlach, D. J.; Nichols, J. A.; Jackson, T. N. Pentacene Organic Thin-Film Transistors for Circuit and Display Applications. *IEEE Trans. Electron Devices* **1999**, *46* (6), 1258–1263. https://doi.org/10.1109/16.766895.
(31) Gundlach, D. J.; Jackson, T. N.; Schlom, D. G.; Nelson, S. F. Solvent-Induced Phase Transition in Thermally Evaporated Pentacene Films. *Appl. Phys. Lett.* **1999**, *74* (22), 3302–3304. https://doi.org/10.1063/1.123325.
(32) Hannah Schamoni; Simon Noever; Bert Nickel; Martin Stutzmann; Jose A. Garrido. α,ω-Dihexyl-Sexithiophene Thin Films for Solution-Gated Organic Field-Effect Transistors. *Appl. Phys. Lett.* **2016**, *108*.
(33) Garnier, F.; Yassar, A.; Hajlaoui, R.; Horowitz, G.; Deloffre, F.; Servet, B.; Ries, S.; Alnot, P. Molecular Engineering of Organic Semiconductors: Design of Self-Assembly Properties in Conjugated Thiophene Oligomers. *J. Am. Chem. Soc.* **1993**, *115* (19), 8716–8721. https://doi.org/10.1021/ja00072a026.
(34) Jones, A. O. F.; Geerts, Y. H.; Karpinska, J.; Kennedy, A. R.; Resel, R.; Röthel, C.; Ruzié, C.; Werzer, O.; Sferrazza, M. Substrate-Induced Phase of a [1]Benzothieno[3,2- *b*]Benzothiophene Derivative and Phase Evolution by Aging and Solvent Vapor Annealing. *ACS Appl. Mater. Interfaces* **2015**, *7* (3), 1868–1873. https://doi.org/10.1021/am5075908.
(35) Kazuo Takimiya; Tatsuya Yamamoto; Hideaki Ebata; Takafumi Izawa. [1]Benzothieno[3,2-b][1]Benzothiophenes- and Dinaphtho[2,3-b:2′,3′-f] Thieno[3,2-b]Thiophene-Based Organic Semiconductors for Stable, High-Performance Organic Thin-Film Transistor Materials. *Thin Solid Films* **2014**, *554*.
(36) Bhosale, S. V.; Kobaisi, M. A.; Jadhav, R. W.; Morajkar, P. P.; Jones, L. A.; George, S. Naphthalene Diimides : Perspectives and Promise. *Chemical Society Reviews* **2021**, *50*, 9845–9998. https://doi.org/10.1039/d0cs00239a.

(37) Würthner, F.; Stolte, M. Naphthalene and Perylene Diimides for Organic Transistors. *Chem. Commun.* **2011**, *47* (18), 5109. https://doi.org/10.1039/c1cc10321k.
(38) Minemawari, H.; Yamada, T.; Matsui, H.; Tsutsumi, J.; Haas, S.; Chiba, R.; Kumai, R.; Hasegawa, T. Inkjet Printing of Single-Crystal Films. *Nature* **2011**, *475* (7356), 364–367. https://doi.org/10.1038/nature10313.
(39) Joon Hak Oh. High-Performance Air-Stable N-Type Organic Transistors Based on Core-Chlorinated Naphthalene Tetracarboxylic Diimides. *Adv. Funct. Mater.*
(40) Yan Zhao; Yunlong Guo; Yunqi Liu. 25th Anniversary Article: Recent Advances in N-Type and Ambipolar Organic Field-Effect. *Adv. Mater.* **2013**, *25*, 5372–5391.
(41) Meng, Q.; Hu, W. Recent Progress of N-Type Organic Semiconducting Small Molecules for Organic Field-Effect Transistors. *Phys. Chem. Chem. Phys.* **2012**, *14* (41), 14152. https://doi.org/10.1039/c2cp41664f.
(42) Yamashita, Y. Organic Semiconductors for Organic Field-Effect Transistors. *Science and Technology of Advanced Materials* **2009**, *10* (2), 024313. https://doi.org/10.1088/1468-6996/10/2/024313.
(43) Anthony, J. E.; Facchetti, A.; Heeney, M.; Marder, S. R.; Zhan, X. N-Type Organic Semiconductors in Organic Electronics. *Adv. Mater.* **2010**, *22*, 3876–3892.
(44) Welford, A.; Maniam, S.; Gann, E.; Jiao, X.; Thomsen, L.; Langford, S. J.; Mcneill, C. R. Influence of Alkyl Side-Chain Type and Length on the Thin Film Microstructure and OFET Performance of Naphthalene Diimide-Based Organic Semiconductors. *Organic Electronics* **2019**, *75* (July), 105378. https://doi.org/10.1016/j.orgel.2019.105378.
(45) Al Kobaisi, M.; Bhosale, S. V.; Latham, K.; Raynor, A. M.; Bhosale, S. V. Functional Naphthalene Diimides: Synthesis, Properties, and Applications. *Chem. Rev.* **2016**, *116* (19), 11685–11796. https://doi.org/10.1021/acs.chemrev.6b00160.
(46) Shukla, D.; Nelson, S. F.; Freeman, D. C.; Rajeswaran, M.; Ahearn, W. G.; Meyer, D. M.; Carey, J. T. Thin-Film Morphology Control in Naphthalene-Diimide-Based Semiconductors : High Mobility n-Type Semiconductor for Organic Thin-Film Transistors. **2008**, No. 4, 7486–7491.
(47) Sagdullina, D.; Lukashkin, N.; Parfenov, A.; Lyssenko, K.; Troshin, P. Highly Sensitive OFET-Based Gas Sensors Using Fluorinated Naphthalenediimide Semiconductor Films. *Synthetic Metals* **2020**, *260*, 116289. https://doi.org/10.1016/j.synthmet.2019.116289.
(48) Zhan, X.; Facchetti, A.; Barlow, S.; Marks, T. J.; Ratner, M. A.; Wasielewski, M. R.; Marder, S. R. Rylene and Related Diimides for Organic Electronics. *Adv. Mater.* **2011**, *23* (2), 268–284. https://doi.org/10.1002/adma.201001402.
(49) Dodabalapur, A.; Katz, H. E.; Torsi, L.; Haddon, R. C. Organic Heterostructure Field-Effect Transistors. *Science* **1995**, *269* (5230), 1560–1562. https://doi.org/10.1126/science.269.5230.1560.
(50) Horowitz, G.; Kouki, F.; Spearman, P.; Fichou, D.; Nogues, C.; Pan, X.; Garnier, F. Evidence for N-Type Conduction in a Perylene Tetracarboxylic Diimide Derivative. *Adv. Mater.* **1996**, *8* (3), 242–245. https://doi.org/10.1002/adma.19960080312.
(51) Laquindanum, J. G.; Katz, H. E.; Dodabalapur, A.; Lovinger, A. J. N-Channel Organic Transistor Materials Based on Naphthalene Frameworks. *J. Am. Chem. Soc.* **1996**, *118* (45), 11331–11332. https://doi.org/10.1021/ja962461j.
(52) Kim, R.; Amegadze, P. S. K.; Kang, I.; Yun, H.; Noh, Y.; Kwon, S.; Kim, Y. High-Mobility Air-Stable Naphthalene Diimide-Based Copolymer Containing Extended π -Conjugation for n-Channel Organic Field Effect Transistors. **2013**, 1–9. https://doi.org/10.1002/adfm.201301197.
(53) Gentili, D.; Gazzano, M.; Melucci, M.; Jones, D.; Cavallini, M. Polymorphism as an Additional Functionality of Materials for Technological Applications at Surfaces and Interfaces. *Chem. Soc. Rev.* **2019**, *48* (9), 2502–2517. https://doi.org/10.1039/C8CS00283E.
(54) Wen-Ya Lee; Joon Hak Oh; Sabin-Lucian Suraru; Wen-Chang Chen; Frank Würthner; Zhenan Bao. High-Mobility Air-Stable Solution-Shear-Processed N-Channel Organic Transistors Based on Core-Chlorinated Naphthalene Diimides. *Adv. Funct. Mater.* **2011**, *21*, 4173–4181.

(55) Chen, X.; Zhang, D.; He, Y.; Ali, M. U.; Wu, Y.; Zhao, C.; Wu, P.; Yan, C.; Wudl, F.; Meng, H. Fluoro-Alkyl Substituted Isothianaphthene Bisimides as Stable n-Type Semiconductors. *Mater. Chem. Front.* **2020**, *4* (12), 3578–3584. https://doi.org/10.1039/D0QM00137F.

(56) He, T.; Stolte, M.; Würthner, F. Air-Stable n-Channel Organic Single Crystal Field-Effect Transistors Based on Microribbons of Core-Chlorinated Naphthalene Diimide. *Adv. Mater.* **2013**, *25* (48), 6951–6955. https://doi.org/10.1002/adma.201303392.

(57) Canola, S.; Negri, F. Anisotropy of the N-Type Charge Transport and Thermal Effects in Crystals of a Fluoro-Alkylated Naphthalene Diimide: A Computational Investigation. *Phys. Chem. Chem. Phys.* **2014**, *16* (39), 21550–21558. https://doi.org/10.1039/C4CP03231D.

(58) Ze-Fan Yao; Jie-Yu Wang; Jian Pei. Control of Π−π Stacking via Crystal Engineering in Organic. *Cryst. Growth Des* **2018**, *18*, 7−15.

(59) Katz, H. E.; Lovinger, A. J.; Johnson, J.; Kloc, C.; Siegrist, T.; Li, W.; Lin, Y.-Y.; Dodabalapur, A. A Soluble and Air-Stable Organic Semiconductor with High Electron Mobility. *Nature* **2000**, *404* (6777), 478–481. https://doi.org/10.1038/35006603.

(60) Higginbotham, H. F.; Pander, P.; Rybakiewicz, R.; Etherington, M. K.; Maniam, S.; Zagorska, M.; Pron, A.; Monkman, A. P.; Data, P. Triphenylamine Disubstituted Naphthalene Diimide: Elucidation of Excited States Involved in TADF and Application in near-Infrared Organic Light Emitting Diodes. *J. Mater. Chem. C* **2018**, *6* (30), 8219–8225. https://doi.org/10.1039/C8TC02936A.

(61) Ma, F.; Hu, Z.; Jiao, L.; Wang, X.; Yang, Y.; Li, Z.; He, Y. Synthesis and Application of Naphthalene Diimide as an Organic Molecular Electrode for Asymmetric Supercapacitors with High Energy Storage. *Adv Materials Inter* **2021**, *8* (10), 2002161. https://doi.org/10.1002/admi.202002161.

(62) Yang, J.; Xiao, B.; Tajima, K.; Nakano, M.; Takimiya, K.; Tang, A.; Zhou, E. Comparison among Perylene Diimide (PDI), Naphthalene Diimide (NDI), and Naphthodithiophene Diimide (NDTI) Based n-Type Polymers for All-Polymer Solar Cells Application. *Macromolecules* **2017**, *50* (8), 3179–3185. https://doi.org/10.1021/acs.macromol.7b00414.

(63) Doria, F.; Amendola, V.; Grande, V.; Bergamaschi, G.; Freccero, M. Naphthalene Diimides as Selective Naked-Eye Chemosensor for Copper(II) in Aqueous Solution. *Sensors and Actuators B: Chemical* **2015**, *212*, 137–144. https://doi.org/10.1016/j.snb.2015.01.113.

(64) Ghule, N. V.; Bhosale, R. S.; Kharat, K.; Puyad, A. L.; Bhosale, S. V.; Bhosale, S. V. A Naphthalenediimide-Based Fluorescent Sensor for Detecting the PH within the Rough Endoplasmic Reticulum of Living Cells. *ChemPlusChem* **2015**, *80* (3), 485–489. https://doi.org/10.1002/cplu.201402307.

(65) Doria, F.; Nadai, M.; Sattin, G.; Pasotti, L.; Richter, S. N.; Freccero, M. Water Soluble Extended Naphthalene Diimides as PH Fluorescent Sensors and G-Quadruplex Ligands. *Org. Biomol. Chem.* **2012**, *10* (19), 3830. https://doi.org/10.1039/c2ob07006e.

(66) Bernstein, J. *Polymorphism in Molecular Crystals*; International Union of Crystallography monographs on crystallography; Oxford University Press: OxfordClarendon Press ; New York, 2002.

(67) Cruz-Cabeza, A. J.; Bernstein, J. Conformational Polymorphism. *Chem. Rev.* **2014**, *114* (4), 2170–2191. https://doi.org/10.1021/cr400249d.

(68) Desiraju, G. R. Polymorphism: The Same and Not Quite the Same. *Crystal Growth & Design* **2008**, *8* (1), 3–5. https://doi.org/10.1021/cg701000q.

(69) *Polymorphism (in the Pharmaceutical Industry)*; Hilfiker, R., Ed.; WILEY-VCH Verlag GmbH & Co. KGaA, 2006.

(70) Zhen, Y.; Dong, H.; Jiang, L.; Hu, W. Tailoring Crystal Polymorphs of Organic Semiconductors towards High-Performance Field-Effect Transistors. *Chinese Chemical Letters* **2016**, *27* (8), 1330–1338. https://doi.org/10.1016/j.cclet.2016.06.023.

(71) Brog, J.-P.; Chanez, C.-L.; Crochet, A.; Fromm, K. M. Polymorphism, What It Is and How to Identify It: A Systematic Review. *RSC Adv.* **2013**, *3* (38), 16905. https://doi.org/10.1039/c3ra41559g.
(72) Shtukenberg, A. G.; Drori, R.; Sturm, E. V.; Vidavsky, N.; Haddad, A.; Zheng, J.; Estroff, L. A.; Weissman, H.; Wolf, S. G.; Shimoni, E.; Li, C.; Fellah, N.; Efrati, E.; Kahr, B. Crystals of Benzamide, the First Polymorphous Molecular Compound, Are Helicoidal. *Angew. Chem. Int. Ed.* **2020**, *59* (34), 14593–14601. https://doi.org/10.1002/anie.202005738.
(73) Cruz-Cabeza, A. J.; Reutzel-Edens, S. M.; Bernstein, J. Facts and Fictions about Polymorphism. *Chem. Soc. Rev.* **2015**, *44* (23), 8619–8635. https://doi.org/10.1039/C5CS00227C.
(74) Chung, H.; Diao, Y. Polymorphism as an Emerging Design Strategy for High Performance Organic Electronics. *Journal of Materials Chemistry C* **2016**, *4* (18), 3915–3933. https://doi.org/10.1039/c5tc04390e.
(75) Lee, E. H. A Practical Guide to Pharmaceutical Polymorph Screening & Selection. *Asian Journal of Pharmaceutical Sciences* **2014**, *9* (4), 163–175. https://doi.org/10.1016/j.ajps.2014.05.002.
(76) Bučar, D.-K.; Lancaster, R. W.; Bernstein, J. Disappearing Polymorphs Revisited. *Angew. Chem. Int. Ed.* **2015**, *54* (24), 6972–6993. https://doi.org/10.1002/anie.201410356.
(77) Bernstein, J. Polymorphism − A Perspective. *Crystal Growth & Design* **2011**, *11* (3), 632–650. https://doi.org/10.1021/cg1013335.
(78) Herbstein, F. H. Diversity Amidst Similarity: A Multidisciplinary Approach to Phase Relationships, Solvates, and Polymorphs. *Crystal Growth & Design* **2004**, *4* (6), 1419–1429. https://doi.org/10.1021/cg030081l.
(79) Diao, Y.; Lenn, K. M.; Lee, W.; Blood-forsythe, M. A.; Xu, J.; Mao, Y.; Kim, Y.; Reinspach, J. A.; Park, S.; Xue, G.; Clancy, P. Understanding Polymorphism in Organic Semiconductor Thin Films through Nanocon Fi Nement. **2014**. https://doi.org/10.1021/ja507179d.
(80) Jones, A. O. F.; Chattopadhyay, B.; Geerts, Y. H.; Resel, R. Substrate-Induced and Thin-Film Phases : Polymorphism of Organic Materials on Surfaces. *Advanced Functional Materials* **2016**, *26*, 2233–2255. https://doi.org/10.1002/adfm.201503169.
(81) Tommaso Salzillo; Aldo Brillante. A New Approach to Polymorphism in Molecular Crystals: Substrate-Mediated Structures Revealed by Lattice Phonon Dynamics.
(82) Ehmann, H. M. A.; Werzer, O. Surface Mediated Structures: Stabilization of Metastable Polymorphs on the Example of Paracetamol. *Crystal Growth & Design* **2014**, *14* (8), 3680–3684. https://doi.org/10.1021/cg500573e.
(83) Reischl, D.; Ro, C.; Christian, P.; Roblegg, E.; Ehmann, H. M. A.; Salzmann, I.; Werzer, O. Surface-Induced Polymorphism as a Tool for Enhanced Dissolution: The Example of Phenytoin. *crystal growth & design* **2015**, *15*, 4687–4693. https://doi.org/10.1021/acs.cgd.5b01002.
(84) Hao, Y.; Velpula, G.; Kaltenegger, M.; Bodlos, W. R.; Vibert, F.; Mali, K. S.; De Feyter, S.; Resel, R.; Geerts, Y. H.; Van Aert, S.; Beljonne, D.; Lazzaroni, R. From 2D to 3D: Bridging Self-Assembled Monolayers to a Substrate-Induced Polymorph in a Molecular Semiconductor. *Chem. Mater.* **2022**, *34* (5), 2238–2248. https://doi.org/10.1021/acs.chemmater.1c04038.
(85) Mattheus, C. C.; Dros, A. B.; Baas, J.; Oostergetel, G. T.; Meetsma, A.; de Boer, J. L.; Palstra, T. T. M. Identification of Polymorphs of Pentacene. *Synthetic Metals* **2003**, *138* (3), 475–481. https://doi.org/10.1016/S0379-6779(02)00467-8.
(86) Bouchoms, I. P. M.; Schoonveld, W. A.; Vrijmoeth, J.; Klapwijk, T. M. Morphology Identification of the Thin Film Phases of Vacuum Evaporated Pentacene on SIO2 Substrates. *Synthetic Metals* **1999**, *104* (3), 175–178. https://doi.org/10.1016/S0379-6779(99)00050-8.
(87) Obersteiner, V.; Scherbela, M.; Hörmann, L.; Wegner, D.; Hofmann, O. T. Structure Prediction for Surface-Induced Phases of Organic Monolayers: Overcoming the Combinatorial Bottleneck. *Nano Lett.* **2017**, *17* (7), 4453–4460. https://doi.org/10.1021/acs.nanolett.7b01637.
(88) Pithan, L.; Nabok, D.; Cocchi, C.; Beyer, P.; Duva, G.; Simbrunner, J.; Nicklin, C.; Schäfer, P.; Draxl, C.; Schreiber, F.; Kowarik, S.; Pithan, L.; Nabok, D.; Cocchi, C.; Beyer, P.; Duva, G.;

Schreiber, F.; Kowarik, S. Molecular Structure of the Substrate-Induced Thin-Film Phase of Tetracene. *The journal of chemical physics* **2018**, *149*, 144701. https://doi.org/10.1063/1.5043379.

(89) Guillaume Schweicher; Guillaume Garbay; Rémy Jouclas; François Vibert; Félix Devaux; Yves H. Geerts. Molecular Semiconductors for Logic Operations: Dead-End or Bright Future? *Advanced Materials* **2020**, *32*.

(90) Gentili, D.; Liscio, F.; Demitri, N.; Schäfer, B.; Borgatti, F.; Torelli, P.; Gobaut, B.; Panaccione, G.; Rossi, G.; Degli Esposti, A.; Gazzano, M.; Milita, S.; Bergenti, I.; Ruani, G.; Šalitroš, I.; Ruben, M.; Cavallini, M. Surface Induces Different Crystal Structures in a Room Temperature Switchable Spin Crossover Compound. *Dalton Trans.* **2016**, *45* (1), 134–143. https://doi.org/10.1039/C5DT03712C.

(91) Arash Badami-Behjat; Peter S.Deimel; Francesco Allegretti; Eva Ringel; Kingsuk Mahata; Michael Schmittel; Johannes V.Barth; Wolfgang M. Heckl; Markus Lackinger. Versatile Role of Molecule−Surface Interactions for Monolayer SelfAssembly at Liquid−Solid Interfaces Substrate-Induced. *Chem. Mater.* **2022**, *34*, 8876−8884.

(92) Seibel, J.; Amabilino, D. B.; De Feyter, S. Preferred Formation of Minority Concomitant Polymorphs in 2D Self-Assembly under Lateral Nanoconfinement. *Angew Chem Int Ed* **2019**, *58* (37), 12964–12968. https://doi.org/10.1002/anie.201908552.

(93) Pandolfi, L.; Rivalta, A.; Salzillo, T.; Giunchi, A.; D'Agostino, S.; Della Valle, R. G.; Brillante, A.; Venuti, E. In Search of Surface-Induced Crystal Structures: The Case of Tyrian Purple. *J. Phys. Chem. C* **2020**, *124* (32), 17702–17710. https://doi.org/10.1021/acs.jpcc.0c05186.

(94) Fijahi, L.; Salzillo, T.; Tamayo, A.; Bardini, M.; Ruzié, C.; Quarti, C.; Beljonne, D.; d'Agostino, S.; Geerts, Y. H.; Mas-Torrent, M. Charge Transfer Complexes of a Benzothienobenzothiophene Derivative and Their Implementation as Active Layer in Solution-Processed Thin Film Organic Field-Effect Transistors. *J. Mater. Chem. C* **2022**, *10* (18), 7319–7328. https://doi.org/10.1039/D2TC00655C.

(95) Goetz, K. P.; Tsutsumi, J.; Pookpanratana, S.; Chen, J.; Corbin, N. S.; Behera, R. K.; Coropceanu, V.; Richter, C. A.; Hacker, C. A.; Hasegawa, T.; Jurchescu, O. D. Polymorphism in the 1:1 Charge-Transfer Complex DBTTF–TCNQ and Its Effects on Optical and Electronic Properties. *Adv. Electron. Mater.* **2016**, *2* (10), 1600203. https://doi.org/10.1002/aelm.201600203.

(96) Solano, F.; Inaudi, P.; Abollino, O.; Giacomino, A.; Chiesa, M.; Salvadori, E.; Kociok-Kohn, G.; da Como, E.; Salzillo, T.; Fontanesi, C. Charge Transfer Modulation in Charge Transfer Co-Crystals Driven by Crystal Structure Morphology. *Phys. Chem. Chem. Phys.* **2022**, *24* (31), 18816–18823. https://doi.org/10.1039/D2CP01408D.

(97) Vermeulen, D.; Zhu, L. Y.; Goetz, K. P.; Hu, P.; Jiang, H.; Day, C. S.; Jurchescu, O. D.; Coropceanu, V.; Kloc, C.; McNeil, L. E. Charge Transport Properties of Perylene–TCNQ Crystals: The Effect of Stoichiometry. *J. Phys. Chem. C* **2014**, *118* (42), 24688–24696. https://doi.org/10.1021/jp508520x.

(98) Alves, H.; Pinto, R. M.; Maçôas, E. S. Photoconductive Response in Organic Charge Transfer Interfaces with High Quantum Efficiency. *Nat Commun* **2013**, *4* (1), 1842. https://doi.org/10.1038/ncomms2890.

(99) Laukhina, E.; Pfattner, R.; Ferreras, L. R.; Galli, S.; Mas-Torrent, M.; Masciocchi, N.; Laukhin, V.; Rovira, C.; Veciana, J. Ultrasensitive Piezoresistive All-Organic Flexible Thin Films. *Adv. Mater.* **2010**, *22* (9), 977–981. https://doi.org/10.1002/adma.200902639.

(100) Ullbrich, S.; Siegmund, B.; Mischok, A.; Hofacker, A.; Benduhn, J.; Spoltore, D.; Vandewal, K. Fast Organic Near-Infrared Photodetectors Based on Charge-Transfer Absorption. *J. Phys. Chem. Lett.* **2017**, *8* (22), 5621–5625. https://doi.org/10.1021/acs.jpclett.7b02571.

(101) Yee, N.; Dadvand, A.; Perepichka, D. F. Band Gap Engineering of Donor–Acceptor Co-Crystals by Complementary Two-Point Hydrogen Bonding. *Mater. Chem. Front.* **2020**, *4* (12), 3669–3677. https://doi.org/10.1039/D0QM00500B.

(102) Liu, H.; Liu, Z.; Jiang, W.; Fu, H. Tuning the Charge Transfer Properties by Optimized Donor – Acceptor Cocrystal for FET Applications: From P Type to N Type. *Journal of Solid State Chemistry* **2019**, *274*, 47–51. https://doi.org/10.1016/j.jssc.2019.03.017.

(103) Zhang, J.; Xu, W.; Sheng, P.; Zhao, G.; Zhu, D. Organic Donor–Acceptor Complexes as Novel Organic Semiconductors. *Acc. Chem. Res.* **2017**, *50* (7), 1654–1662. https://doi.org/10.1021/acs.accounts.7b00124.
(104) Hasegawa, T.; Mattenberger, K.; Takeya, J.; Batlogg, B. Ambipolar Field-Effect Carrier Injections in Organic Mott Insulators. *Phys. Rev. B* **2004**, *69* (24), 245115. https://doi.org/10.1103/PhysRevB.69.245115.
(105) Qin, Y.; Cheng, C.; Geng, H.; Wang, C.; Hu, W.; Xu, W.; Shuai, Z.; Zhu, D. Efficient Ambipolar Transport Properties in Alternate Stacking Donor–Acceptor Complexes: From Experiment to Theory. *Phys. Chem. Chem. Phys.* **2016**, *18* (20), 14094–14103. https://doi.org/10.1039/C6CP01509C.
(106) Zhang, J.; Jin, J.; Xu, H.; Zhang, Q.; Huang, W. Recent Progress on Organic Donor–Acceptor Complexes as Active Elements in Organic Field-Effect Transistors. *J. Mater. Chem. C* **2018**, *6* (14), 3485–3498. https://doi.org/10.1039/C7TC04389A.
(107) Wang, C.; Wang, J.; Wu, N.; Xu, M.; Yang, X.; Lu, Y.; Zang, L. Donor–Acceptor Single Cocrystal of Coronene and Perylene Diimide: Molecular Self-Assembly and Charge-Transfer Photoluminescence. *RSC Adv.* **2017**, *7* (4), 2382–2387. https://doi.org/10.1039/C6RA25447K.
(108) Wang, D.; Kan, X.; Wu, C.; Gong, Y.; Guo, G.; Liang, T.; Wang, L.; Li, Z.; Zhao, Y. Charge Transfer Co-Crystals Based on Donor–Acceptor Interactions for near-Infrared Photothermal Conversion. *Chem. Commun.* **2020**, *56* (39), 5223–5226. https://doi.org/10.1039/D0CC01834A.
(109) Kobaisi, M. A.; Bhosale, R. S.; El-Khouly, M. E.; La, D. D.; Padghan, S. D.; Bhosale, S. V.; Jones, L. A.; Antolasic, F.; Fukuzumi, S.; Bhosale, S. V. The Sensitivity of Donor – Acceptor Charge Transfer to Molecular Geometry in DAN – NDI Based Supramolecular Flower-like Self-Assemblies. *Sci Rep* **2017**, *7* (1), 16501. https://doi.org/10.1038/s41598-017-15599-9.
(110) Wang, J.; Zhang, S.; Xu, S.; Li, A.; Li, B.; Ye, L.; Geng, Y.; Tian, Y.; Xu, W. Morphology-Dependent Luminescence and Optical Waveguide Property in Large-Size Organic Charge Transfer Cocrystals with Anisotropic Spatial Distribution of Transition Dipole Moment. *Adv. Optical Mater.* **2020**, *8* (2), 1901280. https://doi.org/10.1002/adom.201901280.
(111) Salzillo, T.; Masino, M.; Kociok-Köhn, G.; Di Nuzzo, D.; Venuti, E.; Della Valle, R. G.; Vanossi, D.; Fontanesi, C.; Girlando, A.; Brillante, A.; Da Como, E. Structure, Stoichiometry, and Charge Transfer in Cocrystals of Perylene with TCNQ-F_x. *Crystal Growth & Design* **2016**, *16* (5), 3028–3036. https://doi.org/10.1021/acs.cgd.5b01663.
(112) Jin, J.; Wu, S.; Ma, Y.; Dong, C.; Wang, W.; Liu, X.; Xu, H.; Long, G.; Zhang, M.; Zhang, J.; Huang, W. Nucleation Control-Triggering Cocrystal Polymorphism of Charge-Transfer Complexes Differing in Physical and Electronic Properties. *ACS Appl. Mater. Interfaces* **2020**, *12* (17), 19718–19726. https://doi.org/10.1021/acsami.9b23590.
(113) *UHMob website*. https://www.uhmob.eu/.

This page intentionally left blank

Chapter 2: On the crystal forms of NDI-C6: annealing and deposition procedures to access elusive polymorphs

Overview

In this chapter, it is reported the study of the polymorphic behaviour of NDI-C6, a relatively cheap commercially available small-molecule organic n-type semiconductor which has high solubility.

In the research of this compound, I focused on polymorphic and thermal behaviour. For that, I used the crystallographic and solid-state characterization skills and knowledge acquired during this study including variable temperature X-ray powder diffraction (VT-XRPD), hot stage microscopy (HSM), structure determination from X-ray powder diffraction (XRPD) and thermal expansion analysis (PASCal). To have a deeper understanding of the different polymorphs at high temperatures I submitted a proposal (ID proposal 20201790) to the PSI synchrotron for the MS-X04SA beamline and I was able to collect the data at the beginning of 2021.

While working on this project I mastered TOPAS v5, the software used to perform structure determination from the powder of Form γ and used to obtain the input data needed for the PASCal tool.

Furthermore, a preliminary analysis of thin film polymorphism is also reported in this chapter, from where I got skills in thin-film deposition, namely spin-coating technique, and drop-casting.

These results were published in *Faraday Discussions - RSC Publishing*, in June 2022.

The publication can be found at:
https://pubs.rsc.org/en/content/articlelanding/2022/FD/D1FD00100K

Supplementary information can be found in Appendix A.

This page intentionally left blank

Faraday Discussions

Cite this: *Faraday Discuss.*, 2022, **235**, 490

PAPER

On the crystal forms of NDI-C6: annealing and deposition procedures to access elusive polymorphs†

Inês de Oliveira Martins, [ab] Francesco Marin, [b] Enrico Modena *[a] and Lucia Maini *[b]

Received 25th November 2021, Accepted 19th January 2022

DOI: 10.1039/d1fd00100k

NDI-C6 has been extensively studied for its semiconducting properties and its processability. It is known to have several polymorphs and a high thermal expansion. Here we report the full thermal characterization of **NDI-C6** by combining differential scanning calorimetry, variable temperature X-ray powder diffraction, and hot stage microscopy, which revealed two different thermal behaviours depending on the annealing process. The ranking of stability was determined by the temperature and energy involved in the transitions: Form α is stable from RT up to 175 °C, Form β is metastable at all temperatures, Form γ is stable in the range 175–178 °C, and Form δ in the range 178–207 °C followed by the melt at 207 °C. We determined the crystal structure of Form γ at 54 °C from powder. The analysis of the thermal expansion principal axis shows that Form α and Form γ possess negative thermal expansion (*X*1) and massive positive thermal expansion (*X*3) which are correlated to the thermal behaviour observed. We were able to isolate pure Form α, Form β, and Form γ in thin films and we found a new metastable form, called Form ε, by spin coating deposition of a toluene solution of **NDI-C6** on Si/SiO_2 substrates.

Introduction

In the past few decades organic semiconductors (OSCs) have attracted a lot of attention due to their possible employment in solution-processed optoelectronic and electronic devices, such as organic field-effect transistors (OFETs).[1–3] One of the big advantages of solution-processing is the possibility to produce flexible substrates at low cost.[3–5] This allows various potential applications that cannot be achieved with wafer-based electronics, such as large-area flexible displays, RFID

[a]*PolyCrystalLine SPA, Via Della Cooperazione, Bologna, 29 40059, Medicina, Italy. E-mail: enrico.modena@polycrystalline.it*

[b]*Dipartimento di Chimica "G. Ciamician", Via Selmi 2 – Universitá di Bologna, I-40126, Bologna, Italy. E-mail: l.maini@unibo.it*

† Electronic supplementary information (ESI) available. CCDC 2124322. For ESI and crystallographic data in CIF or other electronic format see DOI: 10.1039/d1fd00100k

tags, wearable electronics, and biomedical devices.[6–8] Organic molecular materials tend to form polymorphs, which can exhibit very different conductive,[9] luminescent,[10] and mechanical properties.[11] In most cases, the control of the crystal structure is decisive to maximise the performances of the final devices.[6,7,12,13]

In the field of organic electronics, there are several properties of the active layer that have a key role in the performance of the devices, namely, charge carrier mobility, and stability.[12,14,15] Polymorphism has proven to be an important factor to obtain high-performance organic devices since in some cases metastable phases can present mobilities some orders of magnitude higher than the most stable phase.[6,7] In addition, it is known that some materials can show new phases that are not observed in bulk when thin films are deposited in specific substrates, this effect is described as surface induced polymorphism.[15–19] Therefore, it is of extreme importance to study the polymorphism of OSCs, both in bulk and in thin films since the charge transport in electronic devices occurs in the interface between the OSC and the dielectric, in just a few layers of molecules.[20]

Bis(naphthalene diimide) (NDI) derivatives are a particularly interesting family of organic materials. NDIs possess high electron affinity, good charge carrier mobility, and excellent thermal and oxidative stability, making them promising candidates for applications in organic electronics, photovoltaic devices, and flexible displays.[8,21] Recently, the structure–properties relationship and the polymorphism of these molecules has gained considerable attention,[4,22–25] in particular the influence of the alkyl side chain length on performance and crystal structures has been studied.[26,27]

In this work we present the polymorphism both in bulk and in thin films of *N*,*N*′-bis(*n*-hexyl)naphthalene-1,4,5,8-tetracarboxylicdiimide (**NDI-C6**), Fig. 1, a cheap small-molecule organic n-type semiconductor which has high solubility making it easy to process.

It is known that **NDI-C6** is prone to generating several polymorphs, and the number of crystal forms is higher compared to the analogous molecules with shorter or higher chain length, nonetheless only the crystal structure of the most stable polymorph (Form α) is available.[24] Up to now, four different polymorphs have been reported: Form α the stable form at RT, and Form β, Form γ and Form δ – which can be obtained by thermal treatement and all convert back to Form α at RT.[27] Several papers report the preparation of thin films based on **NDI-C6**,[4,26–29] but only recently have the thin films been characterized by X-ray diffraction and revealed the presence of a mixture of Form α and a metastable polymorph at room

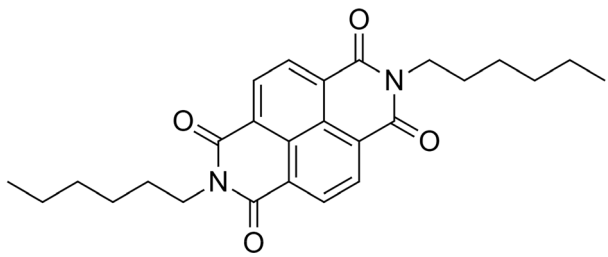

Fig. 1 Chemical structure of NDI-C6.

temperature.[26,27] Herein, the main goal of this work is to study and understand the polymorphic behaviour of **NDI-C6** in bulk and in thin films, with a special focus on the thermal behaviour. In fact, the annealing procedure is a common way to increase the performance of the devices, increasing the crystallinity,[30,31] but in the case of **NDI-C6** it can induce wanted or unwanted phase transitions. The synergic approach of the different thermal techniques such as hot stage optical microscopy (HSM), differential scanning calorimetry (DSC), and variable temperature X-ray powder diffraction (VT-XRPD), allowed us to determine the ranking in energy of the different polymorphs and to optimize different annealing procedures to obtain the desired phase in bulk and thin film. We were able to solve the structure of Form γ at high temperature by X-ray powder diffraction with synchrotron radiation. Furthermore, we optimized the thin film deposition to obtain pure phases and we discovered a new phase called ε.

Experimental

Materials

N,*N*′-Bis(*n*-hexyl)naphthalene-1,4,5,8-tetracarboxylic diimide (**NDI-C6**) is commercially available, it was purchased from Sigma-Aldrich and used as received.

Polymorph screening

The **NDI-C6** solubility was assessed in 12 different solvents at RT, 50 °C, 75 °C, and 100 °C when possible (see Table 1 in ESI†). Recrystallization by solvent evaporation was carried out in chloroform (CHF) and dichloromethane (DCM) at RT, in toluene (TOL) and *p*-xylene (PXY) at high temperature (60 °C) which presented the higher solubility.

For the remaining solvents and solvent mixtures of toluene and methanol (MET), with different ratios, slurry experiments at RT were performed. High temperature slurries were carried out for *N*,*N*-dimethylformamide (DMF) at 90 °C, 2-propanol (2PR), acetonitrile (ACN), and water (H_2O) at 50 °C. With the residual mother liquid obtained after filtration of the precipitate in the DMF solution, a high temperature (60 °C) evaporation experiment was set.

Crystallization by anti-solvent addition was performed testing TOL : MET (1 : 1.25 vol), PXY : MET (1 : 1.20 vol), CHF : *N*-heptane (HEP) (1 : 2 vol), DCM : acetone (ACT) (1 : 1.33 vol), and CHF : MET (1 : 1.5 vol).

Precipitation by gradient temperature was performed by crash cooling of DMF solutions and a solvent mixture of TOL : MET (1 : 1). Slow cooling crystallization was also tested with DMF solutions at different concentrations, using different cooling rates.

Solvothermal crystallization was carried out using TOL and PXY saturated solutions.

X-ray powder diffraction (XRPD)

All the precipitates obtained from the polymorph screening experiments, as well as the starting material, were characterized by XRPD to identify the crystalline phase. The XRD patterns were obtained using a Rigaku MiniFlex 600 diffractometer with Cu Kα ($\lambda = 1.54178$ Å) radiation from a copper sealed tube with 40 kV

voltage and 15 mA current in Bragg–Brentano geometry, over the 2θ range of 3–40° with a step size of 1 0.01° (2θ) at a speed of 10.0° min^{-1} (2θ).

Differential scanning calorimetry (DSC)

The starting material was characterized by differential scanning calorimetry (DSC) using a Mettler-Toledo DSC-1 instrument. The samples were prepared by accurately weighing approx. 2–4 mg of the powder in aluminium closed pans (40 μL). The measurements were performed during two cycles of heating and cooling with different rates (2 °C min^{-1}, 5 °C min^{-1} and 10 °C min^{-1}) under a dry N_2 atmosphere (flow rate 80 mL min^{-1}). All the data were analysed using STARe software.

Hot stage microscopy (HSM)

The thermal behaviour of the material was studied by hot stage microscopy (HSM), the transitions were observed on a single crystal of Form α, grown by precipitation by gradient temperature with a slow cooling rate, using an OLYMPUS BX41 stereomicroscope equipped with a LINKAM LTS350 platinum plate for temperature control and VISICAM analyser. The single crystal is placed on a glass slide and covered with a coverslip; next, it is set inside of the sealed heating chamber.

During the experiment time-lapse images were taken using a NIKON DS FI3 high speed camera and analysed using Nikon NIS Elements software and Linksys32.

Variable temperature X-ray powder diffraction (VT-XRPD)

VT-XRPD in transmission mode was performed at the Paul Scherrer Institute (PSI) synchrotron radiation facility (Switzerland) at MS-X04SA beamline using a well filled and compacted capillary with **NDI-C6** powder. The MS powder diffractometer used works in Debye–Scherrer geometry and is equipped with a solid-state silicon microstrip detector, called MYTHEN (Microstrip sYstem for Time-rEsolved experimeNts).[32] The data were collected with a beam energy of 12.4 keV (1.0 Å). The characterization was executed in a temperature range from 20 °C to 195 °C, to observe the several transitions that occur during temperature variation.

VT-XRPD in reflection mode were performed on a PANalytical X'Pert Pro automated diffractometer with an X'Celerator detector in Bragg–Brentano geometry, using Cu Kα radiation ($\lambda = 1.5418$ Å) without a monochromator in the 2θ range of 3–30.0° under continuous scan mode, step size of 0.0167°, counting time of 24.765 s, Soller slit of 0.04 rad, 40 mA and 40 kV equipped with an Anton Paar TTK 450 system for measurements at a controlled temperature.

Thin films deposition

Various thin films were fabricated by spin-coating on 2 × 2 cm^2 SiO_2/Si substrates, previously cleaned by sonication in an ethanol bath, followed by sonication in an acetone bath and finally rinsed with deionised water and dried with compressed air. Deposition was carried out varying the process parameters: solvent, concentration, and speed. In addition, thermal annealing at 75 °C for 1

Table 1 Parameters used to deposit **NDI-C6** films by spin-coating on SiO_2/Si substrates

Solvent	Concentration	Speed	Number of layers	Thermal annealing
TOL	1 mg mL^{-1}	1000 rpm	1	No
				Yes
			2	No
			3	No
		750 rpm	1	No
	3 mg mL^{-1}	1000 rpm	1	No
DCM	1 mg mL^{-1}	1000 rpm	1	No
			2	No
			3	No
		750 rpm	1	No
				Yes
	3 mg mL^{-1}	1000 rpm	1	No
CHF	1 mg mL^{-1}	750 rpm	1	No
				Yes

hour was performed for some samples. The details of the process parameters are summarised in Table 1.

Structure determination from powder

Indexing, structure determination and refinement of Form γ was performed using TOPAS v5, a nonlinear least-squares optimization program written in the C++ programming language.[33,34] The X-ray powder diffraction pattern of Form γ at 54 °C was indexed with triclinic cell with parameters: $a = 4.855$ Å, $b = 6.471$ Å, $c = 19.946$ Å, $\alpha = 92.14°$, $\beta = 95.83°$, $\gamma = 104.22$ and volume 603 Å^3 and space group $P\bar{1}$. The simulated annealing was performed with a half molecule constrained on the inversion centre. The best solution was chosen for Rietveld refinements, which were performed with the software TOPAS. A shifted Chebyshev function with five parameters and a pseudo-Voigt function were used to fit background and peak shape, respectively. An overall thermal parameter was adopted for all atoms of non-hydrogen atoms. All the hydrogen atoms were fixed in calculated positions. The Rietveld refinement reached the following values: Rwp = 3.45%, R = 2.12%, GoF = 2.81.

PASCal

PASCal – Principal Axis Strain Calculator is a web-based tool used to determine the principal coefficients of thermal expansion from variable-temperature lattice parameters.[35] The input data needed by the tool is simply the value of the temperature and the unit cell parameters at each temperature, for that we used the diffractograms acquired at PSI and refined the cell parameters using Pawley refinement. The tool returns as output the principal axis of thermal expansion and the orientation of the principal axes relative to the axes of the unit cell.

Results and discussion

Polymorph screening

Recrystallization experiments in ACN, ACT, CHF, DCM, MET, TOL, H_2O, 2PR, ETA and PXY led to the isolation of pure Form α, either as a powder or single crystals.

The single crystals were obtained by temperature gradient precipitation with a slow cooling profile. Crash cooling experiments in DMF allowed the concomitant crystallization of Form α and Form β in powder mixture. Furthermore, a mixture of the two different forms was also attained by evaporating at 60 °C, the filtered mother liquor from high temperature slurry experiments in DMF.

Recrystallization gave pure Form α or a mix with Form β. However, we were able to obtain pure Form β by annealing Form α. Phases γ and δ were observed only at high temperature, and it was not possible to achieve them at room temperature in bulk. However, in thin films it was possible to isolate Form α, Form β and Form γ at room temperature.

Thermal properties

We performed DSC, HSM and VT-XRPD on **NDI-C6** to characterize its thermal behaviour and the results were compared to determine the different phases obtained during the thermal treatment.

DSC analysis was based on the first heating, cooling and second heating cycles.

During the first heating of the starting material, the DSC curve presents a solid–solid transition around 178 °C before the melting point at 207 °C, Fig. 2b. This coincides with what has been described before by Milita *et al.*[27] and is ascribable to a double transition: Form α → Form γ suddenly followed by the transition of Form γ → Form δ. The Form α → Form δ transition could be clearly observed by HSM at 180 °C (see Fig. S1 in ESI†).

The VT-XRPD data (Fig. 3) are consistent with the described behaviour, an extra peak belonging to Form γ, appeared during the transition (around 180 °C), and disappeared concomitantly with the peaks of Form α once the transition into Form δ was complete.

While the first heating cycle of the **NDI-C6** Form α was always reproducible, the cooling cycle showed two different behaviours depending on whether the sample was melted or not. When the DSC experiment was performed without reaching the melting point of **NDI-C6**, the cooling curve matched with the behaviour

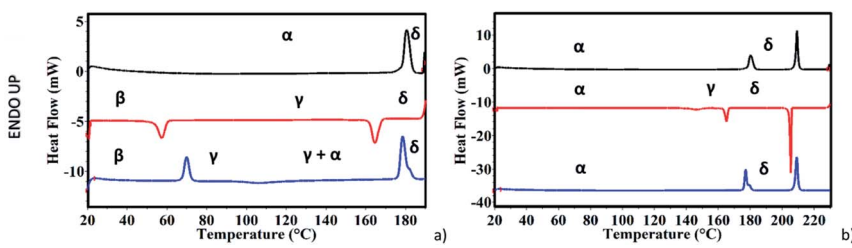

Fig. 2 DSC curves of **NDI-C6**, (a) heating cycle before melting, black line: first heating, up to the first transition Form α, γ → Form δ, red line: first cooling with two exothermic events, Form δ → Form γ at 163 °C and Form γ → Form β at 56 °C, blue line: second heating, with an endothermic peak at 69 °C Form β → Form γ, at 110 °C an exothermic peak related to the partial conversion of Form γ into Form α, and at 177 °C an endothermic peak Form γ + α → Form δ. (b) Heating cycle up to melting, black line: first heating, at 178 °C transition Form α, γ → Form δ, at 206 °C melting, red line: first cooling with three exothermic events recrystallization into Form δ at 205 °C, Form δ → Form γ at 165 °C, and Form γ → Form α at 143 °C, blue line: second heating, at 178 °C transition Form α, γ → Form δ, at 206 °C melting.

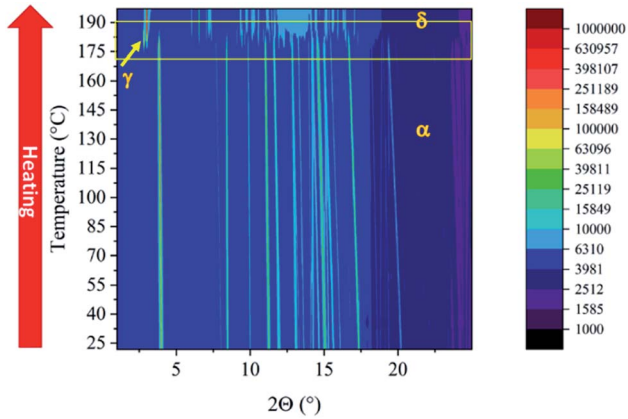

Fig. 3 VT-XRPD of **NDI-C6** at PSI synchrotron, 2D isolines of first heating until 195 °C with a transition of Form α → Form δ at 180 °C, and the presence of the Form γ peak is highlighted with an arrow.

already reported[27] with the Form δ → Form γ transition at 163 °C and followed the Form γ → Form β transition at 56 °C, ending up with Form β as a metastable phase at room temperature (Fig. 2a).

On the other hand, by heating up the sample above the melting point, we observed a different pathway. By recrystallization at 205 °C, Form δ was obtained which converted into Form γ at 165 °C; the latter, unexpectedly converted into Form α at 143 °C (Fig. 2b). The presence of Form α at RT was confirmed by the second heating which was characterized by the almost concomitant double transition at around 175 °C ending in Form δ. Furthermore, we confirmed this behaviour by VT-XRPD: the **NDI-C6** was melted and recrystallized on the sample stage. After melting, the sample is characterized by a strong preferential orientation, but the position of the first peak was used for the determination of the different phases and confirmed the presence of Form α at room temperature (see Fig. S3 in ESI†).

The thermal behaviour was studied by visual observation of the solid–solid transitions of **NDI-C6** by HSM. A crystal was heated above the melting point (214 °C), and then cooled at −10 °C min^{-1} as shown in Fig. 4. The liquid crystallized as Form δ at 203 °C, as observed also in DSC analysis. Decreasing the temperature, we observed a transition at 160 °C, that corresponded to the transition from Form δ to Form γ, then, at 145 °C, the transition Form γ → Form α occurred. No other transition was detected during the cooling, ending up with only Form α in the sample.

During the VT-XRPD collected at PSI, the sample was not melted and during the cooling, the transitions observed matched with the DSC analysis: Form δ converted into Form γ around 157 °C and then Form γ converted into Form β at 48 °C (see Fig. 2a and Fig. 5a). It is worth noting, that the remarkable thermal stability of Form γ was present in a temperature window of more than 100 °C and showed a high thermal contraction.

During the second heating, the DSC curve showed the conversion of Form β into Form γ at 69 °C then, an exothermic event occurred at 100 °C, which was

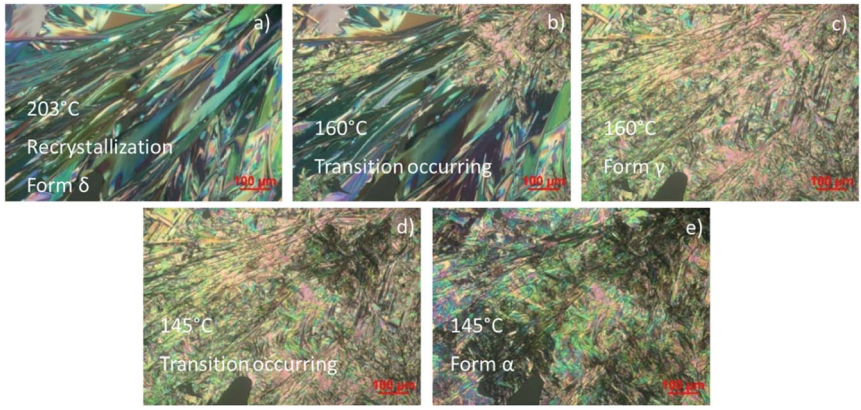

Fig. 4 Hot stage microscopy during the cooling after the melting of a single crystal **NDI-C6**, (a) recrystallization at 203 °C into Form δ, (b) Form δ → Form γ transition starting at 160 °C, (c) transition into Form γ completed, (d) transition Form γ → Form α occurring at 145 °C, (e) transition into Form α completed.

ascribed to the partial formation of Form α as confirmed by the VT-XRPD, see Fig. 5b. This event suggests that Form α is more stable than Form γ at temperatures lower than 175 °C, and that the conversion Form γ → Form α is promoted by the high temperature. In the temperature range 175–180 °C the two transitions – Form α → Form γ, and Form γ → Form δ – occurred.

The VT-XRPD data confirmed the behaviour observed in DSC, pure Form β is obtained by cooling the sample annealed to 195 °C (Fig. 5b) upon heating it converts into Form γ at 73 °C. It is worth noting that at around 108 °C the peaks associated with the interplanar distances 14.28 Å and 6.75 Å of Form α appeared, which are related to the exothermic transition observed in the DSC. Form α and

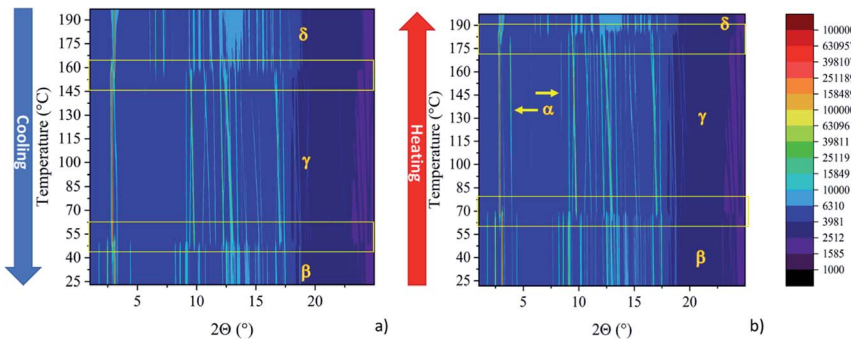

Fig. 5 VT-XRPD of **NDI-C6** at PSI synchrotron, (a) 2D isolines during first cooling from 195 °C to RT, starting at Form δ and ending at Form β. Two transitions are observable Form δ → Form γ at 157 °C and Form γ → Form β at 48 °C. (b) 2D isolines view of the second heating from RT to 195 °C, with two transitions: Form β → Form γ at 73 °C and Form γ → Form δ at 187 °C, it is also visible by the presence of two peaks of Form α, highlighted in the figure with arrows, the peak at lower 2θ is already present before the transition Form β → Form γ but the intensity increases considerably around 110 °C.

Form γ coexist up to 183 °C when Form α is fully converted into Form γ, then at 187 °C Form δ appears and the transition is completed at 190 °C.

The synergic approach of the different techniques allows us to rank the stability of the polymorphs: Form α is stable until 175 °C, then Form γ is stable until 178 °C when it converts into Form δ which is stable until the melting at 207 °C. Form β is always metastable but its energy should be between Form α and Form γ.

More difficult is rationalizing what causes the different thermal behaviour in cooling since they share common transitions: in fact, in both cases the high temperature Form δ converts into Form γ, only at this stage, the two pathways are observed. The different annealing process probably produces Form γ with different morphology or crystallinity which ends up in a different metastability of the crystals. When Form γ converts at high temperatures (145 °C) the thermal energy allows us to directly reach the stable Form α, instead, when the Form γ endures until 60 °C, it converts into Form β because the lower thermal energy is not enough to overcome the activation energy to reach Form α.

Thin films

We explored different combinations of solvent, deposition parameters and post-deposition treatment to obtain different films of different polymorphs. As expected, the crystal phases deposited are highly oriented and only the main peak is observed. The peak (100) of the Si at 33.00° (ref. 36) was used as the internal standard to determine the correct 2θ position of the peaks, and Table 2 summarizes the peak position used to identify the different phases.

By spin coating deposition of a low concentrated solution of **NDI-C6** in DCM, it was possible to obtain three different phases in the same film: Form α, Form β and a new form called Form ε, which was not observed before in the bulk analysis, Fig. 6. Form ε presents a strong peak at 5.2° that is not present in the other forms, and it clearly shows a new phase. Form ε was observed only in thin films crystallized on Si/SiO_2 substrates: it is worth noting that since Form ε could be obtained also by quenching the melted **NDI-C6** on Si/SiO_2 substrates, this suggests that the new form might be induced by the substrate.

By changing concentration, speed or the number of layers, we always obtained a mixture of phases with Form α always present.

In films prepared using CHF solutions, only the Form α and Form ε were present as a mixture. It was possible to obtain pure Form α by thermal annealing at 75 °C, Fig. 7.

By spin coating of toluene solutions with a speed of 1000 rpm, Form ε was obtained but it starts converting into Form β after a short time, Fig. 7.

Table 2 Peak position and related *hkl* plane observed in films of each phase

Form	d (Å)	*hkl*	2θ (°)
Form α	14.3	(001)	6.2
Form β	18.3	(001)	4.9
Form γ	19.8	(001)	4.4
Form δ	19.0	(002)	4.6
Form ε	17.0	—	5.2

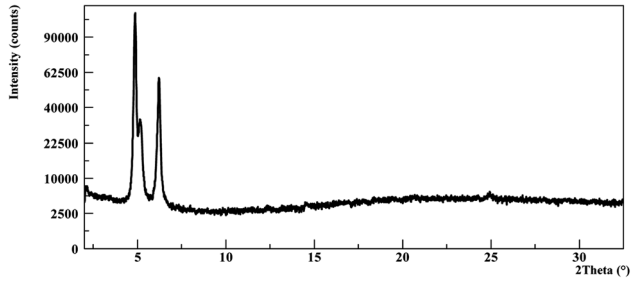

Fig. 6 Thin film prepared with a DCM solution showing a mixture of three different phases (Form α, Form β and Form ε).

A Form γ film is obtained by thermal treatment of Form β film at 75 °C (Fig. 7).

It is worth noting that the more polar and volatile solvents (DCM and CHF) favour the deposition of the stable Form α, although always concomitant with other metastable phases (Form β and Form ε) potentially promoted by the fast evaporation of the solvent. Toluene, on the other hand, favours the presence of ε, and despite being a high boiling solvent, the stable Form α is hardly observed. The main peaks observed in the thin films are ascribable to the alignment of the molecules on the substrate and it is worth noting that the β, γ and ε are characterized by peaks at lower angles than α, which indicates that **NDI-C6** molecules are less tilted in respect to the substrate as observed for the γ phase. The longer planar distance is also induced by different conformation of the chains as discussed in the next section.

Crystal structure

Structure solution of Form γ was obtained by simulated annealing with TOPAS 5. The X-ray powder pattern of Form γ at 54 °C was indexed with a triclinic cell with a volume comparable with the molecular volume, the simulated annealing was performed with a half molecule constrained on the inversion centre.

As observed for the NDI-C*n* molecules, the overall structures can be described as the stacking of layers of molecules, showing on the interface the alkyl chains. Conformation and length of the chains play a key role in the final structure tuning the aromatic core interactions. In Form γ, the alkyl chains of **NDI-C6** present

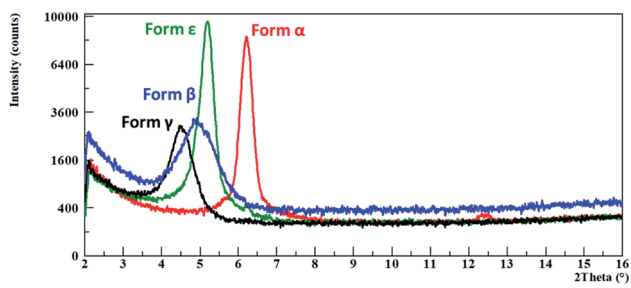

Fig. 7 Thin films of the different phases, identified by the characteristic peak of each phase, Form α in red, Form β in blue, Form γ in black and Form ε in green.

a quite different conformation in respect to Form α, although the carbon atoms do not adopt a full *anti* conformation, the chain is stretched, increasing the long axis of the molecule (see Fig. 8a and b). In both structures, the molecules form π–π interactions, with mainly columnar packing, the interplanar distance of Form γ is slightly longer than in Form α (3.5 Å instead of 3.4 Å), which allows the nearby columns to get tighter (see Fig. 8c and d). The different arrangement of the aromatic core can be better evaluated with the use of the stacking vector (SV) and the angles χ and ψ as described by Milita *et al.*[27] The SVs are similar in both Form α and Form γ (4.90 Å and 4.86 Å respectively), but they have quite a different orientation, hence different χ and ψ values (76.0° and 46.4° in Form α and 64.7° and 58.4° in Form γ). The clustering of the different χ/ψ values for the NDI-C*n* shows two different stacking modes, one for the short alkyl chains ($n < 7$) and the other for the longer ones. Interestingly the values obtained for Form γ are closer to the group of longer chains, where the energy contribution of the chains is predominant.

The thin films of Form α and Form γ are highly orientated and in both cases the highest peak is due to the crystallographic plane (001), which means that the planes (00*l*) are parallel to the substrate. Fig. 9 shows how the molecules of Form

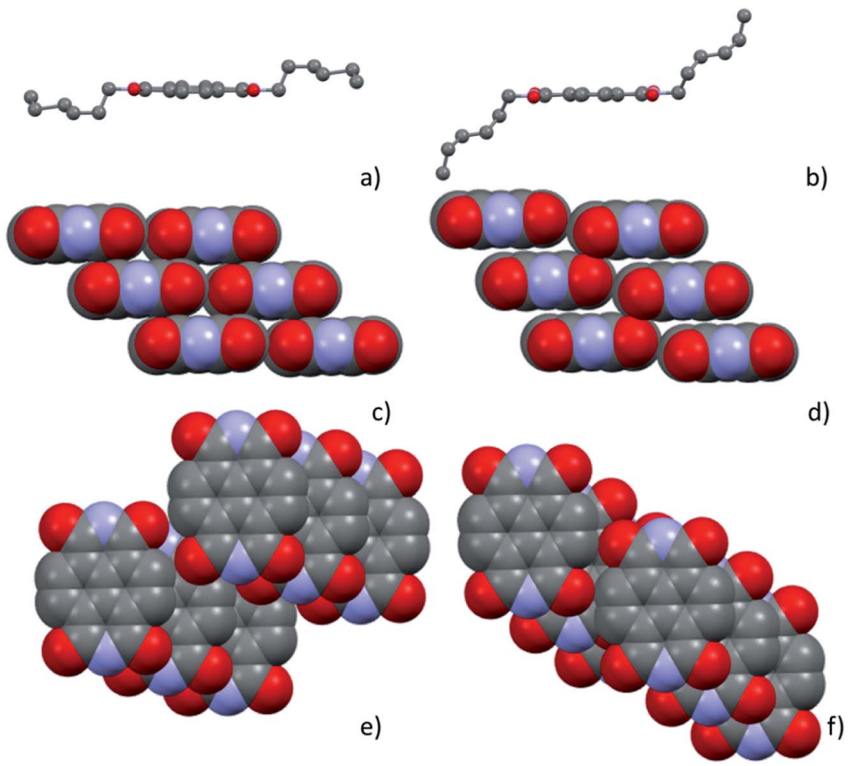

Fig. 8 Comparison of the structure of Form α (left) and Form γ (right): (a and b) different conformation of the chains in the NDI-C6 structures (hydrogen omitted for clarity); (c and d) columnar arrangement of the aromatic core, view along the long direction of the aromatic core; (e and f) columnar arrangement of the aromatic core, view perpendicular to the aromatic core. In c–f hydrogen atoms and alkyl chains are omitted for clarity.

α and Form γ are organized on the substrate, and since in Form γ the **NDI-C6** molecules are less tilted in respect to the substrate than in Form α, the $d_{0\ 0\ 1}$ is longer and the first peak is observed at a lower 2θ angle than the peak of Form α.

Thermal expansion calculation

As mentioned previously, **NDI-C6** presents a big thermal expansion that could be noticed by the peak shift in the VT-XRPD. To have better insight into the thermal expansion mechanism, we used PASCal to analyse Form α and Form γ. The principal axis coefficients and the orientation of the tensors are summarized in Table 3.[35] It is worth noting that the tensors are a set of orthogonal axes (the principal axes) along which the material responds in a purely linear fashion, and in the case of the triclinic system they are not related to the unit-cell axes.

Looking at the results obtained, we can immediately see that both polymorphs have a negative thermal expansion (NTE) along one principal axis, this behaviour is uncommon but it has been described in different materials before, for example in BHH-BTBT.[37,38]

In Form α, the highest positive thermal expansion positive thermal expansion (PTE) of 308 MK^{-1} can be considered a huge expansion[39] and it affects the distances between the layers (see Fig. 10a), which involves mainly the alkyl chains, while the NTE occurs inside the layer and affects mainly the distances between the side-by-side aromatic core, these two effects promote the conversion into Form γ, where the alkyl chains are more stretched, and the columns are closer. As observed before, increasing the temperature allows to reach this new family of phases where the arrangement of the aromatic core is closer to the one observed for the NDIs with long chains and the molecules are less tilted with respect to the (0 0 1) plane, which can be detected by the first peak as low 2θ values.

It is worth noting that in Form γ the thermal expansion is highly anisotropic, with a colossal NTE ($X1 = -292$ MK^{-1}) and a massive PTE ($X3 = 552$ MK^{-1}) using the notation proposed by Goodwin *et al.*[39] and Henke *et al.*[40] In Fig. 10b the $X1$ and $X3$ are reported, and considering that the component of $X1$, $X2$ and $X3$ along the c

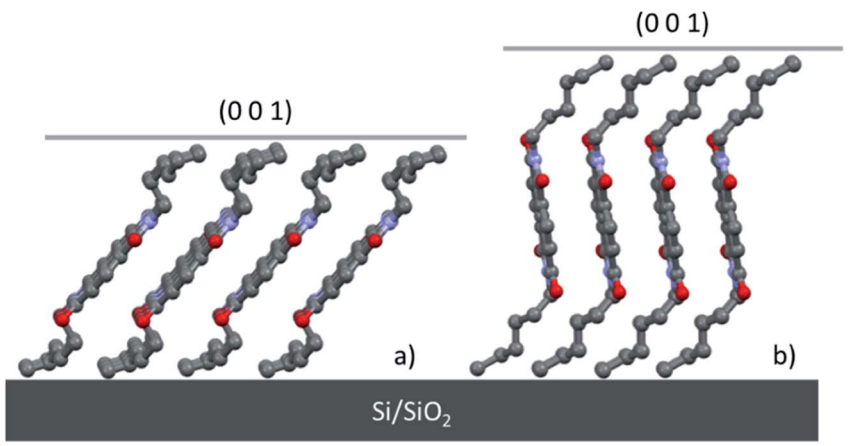

Fig. 9 Molecular arrangement of thin films oriented in the Si/SiO_2 substrates of (a) Form α and (b) Form γ.

Table 3 Values (α_X) of the principal axis of thermal expansion (*X*1, *X*2 and *X*3) and their orientation in regards to the cell axis, *a*, *b* and *c* for both Form α and Form γ

	Principal axis	α_X (MK^{-1})	*a*	*b*	*c*
Form α	*X*1	−87	−0.3966	−0.9180	0.0040
	*X*2	133	0.9847	−0.0715	0.1590
	*X*3	308	−0.6626	0.2685	0.6992
Form γ	*X*1	−292	0.1631	0.9478	−0.2740
	*X*2	193	0.9613	−0.2584	−0.0957
	*X*3	552	−0.7771	−0.5966	−0.2005

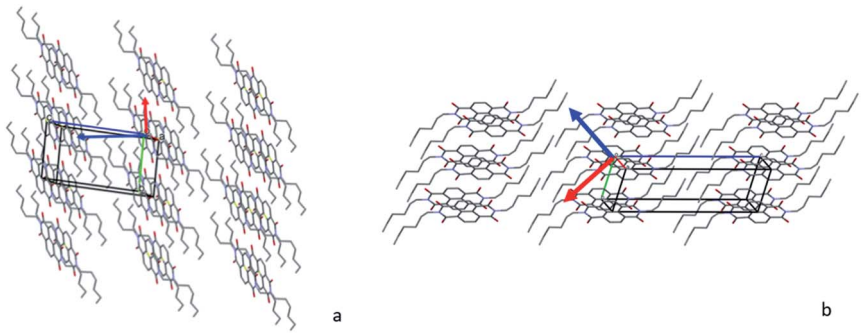

Fig. 10 Packing of the structures with *X*2 perpendicular to the figure, *X*1 in red and *X*3 in blue. The arrows indicate the direction of the tensors: (a) Form α and (b) Form γ.

axis are limited, it suggests that the main rearrangement occurs in the intralayer and the tilt of the molecules. This behaviour can explain the different thermal pathways, when the transition Form γ → Form α occurs at high temperature, it is possible to rearrange the chains and reach the stable Form α. On the other hand, if Form γ reaches a low temperature, the contraction that occurs during the cooling, which involves mainly the layer, compresses the alkyl chains preventing their folding, and instead of Form α, Form β is obtained, which is characterized by a longer axis.

Conclusion

We have studied in detail the thermal behaviour of **NDI-C6**, already known for the high number of polymorphs that can be detected by varying temperature. The careful study of the transition allowed us to determine the stability of the different polymorphs: Form α is stable up to 175 °C, then Form γ is stable until 178 °C when it converts into Form δ which is stable until it melts at 207 °C. Form β is always metastable and its energy is supposed to be between Form α and Form γ. This study revealed that depending on the thermal history, it is possible to achieve different phases at RT: Form α or Form β. The former is obtained by cooling of the melt while the latter is obtained by annealing until below the melting point (206 °C), this phase is metastable at RT, and it reconverts into Form α over time.

We were able to determine the crystal structure of Form γ, where the **NDI-C6** presents almost stretched alkyl chains, and an overall packing closer to the structure of NDI-C_n with $n > 7$. Form α and Form γ present exceptionally high PTE and NTE values, and the analysis of the principal coefficients of thermal expansion gave us insight into the solid–solid transition. In Form α, the highest PTE influences mainly the interlayer distance and upon heating, promotes the stretching of the alkyl chains and thus the conversions to Form γ. On the other hand, colossal NTE and massive PTE calculated on Form γ, are predominant in the *ab* plane, hence in the arrangement of the aromatic cores. Upon cooling, if the transition to Form α does not occur at high temperature, Form γ reaches low temperatures, and the contraction that occurs during the cooling prevents the folding of the alkyl chains and instead of Form α, Form β is obtained, which is characterized by a longer axis.

By different combinations of solvent, speed of deposition and thermal annealing, it was possible to obtain pure phases on the thin film. DCM and CHF promoted the formation of a mixture of Form α with different phases, while, by deposition of toluene solutions, a new polymorph labelled Form ε was observed. The new form is metastable and converts into Form β over time. Pure Form α and γ were obtained by thermal annealing at 75 °C for 1 h of the sample obtained with DCM and TOL solution, respectively. Form ε has been observed only on Si/SiO_2 substrates and further investigations are planned to confirm that it is a substrate-induced polymorph.

Author contributions

Inês de Oliveira Martins: investigation, experimental and computational analysis and writing of the manuscript. Francesco Marin: experimental and computational analysis. Enrico Modena: conceptualization and supervision. Lucia Maini: supervision, manuscript review and editing.

Conflicts of interest

The authors declare no conflicts of interest

Acknowledgements

We acknowledge the Paul Scherrer Institut, Villigen, Switzerland for provision of synchrotron radiation beamtime at beam-line MS-X04SA of the SLS (ID proposal 20201790) and would like to thank Nicola P. M. Casati for assistance. This project has received funding from the European Union's Horizon 2020 research and innovation programme under the Marie Skłodowska-Curie grant agreement no. 811284 (UHMob).

References

1 Y. Diao, L. Shaw, Z. Bao and S. C. B. Mannsfeld, Morphology Control Strategies for Solution-Processed Organic Semiconductor Thin Films, *Energy Environ. Sci.*, 2014, **7**, 2145–2159, DOI: 10.1039/c4ee00688g.

2 J. Mei, Y. Diao, A. L. Appleton, L. Fang and Z. Bao, Integrated Materials Design of Organic Semiconductors for Field-Effect Transistors, *J. Am. Chem. Soc.*, 2013, **135**(18), 6724–6746, DOI: 10.1021/ja400881n.
3 X. Gao and Z. Zhao, High Mobility Organic Semiconductors for Field-Effect Transistors, *Sci. China: Chem.*, 2015, **58**(6), 947–968, DOI: 10.1007/s11426-015-5399-5.
4 C. Zhao, A. Li, X. Chen, M. U. Ali and H. Meng, Hysteresis Effect in Organic Thin Film Transistors Based on Naphthalene Tetracarboxylic Diimide Derivatives, *Appl. Phys. Lett.*, 2021, **118**, 193302, DOI: 10.1063/5.0045183.
5 K. Fukuda, Y. Takeda, M. Mizukami, D. Kumaki and S. Tokito, Fully Solution-Processed Flexible Organic Thin Film Transistor Arrays with High Mobility and Exceptional Uniformity, *Sci. Rep.*, 2014, **4**, 3947, DOI: 10.1038/srep03947.
6 S. Riera-Galindo, A. Tamayo and M. Mas-Torrent, Role of Polymorphism and Thin-Film Morphology in Organic Semiconductors Processed by Solution Shearing, *ACS Omega*, 2018, **3**, 2329–2339, DOI: 10.1021/acsomega.8b00043.
7 H. Chung and Y. Diao, Polymorphism as an Emerging Design Strategy for High Performance Organic Electronics, *J. Mater. Chem. C*, 2016, **4**(18), 3915–3933, DOI: 10.1039/c5tc04390e.
8 X. Gao and Y. Hu, Development of N-Type Organic Semiconductors for Thin Film Transistors : A Viewpoint of Molecular Design, *J. Mater. Chem. C*, 2014, **17**, 3099–3117, DOI: 10.1039/c3tc32046d.
9 E. Benvenuti, D. Gentili, F. Chiarella, A. Portone, M. Barra, M. Cecchini, C. Cappuccino, M. Zambianchi, S. G. Lopez, T. Salzillo, E. Venuti, A. Cassinese, D. Pisignano, L. Persano, M. Cavallini, L. Maini, M. Melucci, M. Muccini and S. Toffanin, Tuning Polymorphism in 2,3-Thienoimide Capped Oligothiophene Based Field-Effect Transistors by Implementing Vacuum and Solution Deposition Methods, *J. Mater. Chem. C*, 2018, **6**(21), 5601–5608, DOI: 10.1039/c8tc00544c.
10 C. Cappuccino, S. Canola, G. Montanari, S. G. Lopez, S. Toffanin, M. Melucci, F. Negri and L. Maini, One Molecule, Four Colors: Discovering the Polymorphs of a Thieno(Bis)Imide Oligomer, *Cryst. Growth Des.*, 2019, **19**, 2594–2603, DOI: 10.1021/acs.cgd.8b01712.
11 C. Cappuccino, L. Catalano, F. Marin, G. Dushaq, G. Raj, M. Rasras, R. Rezgui, M. Zambianchi, M. Melucci, P. Naumov and L. Maini, Structure–Mechanical Relationships in Polymorphs of an Organic Semiconductor (C4-NT3N), *Cryst. Growth Des.*, 2020, **20**, 884–891, DOI: 10.1021/acs.cgd.9b01281.
12 M. Mas-Torrent and C. Rovira, Role of Molecular Order and Solid-State Structure in Organic Field-Effect Transistors, *Chem. Rev.*, 2011, **111**(8), 4833–4856, DOI: 10.1021/cr100142w.
13 Y. Zhen, H. Dong, L. Jiang and W. Hu, Tailoring Crystal Polymorphs of Organic Semiconductors towards High-Performance Field-Effect Transistors, *Chin. Chem. Lett.*, 2016, **27**(8), 1330–1338, DOI: 10.1016/j.cclet.2016.06.023.
14 D. Liu, X. Xiao, Z. He, J. Tan, L. Wang, B. Shan and Q. Miao, Control of Polymorphism in Solution-Processed Organic Thin Film Transistors by Self-Assembled Monolayers, *Sci. China: Chem.*, 2020, **63**(9), 1221–1229, DOI: 10.1007/s11426-020-9793-2.
15 T. Salzillo, A. Campos, A. Babuji, R. Santiago, S. T. Bromley, C. Ocal, E. Barrena, R. Jouclas, C. Ruzie, G. Schweicher, Y. H. Geerts and M. Mas-torrent, Enhancing Long-Term Device Stability Using Thin Film Blends of

Small Molecule Semiconductors and Insulating Polymers to Trap Surface-Induced Polymorphs, *Adv. Funct. Mater.*, 2020, 2006115, DOI: 10.1002/adfm.202006115.

16 A. O. F. Jones, B. Chattopadhyay, Y. H. Geerts and R. Resel, Substrate-Induced and Thin-Film Phases : Polymorphism of Organic Materials on Surfaces, *Adv. Funct. Mater.*, 2016, **26**, 2233–2255, DOI: 10.1002/adfm.201503169.

17 L. Pithan, D. Nabok, C. Cocchi, P. Beyer, G. Duva, J. Simbrunner, C. Nicklin, P. Schäfer, C. Draxl, F. Schreiber, S. Kowarik, L. Pithan, D. Nabok, C. Cocchi, P. Beyer, G. Duva, F. Schreiber and S. Kowarik, Molecular Structure of the Substrate-Induced Thin-Film Phase of Tetracene, *J. Chem. Phys.*, 2018, **149**, 144701, DOI: 10.1063/1.5043379.

18 D. Reischl, C. Ro, P. Christian, E. Roblegg, H. M. A. Ehmann, I. Salzmann and O. Werzer, Surface-Induced Polymorphism as a Tool for Enhanced Dissolution: The Example of Phenytoin, *Cryst. Growth Des.*, 2015, **15**, 4687–4693, DOI: 10.1021/acs.cgd.5b01002.

19 A. O. F. Jones, Y. H. Geerts, J. Karpinska, A. R. Kennedy, R. Resel, C. Röthel, C. Ruzié, O. Werzer and M. Sferrazza, Substrate-Induced Phase of a [1]Benzothieno[3,2-*b*]Benzothiophene Derivative and Phase Evolution by Aging and Solvent Vapor Annealing, *ACS Appl. Mater. Interfaces*, 2015, **7**, 1868–1873, DOI: 10.1021/am5075908.

20 O. D. Jurchescu, Conductivity Measurements of Organic Materials Using Field-Effect Transistors (FETs) and Space-Charge-Limited Current (SCLC) Technique, in *Handbook of Organic Materials for Optical and (Opto)electronic Devices*, Woodhead Publishing Limited, 2013, pp. 377–383, DOI: 10.1533/9780857098764.2.377.

21 S. V. Bhosale, M. Al Kobaisi, R. W. Jadhav, P. P. Morajkar, L. A. Jones and S. George, Naphthalene Diimides : Perspectives and Promise, *Chem. Soc. Rev.*, 2021, **50**, 9845–9998, DOI: 10.1039/d0cs00239a.

22 Z. Ma, H. Geng, D. Wang and Z. Shuai, Influence of Alkyl Side-Chain Length on the Carrier Mobility in Organic Semiconductors : Herringbone *vs.* Pi–Pi Stacking, *J. Mater. Chem. C*, 2016, **4**(20), 22–24, DOI: 10.1039/c6tc00755d.

23 X. Guo, F. S. Kim, M. J. Seger, S. A. Jenekhe and M. D. Watson, Naphthalene Diimide-Based Polymer Semiconductors: Synthesis, Structure–Property Correlations, and n-Channel and Ambipolar Field-Effect Transistors, *Chem. Mater.*, 2012, **24**, 1434–1442, DOI: 10.1021/cm2034273.

24 D. Shukla, S. F. Nelson, D. C. Freeman, M. Rajeswaran, W. G. Ahearn, D. M. Meyer and J. T. Carey, Thin-Film Morphology Control in Naphthalene-Diimide-Based Semiconductors : High Mobility n-Type Semiconductor for Organic Thin-Film Transistors, *Chem. Mater.*, 2008, **20**(24), 7486–7491.

25 X. Chen, Y. He, M. U. Ali, Y. He, Y. Zhu, A. Li, C. Zhao, I. F. Perepichka and H. Meng, Isothianaphthene Diimide : An Air-Stable n-Type Semiconductor, *Sci. China: Chem.*, 2019, **62**, 1360–1364.

26 A. Welford, S. Maniam, E. Gann, X. Jiao, L. Thomsen, S. J. Langford and C. R. Mcneill, Influence of Alkyl Side-Chain Type and Length on the Thin Film Microstructure and OFET Performance of Naphthalene Diimide-Based Organic Semiconductors, *Org. Electron.*, 2019, **75**, 105378, DOI: 10.1016/j.orgel.2019.105378.

27 S. Milita, F. Liscio, L. Cowen, M. Cavallini, B. A. Drain, T. Degoussée, S. Luong, O. Fenwick, A. Guagliardi, B. C. Schroeder and N. Masciocchi, Polymorphism

in *N*,*N*'-Dialkyl-Naphthalene Diimides, *J. Mater. Chem. C*, 2020, **8**, 3097–3112, DOI: 10.1039/c9tc06967d.

28 D. Shukla, S. F. Nelson, D. C. Freeman, M. Rajeswaran, W. G. Ahearn, D. M. Meyer and J. T. Carey, Thin-Film Morphology Control in Naphthalene-Diimide-Based Semiconductors : High Mobility n-Type Semiconductor for Organic Thin-Film Transistors, *Chem. Mater.*, 2008, **20**(4), 7486–7491.

29 S. Ali, M. A. Jameel, A. Gupta, S. J. Langford and M. Shafiei, Capacitive Humidity Sensing Performance of Naphthalene Diimide Derivatives at Ambient Temperature, *Synth. Met.*, 2021, **275**, 116739, DOI: 10.1016/j.synthmet.2021.116739.

30 S. Cho, K. Lee, J. Yuen, G. Wang, D. Moses, A. J. Heeger, M. Surin and R. Lazzaroni, Thermal Annealing-Induced Enhancement of the Field-Effect Mobility of Regioregular Poly(3-Hexylthiophene) Films, *J. Appl. Phys.*, 2006, 114503, DOI: 10.1063/1.2400796.

31 Y. Yuan, G. Giri, A. L. Ayzner, A. P. Zoombelt, S. C. B. Mannsfeld, J. Chen, D. Nordlund, M. F. Toney, J. Huang and Z. Bao, Ultra-High Mobility Transparent Organic Thin Film Transistors Grown by an off-Centre Spin-Coating Method, *Nat. Commun.*, 2014, **5**, 3005, DOI: 10.1038/ncomms4005.

32 P. R. Willmott, D. Meister, S. J. Leake, M. Lange, A. Bergamaschi, M. Böge, M. Calvi, C. Cancellieri, N. Casati, A. Cervellino, Q. Chen, C. David, U. Flechsig, F. Gozzo, B. Henrich, S. Jäggi-Spielmann, B. Jakob, I. Kalichava, P. Karvinen, J. Krempasky, A. Lüdeke, R. Lüscher, S. Maag, C. Quitmann, M. L. Reinle-Schmitt, T. Schmidt, B. Schmitt, A. Streun, I. Vartiainen, M. Vitins, X. Wang and R. Wullschleger, The Materials Science Beamline Upgrade at the Swiss Light Source, *J. Synchrotron Radiat.*, 2013, **20**(5), 667–682, DOI: 10.1107/S0909049513018475.

33 A. A. Coelho, TOPAS and TOPAS-Academic: An Optimization Program Integrating Computer Algebra and Crystallographic Objects Written in C++: An, *J. Appl. Crystallogr.*, 2018, **51**(1), 210–218, DOI: 10.1107/S1600576718000183.

34 J. S. O. Evans, Advanced Input Files & Parametric Quantitative Analysis Using Topas, *Mater. Sci. Forum*, 2010, **651**, 1–9, DOI: 10.4028/www.scientific.net/MSF.651.1.

35 M. J. Cliffe and A. L. Goodwin, PASCal: A Principal Axis Strain Calculator for Thermal Expansion and Compressibility Determination, *J. Appl. Crystallogr.*, 2012, **45**(6), 1321–1329, DOI: 10.1107/S0021889812043026.

36 P. Zaumseil, High-Resolution Characterization of the Forbidden Si 200 and Si 222 Reflections, *J. Appl. Crystallogr.*, 2015, **48**, 528–532, DOI: 10.1107/S1600576715004732.

37 A. van Der Lee, G. H. Roche, G. Wantz, J. J. E. Moreau, O. J. Dautel and J. S. Filhol, Experimental and Theoretical Evidence of a Supercritical-like Transition in an Organic Semiconductor Presenting Colossal Uniaxial Negative Thermal Expansion, *Chem. Sci.*, 2018, **9**(16), 3948–3956, DOI: 10.1039/c8sc00159f.

38 Z. Liu, Q. Gao, J. Chen, J. Deng, K. Lin and X. Xing, Negative Thermal Expansion in Molecular Materials, *Chem. Commun.*, 2018, **54**, 5164–5176, DOI: 10.1039/c8cc01153b.

39 A. L. Goodwin, M. Calleja, M. J. Conterio, M. T. Dove, J. S. O. Evans, D. A. Keen, L. Peters and M. G. Tucker, Colossal Positive and Negative Thermal Expansion

in the Framework Material $Ag_3[Co(CN)_6]$, *Science*, 2008, **319**(5864), 794–797, DOI: 10.1126/science.1151442.

40 S. Henke, A. Schneemann and R. A. Fischer, Massive Anisotropic Thermal Expansion and Thermo-Responsive Breathing in Metal–Organic Frameworks Modulated by Linker Functionalization, *Adv. Funct. Mater.*, 2013, **23**(48), 5990–5996, DOI: 10.1002/adfm.201301256.

Chapter 3: Study of surface induced polymorphism of NDI-C6

Overview

The work present herein is a continuation of the work reported in the previous chapter, therefore the material explored is NDI-C6. This chapter focuses on exploring and understanding the crystal forms obtained in thin films.

A set of new skills were gained throughout this project which was done in part during my secondments at the Technische Universität Graz (TUGraz) (March-June 2020), under the supervision of Prof. Roland Resel, and at the University of Cambridge (April-July 2022), under the supervision of Prof Henning Sirringhaus.

While I was in TUGraz, I characterized the thin films using X-ray reflectivity and variable temperature X-ray reflectivity. Since my time in TUGraz was during the pandemic lockdown my access to the laboratory was limited and therefore the number of experiments was also limited.

In addition, I had the opportunity to later join the group of Prof. Roland Resel at Elettra Sincrotrone Trieste at the X-ray Diffraction 1 (XRD1) beamline to further characterize my samples and I learnt about grazing incidence XRD and how to analyze the results obtained from this technique.

At the University of Cambridge, I acquired knowledge on OFET fabrication, electrical characterization using a semiconductor parameter analyzer linked to a probe station and morphological characterization with AFM.

This page intentionally left blank

Study of surface induced polymorphism of NDI-C6

Introduction

Polymorphism, the ability of any compound to crystallize as more than one distinct crystal form, has been widely studied in bulk as opposed to polymorphism in thin films.[1–3] Thin film polymorphism is still a field minimally explored and more difficult to control and understand, nonetheless, it has been proved that molecule-substrate interactions can greatly influence the molecular packing by lowering the activation energy barriers, which causes heterogeneous crystallization.[1,4–6] Consequently, the crystal structure in the vicinity of a substrate does not always match the bulk structures.

These new crystal forms, called thin film phases or surface mediated phases were observed for the first time in thin films of pentacene which started the interest to study this phenomenon in organic semiconductor molecules.[5–10] More recently, these phases have been described as surface induced polymorphs and surface selected polymorphs. A surface induced phase (SIP) can be associated with a distorted bulk phase since usually the crystal parameters do not differ much from the ones of the bulk phases, while a surface selected phase does not show a relation with the bulk phases, and it is considered an authentic new structure.[11]

Once the crystal packing strongly affects the charge carrier mobility and the charge transport happens within a few molecular layers in the semiconductor-insulator interface, it is extremely important to study the formation of SIPs.[1,2,5,7,8,12] Even though the importance of SIPs cannot be denied, a systematic approach to study, identify, and characterize SIPs is not reported yet and only a small number of systems have been studied.[1,7,8,11]

N, N'-bis(n-hexyl)naphthalene-1,4,5,8-tetracarboxylicdiimide (NDI-C6), Figure 1, is a small-molecule n-type organic semiconductor with high electron affinity, and good electrical properties such as good charge carrier mobility and thermal and oxidative stability, what makes it a good candidate to organic electronics.[13,14] Moreover, it exhibits high solubility making it easy to produce films by solution-based processes like drop-casting and spin-coating, with different solvents. Which is a requisite during the screening of SIP to study the effect of different solvents, solute concentration and temperature in thin film formation since these factors can affect the crystallization process and promote different polymorphs.[15,16]

Furthermore, NDI-C6 has proven to be prone to create various polymorphs: Form α (the stable form at RT), Form β, Form γ and Form δ (all three obtained by thermal treatment and convert back to Form α at RT).[17,18] And the number of crystal forms is higher compared to similar molecules with shorter or longer chains. Recently we have also described the presence of a new phase, called Form ε, which can be classified as a SIP.[18]

In this work we study the influence of several deposition parameters such as solvent and solution concentration, in the deposited films. The stability of the films, both over a period of time and thermal, were also evaluated. With the optimized conditions to get films of pure phases, we studied the different polymorphs in thin films including the substrate induced polymorph Form ε using

GIXRD, what allowed us to get two possible cell parameters for Form ε. Furthermore, we also tried to characterize the different electrical properties of the different phases, by producing and characterizing OFETs using the optimized conditions to deposit the semiconductor layer with known crystal phases. The films were also characterized by AFM analysis to describe the morphology of the active layer.

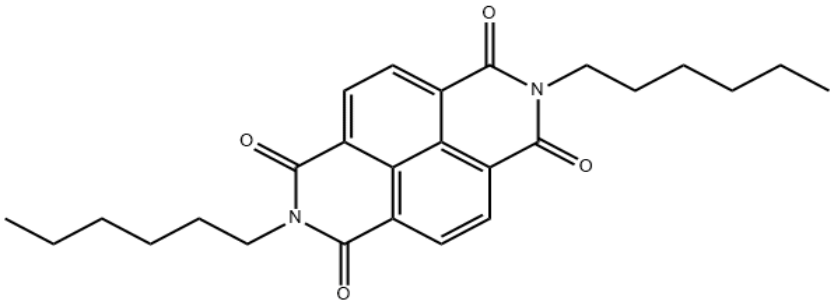

Figure 1 - Chemical structure of NDI-C6 molecule.

Experimental section

Materials

N, N'-bis(n-hexyl)naphthalene-1,4,5,8-tetracarboxylic diimide (NDI-C6) molecule is commercially available, it was purchased from Sigma-Aldrich and used as received.

Thin films deposition

Various thin films were fabricated by spin-coating on 1x1 cm^2 and 2x2 cm^2 SiO_2/Si substrates, previously cleaned by sonication in an acetone bath, followed by sonication in an ethanol bath and finally rinsed with deionised water and dried with compressed air. Deposition was carried out varying different process conditions such as solvent, concentration, and speed. In addition, thermal annealing at 75°C for 1 hour was performed for some samples.

X-ray reflectivity (XRR)

X-ray reflectivity measurements were performed with a PANalytical Empyrean diffractometer with Cu Kα (λ = 1.54178 Å) radiation from water cooled copper tube powered with 40 mA at 40 kV. The measurements were performed specularly, what means the incident and diffracted beam have the same angle to get out of plane information, with an incident angle between the 0-6°. The detector used was the PIXcel3D detector, a solid-state detector with 255x255 pixels of 55x55 μm size in 0D receiving slit mode using three open channels.

Variable temperature X-ray reflectivity (VT-XRR)

In situ variable temperature X-ray reflectivity was performed with the same specifications of the XRR described above, equipped with a DHS 900 heating stage. The heating stage was equipped with a dome to protect the sample from oxidation at high temperatures and to maintain the temperature controlled.

X-ray diffraction (XRD)

To identify the crystalline forms obtained in the deposited films, they were characterized by XRD in Bragg–Brentano geometry, with a Rigaku MiniFlex 600 diffractometer using a Cu Kα (λ = 1.54178 Å) radiation generated from a copper sealed tube with 40 kV and 15 mA, over the 2θ range of 3–40° with a step size of 0.01° and speed of 10.0°/min.

Grazing incidence X-ray diffraction (GIXRD)

To study the in-plane structure of the thin films, grazing incidence X-ray diffraction was performed at the Elettra Synchrotron in Trieste at the X-ray Diffraction 1 (XRD1) beamline. The beamline is equipped with a multipole wiggler photon source with a range of 4-21 keV, a cylindrical collimating mirror, a double-crystal Si(111) monochromator and a bendable toroidal focusing mirror. The Goniometer used is a Huber Kappa Goniometer. The detector is a Dectris Pilatus 2M detector with a CMOS hybrid-pixel technology operating in single-photon-counting mode.[19]

GIDVis

To visualize and analyse the grazing-incidence thin-film X-ray diffraction data obtained during sample rotation around the surface normal GIDVis was used. GIDVis is a software package based on MATLAB that allows the user to perform detector calibration, data stitching, intensity corrections, standard data evaluation and crystal phase analysis. [20]

GIDInd

GIDInd is automated indexing software based on the assumption of a triclinic unit cell with six lattice constants and a distinct contact plane parallel to the substrate surface. It was used to index and obtain the cell parameters of the unknown phase. The input data is taken from GIXRD results, and the output are unit cells reduced according to approved crystallographic conventions. [21]

Atomic force microscopy (AFM)

Atomic Force Microscopy (AFM) measurements were performed under ambient conditions in tapping mode using Asylum Research MFP-3D AFM System (Oxford Instruments) and TESPA-V2 probes (Bruker) with a nominal tip radius of 7 nm, 320 KHz frequency, and a spring constant of 37 N/m.

Devices fabrication

Organic field effect transistors (OFETs) with both bottom-gate bottom-contact and bottom-gate top-contact configurations were produced to characterize the performance of NDI-C6 based devices. Silicon wafers with thermally grown SiO_2 were used as substrate. The SiO_2/Si substrates were cleaned by sonication with a diluted Decon 90 solution for 10 min, followed by sonication in water, acetone, and IPA for 10 min in each solvent, and finally dried using a nitrogen gun. The organic semiconductor layer was deposited with the different optimized conditions and in the case of Form α and Form γ the films were annealed at 75°C for one hour. In the case of the bottom-contact configuration, chromium (5 nm) and gold (25 nm) were thermally evaporated onto the

substrate to form source and drain contacts using shadow masks. For the top-contact configuration only gold was thermally evaporated onto the semiconductor layer also using shadow masks.

Devices characterization

Transistors were characterized using an Agilent 4155B Semiconductor Parameter Analyzer and standard probe station setup at room temperature in an N_2-filled glovebox with H_2O and O_2 <5 ppm.

Results and Discussion

Different solvent and concentrations

Films of NDI-C6 were prepared at room temperature by spin-coating with a speed of 1000 rpm for 60 seconds, using toluene and dichloromethane. The solvents used were chosen due to the boiling point difference, 110°C for toluene and 40°C for dichloromethane, making the evaporation of solvent during the spin-coating significantly distinct to promote differences in the crystallization process and assess the formation of different polymorphs. It is reported that lower concentrations tend to form less densely packed crystal forms on the surface, [15] so different concentrations were tested to evaluate the influence of this parameter on the crystallization.

The five different polymorphs reported in chapter 2 can be easily identified by their characteristic peak position and corresponding hkl plane, reported in Table 1. [18]

Table 1 - Peak position and related hkl plane used to identify the different phases in films and their respective density.

Form	d (Å)	hkl	2θ (°)	Density (g/cm^3)
Form α	14.3	001	6.2	1.25
Form β	18.3	001	4.9	1.22
Form γ	19.8	001	4.4	1.20
Form δ	19.0	002	4.6	1.05
Form ε	17.0	-	5.2	-

By varying the concentration of the solutions, we were able to deposit different polymorphs. As expected, thicker films promote the formation of the most thermodynamic stable bulk phase Form α, even though it was always observed concomitantly with other phases.

Form ε was obtained as pure phase by spin coating a 1mg/mL dichloromethane solution, while by increasing the concentration of the solution the films obtained are a mixture of Form ε, Form α and Form β, Figure 2 a).

When we changed the solvent to toluene, by spin coating a 1 mg/mL solution led to the formation of pure Form β, while higher concentrations (1.5 mg/ml and 2.0 mg/ mL) lead to the formation of a mixture of Form ε, Form α and Form β, as shown in Figure 2 b)

From the study of the bulk polymorphism, it is known that Form β converts into Form α over time. Therefore, since the films were not characterized immediately after the deposition, it is difficult to claim surely if the films crystalize as a mixture of the three concomitant polymorphs or if the mixture is a result of the partial conversion of the less stable phases.

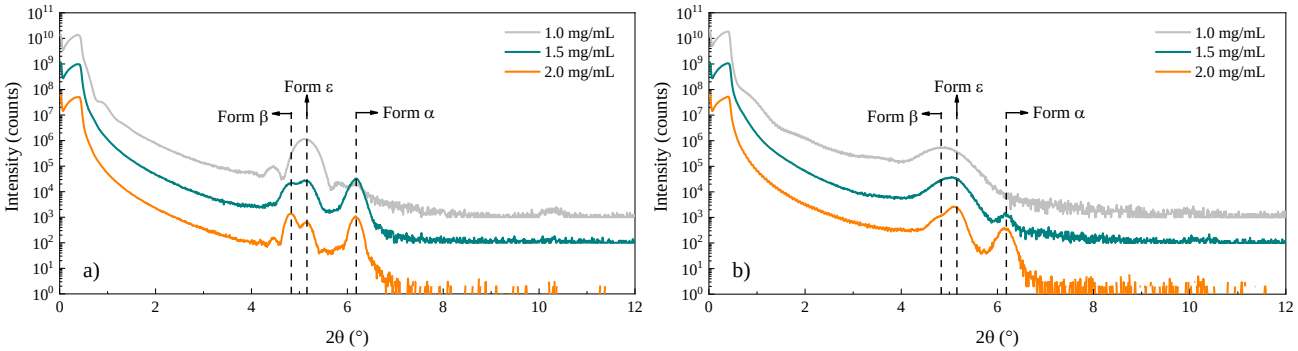

Figure 2 - X-ray reflectivity of thin films with different concentrations of a) dichloromethane solutions, b) toluene solutions.

Normally the surface-induced phases are ascribed to very thin films, as observed in the deposition of the dichloromethane solution, where increasing the concentration, increases the thickness of the film and promote the formation of the crystal phases observed in bulk. The results obtained by deposition of toluene solutions are difficult to explain, since the Form ε which is the SIP phase is observed not on the thinner layer obtained with the lowest concentration but on the thicker film concomitantly with Form α and Form β. This uncommon behavior led to a deeper study of the influence of the toluene solutions concentration in the films' polymorphs. Two additional concentrations have been considered (2.5 and 3.0 mg/mL).

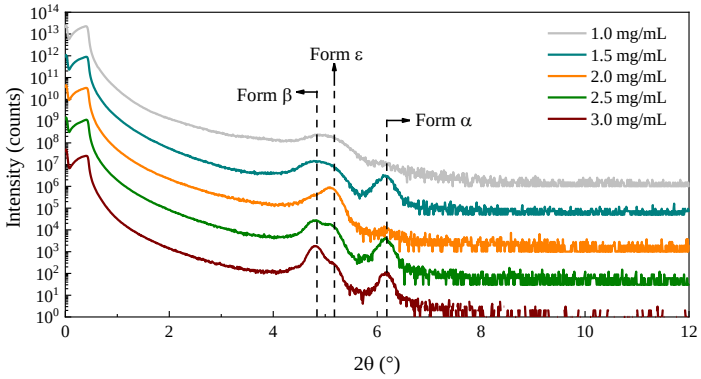

Figure 3 – X-ray reflectivity measurement of films produced with toluene solutions of different concentrations.

From the XRR patterns of the films deposited with toluene solutions of various concentrations, we can observe that even with a solution of 3mg/mL the films continue to be Form ε, Form β and Form α, Figure 3.

Stability over time

The stability of the thin films over time was checked by characterizing the samples again after 3-4 weeks. The sample preparation and the measurements were done in Spring 2020 during the pandemic lockdown, so it was not possible to keep the same interval of time for every sample.

Pure Form ε converts in Form α and Form γ after 20 days (see Figure 4 a). While after approximately 20 days the film of Form α, Form β and Form ε converts to Form α and Form β (Figure 4 b), it is worth noting that in this case, because the more stable Form α and Form β are observed in the film after deposition, Form ε converts directly to Form α and Form β and no Form γ is detected. These results make it safe to conclude that Form ε is less stable at room temperature than both Form α, Form β and Form γ.

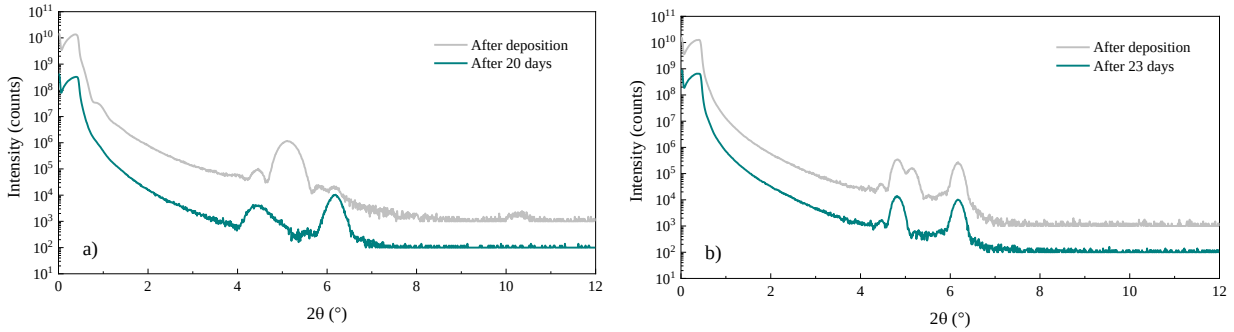

Figure 4 – Stability over time measured by x-ray reflectivity of films deposited with a) 1mg/ml dichloromethane solution and b) 2mg/ml dichloromethane solution.

The film of pure Form β was stable and in 30 days no other phases appeared (Figure 5 a). The film of Form α, Form β and Form ε produced with a toluene solution also stays unchanged even after a longer period of 45 days (Figure 5 b), in this case Form ε does not convert to the more stable forms. It is important to mention the difference between the films produced with dichloromethane and toluene, since the stability of films with the same phases, namely the mixture of Form α, Form β and Form ε, changes when different solvents are used.

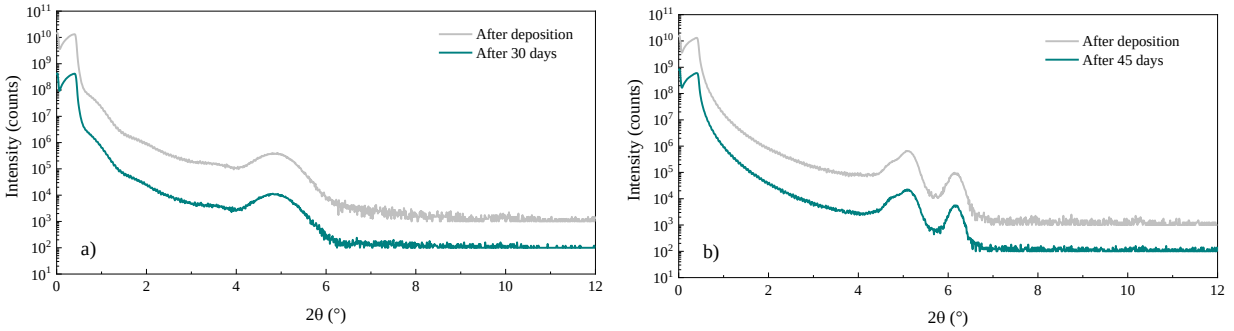

Figure 5 - Stability over time measured by x-ray reflectivity of films deposited with a) 1mg/ml toluene solution and b) 2 mg/ml toluene solution.

The films obtained using toluene solutions showed better long-term stability after more than one month, including in the films of Form ε. Hereupon, we focused on studying the stability of Form ε in a film produced with a 3 mg/mL toluene solution. The film was characterized by XRD immediately after the deposition and again 1 day and 4 days after the deposition, Figure 6.

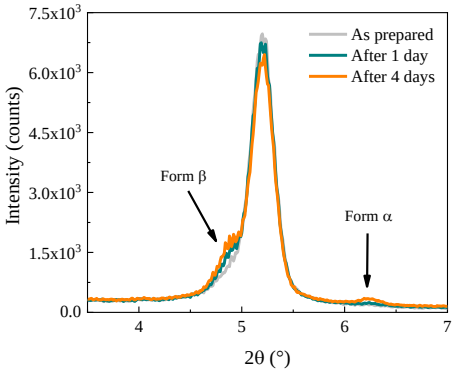

Figure 6 – XRD of Form ε right after deposition and after one and four days.

The stability analysis of the new thin film produced with a 3 mg/mL toluene solution showed a surprising result, immediately after the deposition the film is composed of only Form ε. After one day, the results showed already the presence of Form α and Form β peaks, and by the fourth day the intensity of the peaks of Form α and Form β increased while the peak of Form ε decreased in intensity. These results confirm that Form ε is a metastable phase with a tendency to convert over time at RT with no specific control of storage conditions. This observation suggests that the previously studied films that are a mixture of Form α, Form β and Form ε may be the result of the partial conversion of Form ε to Form α and Form β.

Thermal stability

We studied the thermal behavior of the films to better understand where Form ε fits in the stability ranking among the other polymorphs, for that in situ variable temperature XRR was performed. In this analysis, four different films (toluene 1mg/mL, toluene 2mg/mL, dichloromethane 1mg/mL and dichloromethane 2mg/mL) were characterized. Even though the films were characterized weeks after the deposition, what caused the conversion to most stable forms in some cases, it is still possible to draw conclusions from the thermal analysis.

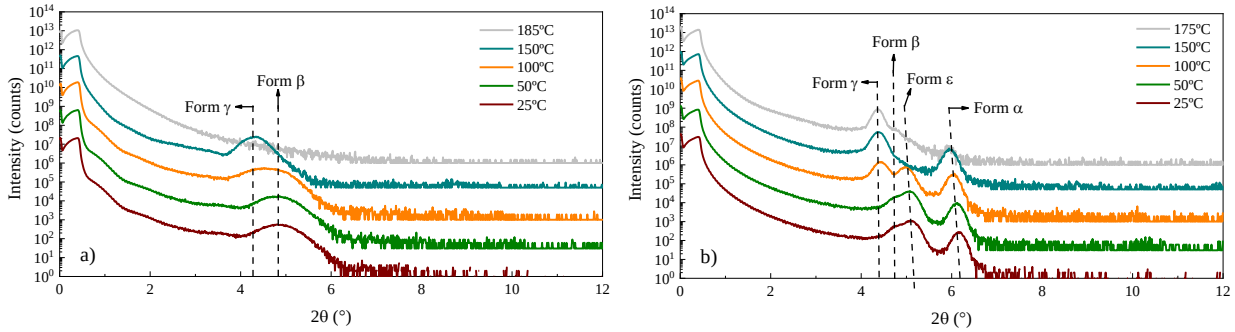

Figure 7 - In situ variable temperature X-ray reflectivity of films deposited with a) 1 mg/ml toluene solution, b) 2mg/ml toluene solution.

The film of pure Form β, is stable until 100°C and at 150°C has completely converted into Form γ, see Figure 7 a). From the bulk thermal analysis, this transition was already expected, however the results show that Form β is stable until higher temperatures in film, since when in bulk the transition Form β → Form γ is at approx. 70°C while in film is stable up to 100°C. At 185°C the

film has completely sublimed, and no signal is detected in the measurement, while in bulk it melts close to 215°C.

The film of Form α, Form β and Form ε remains stable until 50°C and at 100°C Form β converts into Form γ making the film a mixture of Form α, Form γ and Form ε. Further in the heating, at 150°C, it can be observed the complete disappearing of Form ε and only Form α and Form γ are present in the film. Lastly, Form α converts into Form γ and the film ends up as pure Form γ at 175°C, see Figure 7 b). In addition, a slight shift in the peak position can be observed during the heating due to thermal expansion.

By the temperature involved in the transitions it is possible to determine the stability ranking of the different polymorphs in thin film. The ranking can be described as: Form α is stable from RT until 150°C, Form β is metastable from RT up to around 100°C, Form ε is also metastable in the range of RT-150°C and Form γ is stable from 150°C until sublimation of the film around 180°C. At least within the experimental conditions investigated, it was not possible to get Form δ in film, the polymorph that is stable in bulk from 178°C until the melt at 207°C.[18]

Thin films of pure phases

To be able to study more in deep the different polymorphs in thin film, the deposition conditions were optimized to obtain pure phases in films, these results are described in our previous work and can be consulted at Table 2. The films were characterized by XRD immediately after the deposition to confirm the crystal form obtained, and all the polymorphs were pure right after deposition.

Table 2 – Deposition parameters used to obtain pure phases in thin films.

Polymorph	Solvent	Concentration	Speed	Thermal annealing
Form α	Chloroform	1 mg/mL	750 rpm	Yes
Form β	Toluene	1 mg/mL	1000 rpm	No
Form γ				Yes
Form ε		3 mg/mL	1000 rpm	No

Using the conditions reported in Table 2, several batches of films were produced and characterized, and the results were consistent. The films were characterized by XRD during the optimization, Figure 8, and since the crystal phases deposited are highly oriented, only the main peak is observed and it is related to the (001) plane for Form α, Form β and Form γ. In the case of Form ε, the plane associated with the peak observed cannot be described with certainty as the cell parameters are not known.

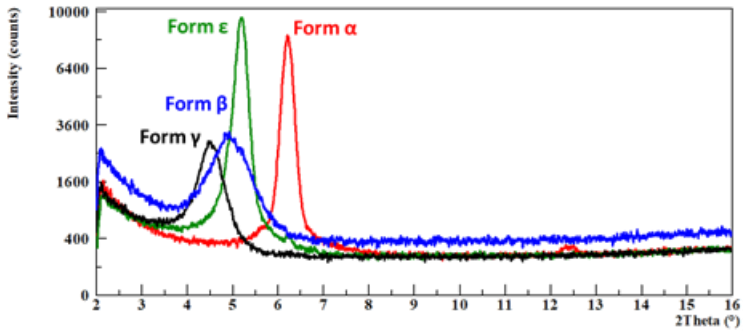

Figure 8 - Thin films of the different phases, identified by the characteristic peak of each phase, Form α in red, Form β in blue, Form γ in black and Form ε in green.

The films were also characterized by GIXRD to distinguish the crystal phases present in the films. We used GIDVis as a tool to visualize and index the peaks present based on the cell parameters known for each polymorph. It was possible to confirm that the films of Form α and Form γ were indeed pure, as showed in Figure 9, while the film of Form β show fuzzy and blurred spots which makes it harder to identify the peaks.

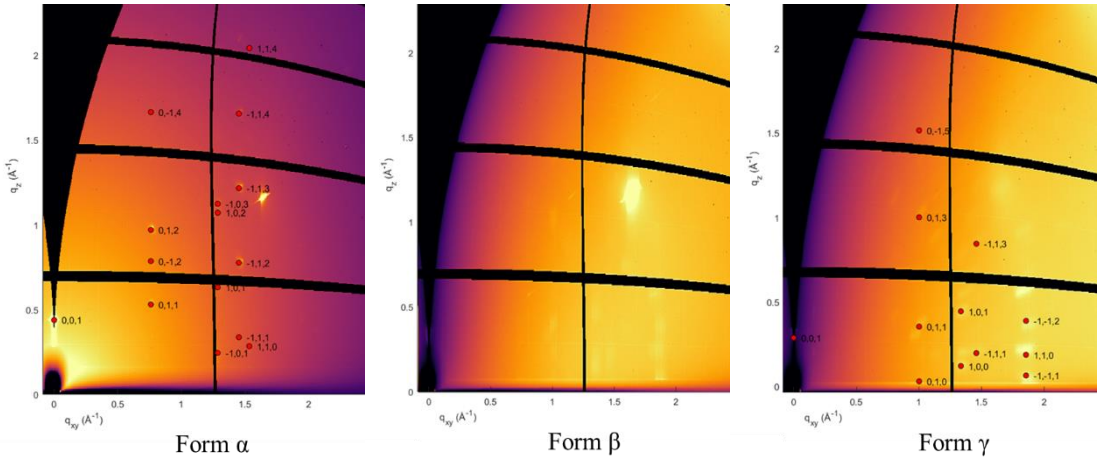

Figure 9 – Identification of hkl planes of each peak of Form α, Form β and Form γ.

In the case of Form ε, since there is no crystal structure or cell parameters reported, GIDInd was used to index the peaks referring to Form ε to get the cell parameters of the surface induced phase, this was quite challenging since the films of Form ε are never pure by the time of the characterization. Manual indexation was also performed by changing the cell parameters until a good fit between the peaks present in the data and the calculated peaks is obtained. The cells obtained with both methods can be consulted at Table 3. It is noteworthy the value of the c axis, normally associated with the length of the layers, around 17Å in both cells, this value also coincides with the d-spacing obtained from the first and only observable peak of the XRD data.

Table 3 - Cell parameters of Form ε obtained by indexation of GIXRD data.

	a (Å)	b (Å)	c (Å)	α (°)	β (°)	γ (°)
GIDInd	4.84	8.69	17.41	83.88	85.06	81.61
Manually	4.70	8.20	17.80	96.70	95.60	85.10

OFET fabrication

Even though Form ε is known to be very metastable, OFETs were fabricated with the four polymorphs obtained in thin films. Initially bottom gate bottom contact devices were fabricated by depositing gold contacts with a thin layer of chromium to improve the gold adhesion on Si/SiO_2 substrates, but for all the different polymorphs the transfer curves of the devices did not show any drain current for all the gate voltages. With this architecture, OFETs were fabricated with and without ODTS treatment of the surface before the semiconductor deposition; in both cases it was observed the same behavior described before, i.e., no drain current.

Later we changed the architecture to bottom gate top contact devices and produced devices with and without ODTS treatment. The behavior of the devices produced without ODTS with different polymorphs can be observed in Figure 10.

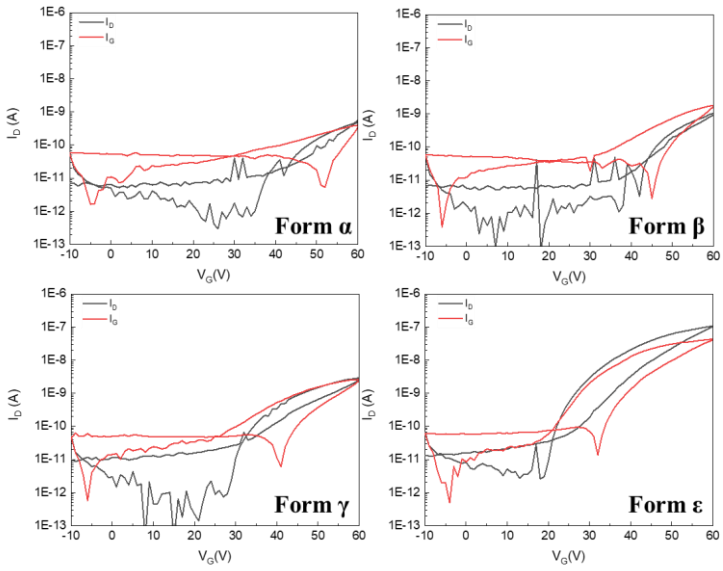

Figure 10 - Transfer characteristics of different polymorphs of NDI-C6.

The devices characterized do not show an ideal behavior as the drain current is always very low and in the case of higher ON current the gate current is also high and follows the trend of the drain current. This behavior was observed in all the batches fabricated even when changing the Si/SiO_2 wafer.

Another important characteristic of thin films is the morphology since it can significantly influence charge transport along polycrystalline films. To have an insight into how the different polymorphs crystallize in the substrate AFM was performed. At first instance, Form ε looks like having the best electronic properties when compared to the other crystal forms, since the devices show higher ON current but if we take a closer look to the film morphology, Figure 11, we can observe that all the films have a very different morphology, yet none of the films show good coverage or good uniformity. The thickness of the films is between 25-30nm in all cases, even though it is normally a suitable thickness in the field of organic electronics, in these films it can be observed the

formation of individual crystal very scattered in the substrate with a big area uncovered by the films. Form β and Form γ have similar morphologies what was expected since Form γ is obtained by thermal annealing of Form β, ergo the deposition conditions are the same except for the thermal treatment. Among the four polymorphs Form β and Form γ are the ones that show a better uniformity. Form ε form bigger crystals what creates a bigger uninterrupted pathway for charge transport compared to the other films.

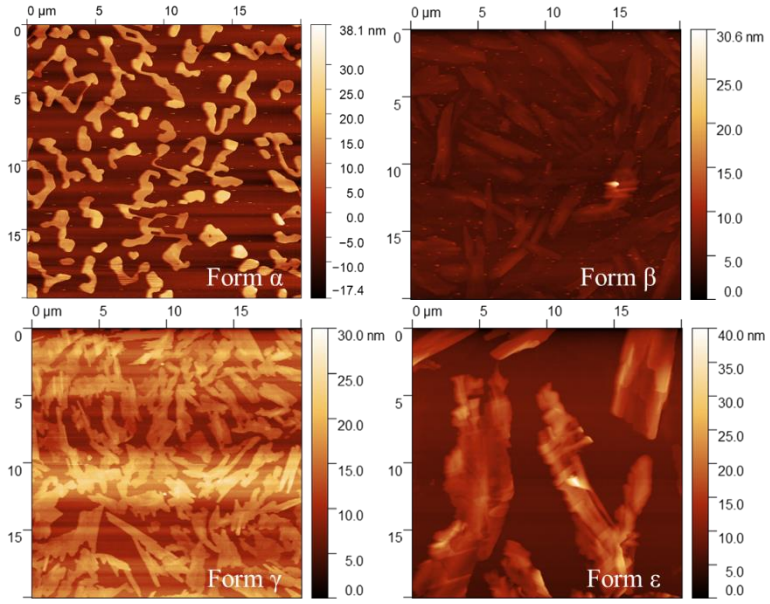

Figure 11 - Film morphology of the four polymorphs of NDI-C6 characterized by AFM.

Conclusions

The polymorphism of NDI-C6 thin films deposited by spin-coating was studied, in particular the influence of different solvents and concentrations. The choice of solvents was based on the difference of boiling point, namely toluene that has a high boiling point and dichloromethane with a much lower boiling point. It was possible to observe Form α, Form β and Form ε in films produced with both solvents, the most common result is a mixture of the three phases, since Form α is the thermodynamic stable phase and Form β is metastable at room temperature. However, it was possible to obtain pure form β in films deposited with a 1mg/ml toluene solution and pure Form ε with a 1mg/ml dichloromethane solution.

In addition, we also studied the thermal stability and the stability over time of the different films. The films deposited with toluene proved to be more stable over a long period of time, while the films produced with dichloromethane converted to more stable forms over time. The stability study allowed us to conclude the stability ranking of the different polymorphs. The ranking can be described as: Form α is stable from RT until 150°C, Form β is metastable from RT up to around 100°C, Form ε is also metastable in the range of RT-150°C and Form γ is stable from 150°C until sublimation of the film around 180°C. At least within the experimental conditions investigated, it was not possible to get Form δ in film. All the pure phases deposited with the optimized conditions

were studied by GIXRD to have a better insight of the crystal forms present in the films. In the case of the new surface induced phase (Form ε) we tried to index the peaks. Because the film is very metastable at the moment of the characterization it was already a mixture of phases making it difficult to get a definite cell and with different approaches, we were able to obtain two slightly different cell parameters.

Using the optimized conditions to get pure phases, we produced OFET devices and studied the morphology of the different polymorphs. The devices characterized do not show a good performance overall, however different polymorphs appear to have different performances. The difference in performance is most likely related to the morphology of the films since it impacts hugely on the charge transport. Considering that none of the phases show films with good uniformity and coverage it is not possible to compare the charge transport and electrical properties of the different polymorphs.

References

(1) Diao, Y.; Lenn, K. M.; Lee, W.; Blood-forsythe, M. A.; Xu, J.; Mao, Y.; Kim, Y.; Reinspach, J. A.; Park, S.; Xue, G.; Clancy, P. Understanding Polymorphism in Organic Semiconductor Thin Films through Nanocon Fi Nement. **2014**. https://doi.org/10.1021/ja507179d.

(2) Bernstein, J. *Polymorphism in Molecular Crystals*; International Union of Crystallography monographs on crystallography; Oxford University Press: OxfordClarendon Press ; New York, 2002.

(3) Zhen, Y.; Dong, H.; Jiang, L.; Hu, W. Tailoring Crystal Polymorphs of Organic Semiconductors towards High-Performance Field-Effect Transistors. *Chinese Chemical Letters* **2016**, *27* (8), 1330–1338. https://doi.org/10.1016/j.cclet.2016.06.023.

(4) Gentili, D.; Gazzano, M.; Melucci, M.; Jones, D.; Cavallini, M. Polymorphism as an Additional Functionality of Materials for Technological Applications at Surfaces and Interfaces. *Chem. Soc. Rev.* **2019**, *48* (9), 2502–2517. https://doi.org/10.1039/C8CS00283E.

(5) Jones, A. O. F.; Geerts, Y. H.; Karpinska, J.; Kennedy, A. R.; Resel, R.; Röthel, C.; Ruzié, C.; Werzer, O.; Sferrazza, M. Substrate-Induced Phase of a [1]Benzothieno[3,2-*b*]Benzothiophene Derivative and Phase Evolution by Aging and Solvent Vapor Annealing. *ACS Appl. Mater. Interfaces* **2015**, *7* (3), 1868–1873. https://doi.org/10.1021/am5075908.

(6) Hao, Y.; Velpula, G.; Kaltenegger, M.; Bodlos, W. R.; Vibert, F.; Mali, K. S.; De Feyter, S.; Resel, R.; Geerts, Y. H.; Van Aert, S.; Beljonne, D.; Lazzaroni, R. From 2D to 3D: Bridging Self-Assembled Monolayers to a Substrate-Induced Polymorph in a Molecular Semiconductor. *Chem. Mater.* **2022**, *34* (5), 2238–2248. https://doi.org/10.1021/acs.chemmater.1c04038.

(7) Jones, A. O. F.; Chattopadhyay, B.; Geerts, Y. H.; Resel, R. Substrate-Induced and Thin-Film Phases : Polymorphism of Organic Materials on Surfaces. *Advanced Functional Materials* **2016**, *26*, 2233–2255. https://doi.org/10.1002/adfm.201503169.

(8) Chung, H.; Diao, Y. Polymorphism as an Emerging Design Strategy for High Performance Organic Electronics. *Journal of Materials Chemistry C* **2016**, *4* (18), 3915–3933. https://doi.org/10.1039/c5tc04390e.

(9) Mattheus, C. C.; Dros, A. B.; Baas, J.; Oostergetel, G. T.; Meetsma, A.; de Boer, J. L.; Palstra, T. T. M. Identification of Polymorphs of Pentacene. *Synthetic Metals* **2003**, *138* (3), 475–481. https://doi.org/10.1016/S0379-6779(02)00467-8.

(10) Bouchoms, I. P. M.; Schoonveld, W. A.; Vrijmoeth, J.; Klapwijk, T. M. Morphology Identification of the Thin Film Phases of Vacuum Evaporated Pentacene on SIO2 Substrates. *Synthetic Metals* **1999**, *104* (3), 175–178. https://doi.org/10.1016/S0379-6779(99)00050-8.

(11) Tommaso Salzillo; Aldo Brillante. A New Approach to Polymorphism in Molecular Crystals: Substrate-Mediated Structures Revealed by Lattice Phonon Dynamics.

(12) *Polymorphism (in the Pharmaceutical Industry)*; Hilfiker, R., Ed.; WILEY-VCH Verlag GmbH & Co. KGaA, 2006.

(13) Bhosale, S. V; Kobaisi, M. Al; Jadhav, R. W.; Morajkar, P. P.; Jones, L. A.; George, S. Naphthalene Diimides : Perspectives and Promise. *Chemical Society Reviews* **2021**, *50*, 9845–9998. https://doi.org/10.1039/d0cs00239a.

(14) Gao, X.; Hu, Y. Development of N-Type Organic Semiconductors for Thin Film Transistors : A Viewpoint of Molecular Design. *Journal of Materials Chemistry C* **2014**, No. 17, 3099–3117. https://doi.org/10.1039/c3tc32046d.

(15) Arash Badami-Behjat; Peter S.Deimel; Francesco Allegretti; Eva Ringel; Kingsuk Mahata; Michael Schmittel; Johannes V.Barth; Wolfgang M. Heckl; Markus Lackinger. Versatile Role of Molecule−Surface Interactions for Monolayer SelfAssembly at Liquid−Solid Interfaces Substrate-Induced. *Chem. Mater.* **2022**, *34*, 8876−8884.

(16) Gentili, D.; Liscio, F.; Demitri, N.; Schäfer, B.; Borgatti, F.; Torelli, P.; Gobaut, B.; Panaccione, G.; Rossi, G.; Degli Esposti, A.; Gazzano, M.; Milita, S.; Bergenti, I.; Ruani, G.; Šalitroš, I.; Ruben, M.; Cavallini, M. Surface Induces Different Crystal Structures in a Room Temperature Switchable Spin Crossover Compound. *Dalton Trans.* **2016**, *45* (1), 134–143. https://doi.org/10.1039/C5DT03712C.

(17) Milita, S.; Liscio, F.; Cowen, L.; Cavallini, M.; Drain, B. A.; Degoussée, T.; Luong, S.; Fenwick, O.; Guagliardi, A.; Schroeder, B. C.; Masciocchi, N. Polymorphism in N,N'-Dialkyl-Naphthalene Diimides. *Journal of Materials Chemistry C* **2020**, *8*, 3097–3112. https://doi.org/10.1039/c9tc06967d.
(18) de Oliveira Martins, I.; Marin, F.; Modena, E.; Maini, L. On the Crystal Forms of NDI-C6: Annealing and Deposition Procedures to Access Elusive Polymorphs. *Faraday Discuss.* **2022**, *235*, 490–507. https://doi.org/10.1039/D1FD00100K.
(19) Lausi, A.; Polentarutti, M.; Onesti, S.; Plaisier, J. R.; Busetto, E.; Bais, G.; Barba, L.; Cassetta, A.; Campi, G.; Lamba, D.; Pifferi, A.; Mande, S. C.; Sarma, D. D.; Sharma, S. M.; Paolucci, G. Status of the Crystallography Beamlines at Elettra. *Eur. Phys. J. Plus* **2015**, *130* (3), 43. https://doi.org/10.1140/epjp/i2015-15043-3.
(20) Schrode, B.; Pachmajer, S.; Dohr, M.; Röthel, C.; Domke, J.; Fritz, T.; Resel, R.; Werzer, O. *GIDVis* : A Comprehensive Software Tool for Geometry-Independent Grazing-Incidence X-Ray Diffraction Data Analysis and Pole-Figure Calculations. *J Appl Crystallogr* **2019**, *52* (3), 683–689. https://doi.org/10.1107/S1600576719004485.
(21) Kainz, M. P.; Legenstein, L.; Holzer, V.; Hofer, S.; Kaltenegger, M.; Resel, R.; Simbrunner, J. *GIDInd* : An Automated Indexing Software for Grazing-Incidence X-Ray Diffraction Data. *J Appl Crystallogr* **2021**, *54* (4), 1256–1267. https://doi.org/10.1107/S1600576721006609.

Chapter 4: Polymorph screening of core-chlorinated naphthalene diimides with different fluoroalkyl side chain lengths

Overview

This chapter starts a new project working with a new series of NDI derivatives provided by BASF SE, which is a partner institute in the UHMob consortium. The selected molecules are core-chlorinated NDIs with fluoroalkyl side chains. These molecules are relevant in the field of organic electronics since the molecular modifications make NDIs more stable in ambient conditions.

This work is focused on the polymorph screening of three NDI derivatives with different fluoroalkyl chain lengths (CF_3-NDI, C_3F_7-NDI, and C_4F_9-NDI). Even though all the systems showed polymorphs and all of them had one solvate form, it was only possible to obtain suitable crystals of the CF_3-NDI different forms. The crystals were characterized by single-crystal XRD, allowing me to learn and understand this technique.

To study the behaviour of the systems at high temperatures I submitted a proposal (ID proposal 2020094721) to ALBA synchrotron for the BL04-MSPD beamline and I was able to collect the data in February 2021.

Supplementary information can be found in Appendix B.

This page intentionally left blank

Polymorph screening of core-chlorinated naphthalene diimides with different fluoroalkyl side chain lengths

Introduction

Organic field-effect transistors (OFETs) are very promising components as they allow to process and fabricate low-cost, large-area, and flexible electronics.[1–4] To develop electronic circuits based on organic semiconductors it is needed complementary logic elements that are more than just single transistors, for example the voltage inverter that is the most basic element. These logic elements require n- and p-type semiconductors and are crucial to achieve low-power dissipation, high-speed and stable circuit performance [5–7] Although much progress has been made in p-type organic semiconductors, the development of organic n-type semiconductors significantly falls behind.[4,7–12] The main reason can be attributed to the difficulty in finding n-type semiconductors with high charge-carrier mobility and air stability, due to the high sensitivity of electrons to ambient oxidants, since ambient oxygen and moisture act as electron traps. [9,12–16]

To improve the air stability of n-type semiconductors two different molecular design strategies can be used. One is by introducing strong electron withdrawing substituents such as -CN, -Cl and -F in the core region, this will lower the LUMO level that not only reduces the electron injection barrier but also provide an effective barrier for water and oxygen penetration, improving the air stability of the devices. The other approach is by adding fluorinated substituents at the imide nitrogen such as fluoroalkyl chains. It is known that fluoroalkyl chains lead to a more densely packed steric barrier to the atmosphere which can prevent oxygen and moisture penetration. [7,14,15,17]

Among the n-type organic semiconductors, naphthalene tetracarboxylic diimides (NDIs) are one of the most promising, due to their easy synthesis from commercially available precursors high electron affinity, large π-orbital overlap in the solid state and tuneable optoelectronic properties. [9,14,18–20] Consequently, NDI derivatives with fluoroalkyl chains at the imide positions and Cl substituents in the core are very promising n-type organic semiconductors. The fluoroalkyl chain substitution at the imide nitrogen positions of the NDI greatly affects the molecular packing and charge carrier mobility [4,9]

The molecular packing of organic small molecule materials is strongly related to charge-carrier transport properties, since close molecular packing with π-orbital overlap between neighbouring molecules improves the charge carrier transport and facilitates high mobility. By slightly changing the packing motif and relative orientation of molecules may cause a big difference in the charge carrier mobility. [7,12,17,21]

For organic molecular materials it is very predominant the crystallization into different polymorphs with various packing arrangements as a consequence of the noncovalent interactions. [22–24] Polymorphism has proven to be an important factor to obtain high-performance organic devices because only specific crystal packing yield to the best mobilities which can be orders of magnitude higher than the mobilities observed in the other polymorphs, moreover it is not easy to

tune the crystallization to obtain the desired form, which can be one not thermodynamically stable. [23,25,26] Thus, the study of polymorphism in organic semiconductors is tremendously important.

Here we study the polymorphic behaviour of three core-chlorinated NDIs with fluoroalkyl chains molecules, all the molecules have the same core and different chain lengths, see molecular structure at Figure 1. The influence of the side chain on the crystal packing was analysed, as well as the thermal properties of each compound. The focus of this work is to analyse the new compound CF_3-NDI (4,5,9,10-tetrachloro-2,7-bis (2,2,2-trifluoroethyl) benzo[lmn] [3,8] phenanthroline-1,3,6,8(2H,7H)-tetraone) and compare it with the well-known C_3F_7-NDI and C_4F_9-NDI. Both C_3F_7-NDI and C_4F_9-NDI have been deeply studied as an active layer of organic field effect transistors and the crystal structures of the most stable phase are solved. [4,12,14] However, no polymorph screenings are reported for these molecules. We report also the serendipitously decomposition of CF_3-NDI that was observed in DMSO and led to the formation of a solid solution of CF_3-NDI and CF_3-NDI-OH.

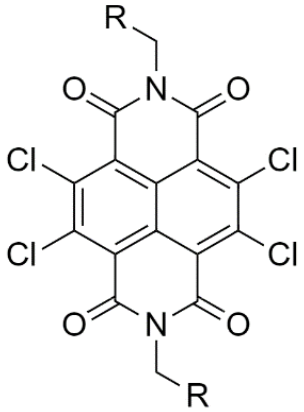

1. $R_1 = CF_3$
2. $R_2 = C_3F_7$
3. $R_3 = C_4F_9$

Figure 1 - Molecular structure of studied NDI derivatives.

Experimental Section

Materials

All the core-chlorinated NDIs with fluoroalkyl chains molecules were provided by BASF SE (Ludwigshafen am Rhein, Germany).

Polymorph screening

The solubility of the three materials was assessed in 14 different solvents at room temperature (see Table S1 in S.I.). Since the molecules exhibit different solubilities, the solvents used for the recrystallization experiments were chosen according to the solubility. Recrystallization by solvent evaporation at room temperature was carried out in the solvents where the solubility was higher than 5 mg/mL, for the remaining solvents slurry experiments at RT were performed.

Slow cooling crystallization was performed using a Technobis – crystallization systems Crystal16 instrument. For CF_3-NDI with a cooling rate of 0.125 °C/min with an acetonitrile (ACN) solution with a concentration of 12.5 mg/ml starting from 75°C to 25°C, and with a dimethyl sulfoxide

(DMSO) solution with a concentration of 33.3 mg/ml and a temperature range 100°C-25°C. In the case of C_3F_7-NDI and C_4F_9-NDI slow cooling was performed using an acetonitrile (ACN) solution with a concentration of 3 mg/ml from 75°C to 25°C and a cooling rate of 0.125 °C/min. All the crystals were left to dry at room conditions before XRD characterization.

X-ray powder diffraction (XRPD)

The powders obtained by recrystallization and the starting material of all the compounds were characterized by XRPD to identify the crystalline phases. The XRD patterns were obtained in Bragg−Brentano geometry, over the 2θ range of 3−40°, with a step size of 0.01° and a speed of 10.0°/min, using a Rigaku MiniFlex 600 diffractometer with Cu Kα (λ = 1.54178 Å) radiation generated from a copper sealed tube with 40 kV and 15 mA.

Variable temperature X-ray powder diffraction (VT-XRPD)

VT-XRPD in transmission mode was performed at ALBA Synchrotron light facility (Barcelona) at BL04-MSPD (Material Science and Powder Diffraction) beamline using glass capillaries with a diameter of 0.5 mm, spinning during the measurement. CF_3-NDI and C_4F_9-NDI powder was filled and compacted in the capillaries. The beamline was equipped with the high-throughput Position Sensitive Detector (PSD) MYTHEN and an FMB Oxford hot air blower to control the temperature. [27] The data were collected with a beam energy of 30 keV (0.41235(1) Å).[28] The characterization of C_4F_9-NDI was executed in a temperature range from 20°C to 275°C in continuous heating with a 5°C/min heating rate. While for CF_3-NDI only room temperature powder pattern was collected.

VT-XRPD of C_3F_7-NDI was performed in reflection mode on a PANalytical X'Pert Pro automated diffractometer with an X'Celerator detector in Bragg–Brentano geometry over the 2θ range of 3−30°, under continuous scan mode with a step size of 0.0167°, using Cu Ka radiation (λ=1.5418 Å) without a monochromator with 40 mA and 40 kV. The diffractometer was equipped with an Anton Paar TTK 450 system for measurements at a controlled temperature.

Single crystal X-ray diffraction (SCXRD)

Data collection of single crystal X-ray diffraction of CF_3-NDI•PXY, obtained from slow evaporation at room temperature of a p-xylene solution, was performed with a Rigaku Oxford Diffraction Xcalibur diffractometer with a Sapphire 3 detector using Mo Kα radiation (λ=0.71073 Å) at room temperature.

A crystal of CF_3-NDI•SS, obtained from DMSO by slow evaporation at room temperature, was mounted on a cryo-loop and used for a low-temperature (160 K) X-ray structure determination. All measurements were made on a Rigaku Oxford Diffraction XtaLAB Synergy diffractometer with a HyPix 6000HE hybrid pixel array detector using Mo Kα radiation (λ=0.71073 Å) from a *PhotonJet* micro-focus X-ray source and an *Oxford Cryosystems Cryostream 800* + cooler. A crystal of CF_3-NDI•Form I, obtained from acetonitrile by slow cooling crystallization, was mounted following the description above but in this case the radiation used was Cu Kα (λ= 1.54184 Å).

The crystal structure was solved using OLEX 2-1.5 software by recurring to SHELXT codes that uses the intrinsic phasing and refined with SHELXL-2019/2 with least square L.S. command.

For visualization and image acquisition of the crystal structures it was used CCDC Mercury 2022.1.0.[29,30]

Differential Scanning Calorimetry (DSC)

The starting materials and the crystals obtained were characterized by differential scanning calorimetry (DSC) using a Mettler-Toledo DSC-1 instrument. The samples were prepared by weighing approximately 1-4 mg of the powder or crystals in aluminium pans (40 μL) and then sealed with an aluminium cover. Before the measurement the pan cover was pierced, and the measurements were performed with a pinhole during two cycles of heating and cooling with a rate of 5°C/min under a dry N_2 atmosphere (flow rate 80 mL/min). Different rates of heating and cooling were tried for better clarity of the thermal events, namely 2°C/min, 5°C/min, 10°C/min and 20°C/min. All the data were analysed using STARe software.

Thermo-Gravimetric Analysis-Evolved Gas analysis (TGA-EGA)

To characterize the solvate forms of the different materials, TGA-EGA was performed on Mettler-Toledo TGA coupled with a Thermo Nicolet iS 10IR FT_IR spectrometer with the scan rate of 10°C/min and analysed using STARe software.

Hot Stage Microscopy (HSM)

The thermal behaviour of the different crystals was studied by hot stage microscopy (HSM), the influence of the temperature was observed on single crystals of C_3F_7-NDI•ACN and C_4F_9-NDI•ACN, obtained by precipitation by gradient temperature in ACN with a cooling rate of -0.125°C/min. The samples were prepared by placing the crystals on a glass slide and covering with a coverslip. The sample is then positioned inside of the sealed heating chamber. The thermal behaviour was analysed using an OLYMPUS BX41 stereomicroscope equipped with a LINKAM LTS350 platinum plate for temperature control and VISICAM analyser. During the experiment time-lapse images were taken using a NIKON DS FI3 high speed camera and analysed using Nikon NIS Elements software and Linksys32.

Attenuated Total Reflection-Fourier Transform Infrared (ATR-FTIR) Spectroscopy

Infrared spectroscopy was performed on all the crystal forms of CF_3-NDI, what includes starting material Form I, solid solution and the solvate phase. The spectra were obtained using a Fourier−transformation infrared spectrometer (Spectrometer: Nicolet iS50 and Detector: DTGS ATR). The spectra were measured over the range of 4000−400 cm^{-1}.

Nuclear magnetic resonance (NMR)

C-NMR and H-NMR were performed on a sample of CF_3-NDI•SS using a Bruker Avance Neo 600 MHz spectrometer, equipped with cryoprobe PRODIGY, cooled with liquid nitrogen.

Hirshfeld surface analysis.

For the Hirshfeld surface analysis of each Form of CF_3-NDI, C_3F_7-NDI and C_4F_9-NDI it was used the software CrystalExplorer 17.5. The analysis was carried out using the crystal structures obtained by single crystal XRD for each Form. The corresponding 2D fingerprint plots were also generated using CrystalExplorer 17.5.

PASCal

PASCal – Principal Axis Strain Calculator is a web-based tool used to determine the principal coefficients of thermal expansion from variable-temperature lattice parameters.[31] The tool requires the temperature and the unit cell parameters values at each temperature as input data. For C_3F_7-NDI we used the data from the VT-XRD obtained using a PANalytical X'Pert Pro, while in the case of C_4F_9-NDI it was used the diffractograms acquired at ALBA. In both cases the cell parameters were refined using Pawley refinement. The tool returns as output the principal axis of thermal expansion and the orientation of the principal axes relative to the axes of the unit cell.

Results and Discussion

Polymorph screening

The solubility assessment for the three molecules demonstrates a decrease in the solubility with the increase of the length of fluoroalkyl side chains related to the low surface free energies of the fluoroalkyl chains and the fact that they are non-polarizable.

In the case of CF_3-NDI, recrystallization experiments by solvent evaporation were performed as described in the experimental section and yield always to the CF_3-NDI•Form I (starting material), except in DMSO and paraxylene. By solvent evaporation in paraxylene we obtained a solvate called CF_3-NDI•PXY which converts into CF_3-NDI•Form I in a couple of hours at room conditions. When CF_3-NDI is recrystallized in DMSO, both by solvent evaporation and by thermal gradient precipitation with a slow cooling profile, big orange block crystals are obtained which only after some efforts were identified as a solid solution of CF_3-NDI and a new molecule obtained by decomposition of CF_3-NDI. The characterization of the new molecule was not straight forward, since it is always obtained along with the presence of starting compound, however by single crystal X-ray diffraction, C-NMR, H-NMR and FTIR (Figure S1, S2 and S3) we were able to identify the new molecule as 4,5,9-trichloro-10-hydroxy-2,7-bis(2,2,2-trifluoroethyl)benzo[lmn][3,8] phenanthroline-1,3,6,8(2H,7H)-tetraone (CF_3-NDI-OH). One of the chlorine atoms has been substituted by the hydroxyl group due to the presence of water in the DMSO. The substitution of the halogen atom was not expected since it happened during a simple recrystallization process, whereas commonly obtained in presence of a reducing agent such as tetrabutylammonium fluoride (TBAF).[32]

It is worth noting that the crystals of the solid solution of CF_3-NDI with CF_3-NDI-OH (hereafter CF_3-NDI•SS), are not isomorphic with CF_3-NDI•Form I so we tried to seed a solution of CF_3-NDI with a crystal of CF_3-NDI•SS to obtain a new polymorph, without any success.

During the polymorph screening we also performed slurry experiment for ten days in isopropanol (2PR), chloroform (CHF), dichloromethane (DCM), ethanol (ETH), water (H2O) and methanol (MET), the solid residue was measured by XRD after one day, three days and ten days. In addition, anti-solvent precipitation and precipitation by gradient temperature were performed in ACN. In all cases, it was obtained CF_3-NDI•Form I.

Analogous polymorph screening was performed for C_3F_7-NDI and C_4F_9-NDI, for both compounds all the slurry and evaporation recrystallization experiments led to the starting material phase Form I, with exception for the slurry experiment in ACN that produced the solvate forms:C_3F_7-NDI•ACN and C_4F_9-NDI•ACN. These solvate forms quickly desolvate into a very poorly crystalline form which is not ascribable to the starting material and was labelled C_3F_7-NDI•Form III and C_4F_9-NDI•Form III, respectively, which convert into the starting structure (Form I) over time. C_3F_7-NDI•ACN and C_4F_9-NDI•ACN crystals were obtained by precipitation by gradient temperature with a cooling rate of -0.125 °C/min, the crystals are stable if they remain in the mother liquor.

Crystal structure

The structures of CF_3-NDI•Form I, CF_3-NDI•SS and CF_3-NDI•PXY were obtained by single crystal X-ray diffraction. Suitable crystals of CF_3-NDI•Form I and CF_3-NDI•SS were obtained by thermal gradient of ACN and DMSO solutions, respectively. CF_3-NDI•PXY crystals were obtained by slow evaporation of a PXY solution. All the crystals exhibit different crystal habits as shown in Figure 2, CF_3-NDI•Form I crystalize in a yellow needle like shape, CF_3-NDI•SS grow as an orange prism while crystals of CF_3-NDI•PXY are dark yellow with a block like morphology.

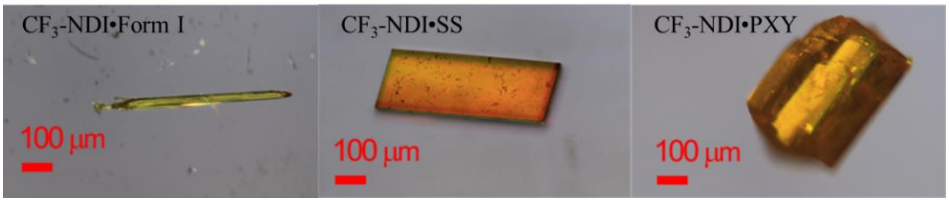

Figure 2 – Crystal habits of CF_3-NDI crystal forms.

Both CF_3-NDI•Form I and CF_3-NDI•PXY are triclinic with space group $P\bar{1}$ with the molecule placed on the inversion centre and half a molecule in the asymmetric unit, in the case of the solvate form the asymmetric unit consists of half molecule of CF_3-NDI and half molecule of paraxylene. While for the solid solution the crystal structure was solved with P1 space group, see in Table 1. The packing of CF_3-NDI•Form I matches with the reported packing of NDIs with longer chains, with slip-stacked molecular packing,[4] but unlike C_3F_7-NDI•Form I and C_4F_9-NDI•Form I, that show a very interdigitated packing, CF_3-NDI•Form I has not interdigitation and it is present a slip plane with 1.574 Å separation between layers, as shown at Figure 3. Despite the presence of the slippery plane the crystals are brittle upon mechanical deformation.

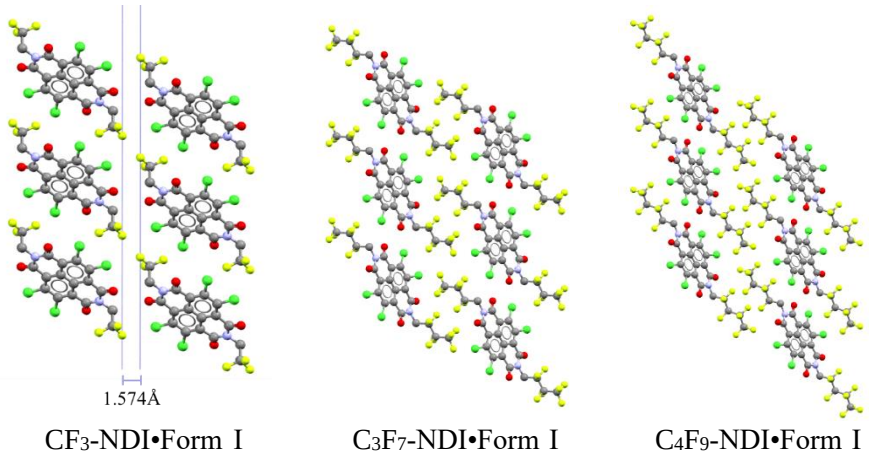

Figure 3 – View of layer separation of CF_3-NDI•Form I and interdigitation of the molecules of C_3F_7-NDI•Form I and C_4F_9-NDI•Form I.

In the case of CF_3-NDI•PXY the solvent molecules are alternated between the slip-stack packs with a 1:1 mixed-stack packing, see Figure 4. Similarly, to CF_3-NDI•Form I, CF_3-NDI•PXY also displays a slip plane but in this case the distance between the layers is much shorter, more specifically 0.641 Å. Curiously, even though CF_3-NDI•PXY shows a tighter packing there are present far lesser short contacts than in CF_3-NDI•Form I.

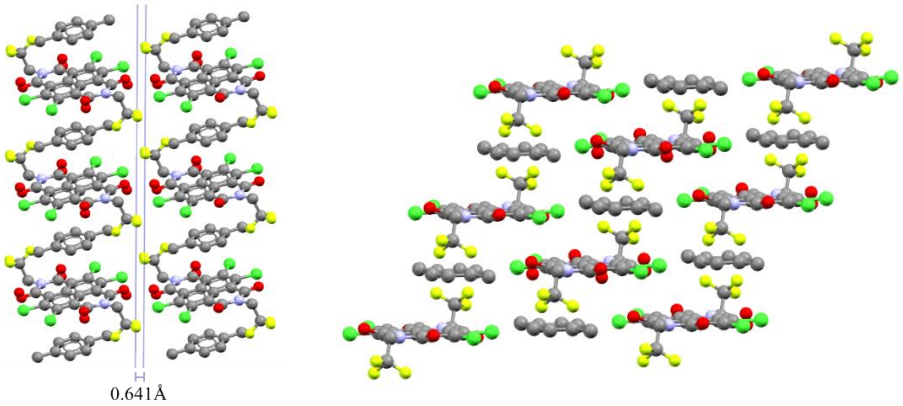

Figure 4 - View of layer separation of CF_3-NDI•PXY and alternated slip-stack of NDI and PXY molecules.

CF_3-NDI•SS crystallizes as triclinic P1, the loss of the inversion centre is due to the substitution of one chlorine atom with a hydroxy group, the diffraction data suggests a substitution of 80%. The hydroxyl group was confirmed also by the C-NMR. Interestingly the crystal structure of CF_3-NDI•SS shows a shorter distance between π-planes (3.277 Å), as displayed in Figure 5, and a more planar core with the lowest torsion angle of all the structures (0.15° and 0.68°), Figure 6, suggesting that if a pure compound is obtained with the same packing parameters, it should give high mobilities in the solid state. Another indicator for expecting high charge carrier mobilities is the high density of the crystal structure (2.069 $g.cm^{-3}$) [4]

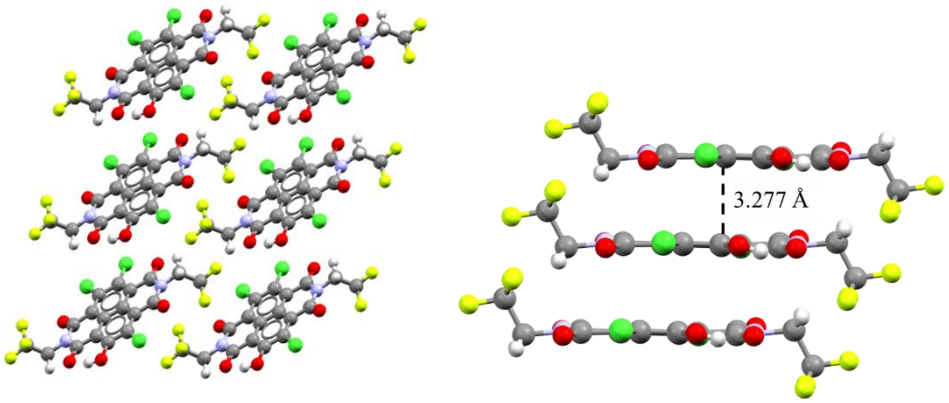

Figure 5 - Crystal packing of CF3-NDI•SS, only the CF_3-NDI-OH are shown but it should be considered that 20% of the solid solution have only Cl in the core.

All the crystal forms of C_3F_7-NDI have the π-conjugated core quite planar, with a torsion angle of 0.69° for CF_3-NDI•Form I, 0.15° and 0.68° for CF_3-NDI•SS that have two different values for the torsion angle since the molecule is not symmetric, and 1.07° for CF_3-NDI•PXY (Figure 6). Regarding the π-π stacking plane distance, both CF_3-NDI•SS and CF_3-NDI•PXY show shorter distances, 3.277 Å and 3.395 Å, what can be associated to the darker orange colour of the crystals. All the packing parameters of the crystal structures can be consulted at Table S2.

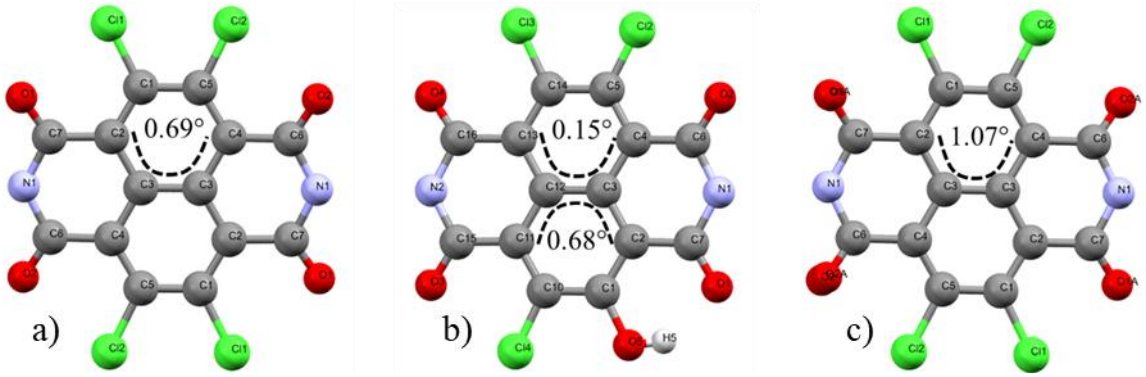

Figure 6 - NDI core with labelled atoms and dihedral angles of all the different crystal forms of C_3F_7-ND: a) CF_3-NDI•Form I, b) CF_3-NDI•SS with only displayed the core of the CF_3-NDI-OH molecule for better clarity and c) CF_3-NDI•PXY.

Table 1 - Crystal structure parameters of CF_3-NDI•Form I, CF_3-NDI•SS, CF_3-NDI•PXY, C_3F_7-NDI•Form I and C_4F_9-NDI•Form I.

	CF_3-NDI•Form I	CF_3-NDI•SS	CF_3-NDI•PXY	C_3F_7-NDI•Form I	C_4F_9-NDI•Form I
CCDC number	This work	This work	This work	761582	761581
Temperature (K)	160.15	160.15	RT	100	100
Formula	$C_{18}H_4Cl_4F_6N_2O_4$	$C_{18}H_{4.8}Cl_{3.2}F_6N_2O_{4.8}$	$C_{18}H_4Cl_4F_6N_2O_4$, C_8H_{10}	$C_{22}H_4Cl_4F_{14}N_2O_4$	$C_{24}H_4Cl_4F_{18}N_2O_4$
Molecular weight	568.03	553.46	674.19	768.07	868.08
Crystal system	Triclinic	Triclinic	Triclinic	Triclinic	Triclinic
Space group	$P\bar{1}$	P1	$P\bar{1}$	$P\bar{1}$	$P\bar{1}$
a (Å)	4.8722(2)	5.83510(10)	7.7798(7)	5.1039(19)	5.5055(7)
b (Å)	8.8027(3)	8.09990(10)	8.1543(9)	10.358(4)	9.8095(11)
c (Å)	11.5608(2)	9.7935(2)	10.6415(7)	12.395(5)	12.7073(15)
α (°)	75.075(2)	97.9620(10)	91.60(7)	111.077(19)	87.786(6)
β (°)	89.777(2)	95.3400(10)	101.96(7)	90.07(2)	81.088(7)
γ (°)	82.792(3)	102.323(2)	90.58(8)	96.67(2)	87.289(7)
V ($Å^3$)	475.103	444.242	660.08	606.645	676.888
Z/Z'	1/0.5	1/1	1/0.5	1/0.5	1/0.5
Density ($g.cm^{-3}$)	1.985	2.069	1.696	2.102	2.13
F(000)	280	274	338		
GOF on F^2	1.156	1.100	1.039	1.076	1.030
R_1 (on F, $I>2\sigma(I)$/ R_{ex})	0.0306	0.0695	0.0477	0.0918	0.0397
WR_2 (F^2 all data) R_{wp}	0.0856	0.2323	0.1049	0.2512	0.1027

Hirshfeld surface analysis

The Hirshfeld surface and their corresponding fingerprint plots, present in Figure 7, were calculated with CrystalExplorer to highlight the different packings within the crystal structure of CF_3-NDI•Form I, C_3F_7-NDI•Form I and C_4F_9-NDI•Form I.[33] d_{norm} mapped on the Hirshfeld Surface shows short intermolecular contacts as red spots, in other words the distance shorter than the van der Waals distance.[34] The Hirshfeld surface plot was mapped over d_{norm} with a range of -0.2382 to 1.396 for CF_3-NDI•Form I, -0.1829 to 1.6553 for C_3F_7-NDI•Form I, and -0.2058 to 1.2578 for C_4F_9-NDI•Form I. In the three structures it is visible red spots related to O--H contacts, the only short intermolecular interaction common for all the three structures, although all the structures have very visible contributions from O--H interactions in the 2D fingerprint plots and in the surface analysis the O and H atoms involved in the interaction is not the same among the three structures, as shown in Figure S4. In the case of CF_3-NDI•Form I this type of interaction occurs both between the molecules involved by π-π stack and the molecules in the same plane with end-to-end interaction. In C_3F_7-NDI•Form I the O--H interaction is between molecules from different planes that form the interdigitated packing. In C_4F_9-NDI•Form I the O--H contacts are

formed between the molecules in the π-π stack. In any way, it must be considered that the Hirshfeld surface analysis is a good indicator of the packing but not necessarily of the interactions potential since the only factor analysed is the distance between atoms. If we look at the interaction's potential by resorting to the mercury tool "UNI intermolecular potentials" it is possible to conclude that the strongest interaction for the three crystal structures is the π-π stack interactions, with a potential significantly higher compared to the other interactions (Figure S5).[35,36]

With the increase of the fluoroalkyl chain it is noticeable at the Hirshfeld surfaces that the interactions between the chains become more prominent (F--F contacts) while the interactions among the core lose importance (C--O contacts). Although the differences follow a trend with the size of the chains, the bigger variation is observed between CF_3-NDI•Form I and the other two structures, CF_3-NDI•Form I and C_4F_9-NDI•Form I, as it can be seen by the 2D fingerprints plots. The most dominant interactions in CF_3-NDI•Form I are Cl –F contacts contributing 28.1% to the Hirshfeld surface and O – H that contributes 11.3%, while both CF_3-NDI•Form I and C_4F_9-NDI•Form I have the same dominant interactions; F –F contacts contributing 29.6% for both structures and Cl—F contacts with a contribution close to 20% in the two structures.

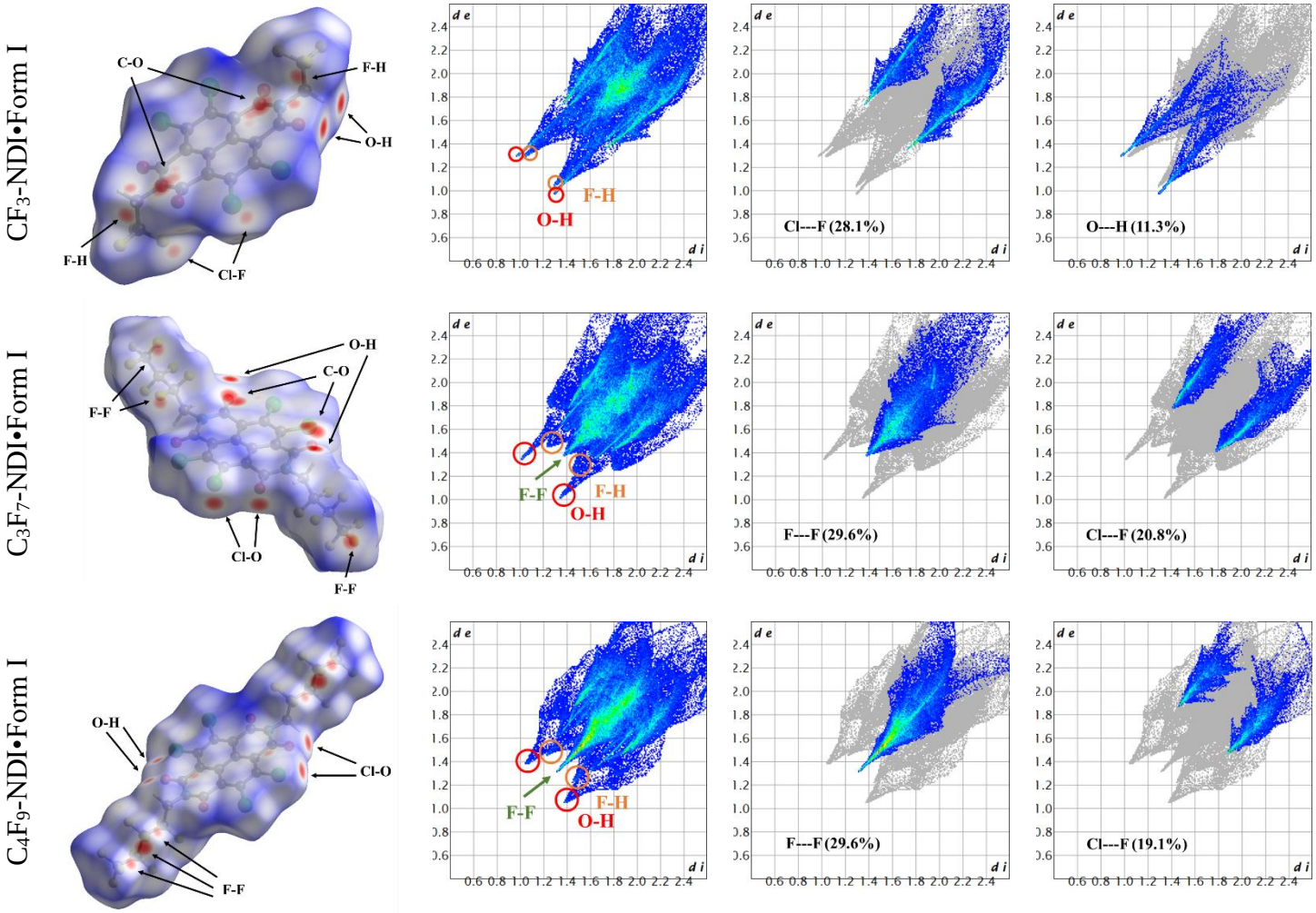

Figure 7 – Hirshfeld surface analysis and corresponding fingerprint plots for Form I (thermodynamic stable form) of each molecule.

Thermal characterization

We performed DSC and TGA on the starting material and on the new forms obtained in the polymorph screening of all three molecules, to characterize their thermal behaviour and depending on the results additional analyses such as VT-XRPD and HSM were also carried out.

For CF_3-NDI•Form I, DSC analysis was performed with two cycles of heating and cooling. No transitions were observed, except for the peaks related to the melting at 322 °C for both heating cycles, and the peak of crystallization during the cooling (Figure S6). Similar behaviour was observed for CF_3-NDI•SS, which shows only the melting peak at 304°C (Figure S7).

TGA and EGA analysis of CF_3-NDI•PXY confirmed that it is a solvate form with stoichiometry of 1:1 with a molecule of PXY for each molecule of CF_3-NDI. The PXY molecules are easily released from the crystal lattice at around 63°C or in a matter of hours at room conditions. The desolvation is easy to identify since the crystal colour changes from the orange crystals of CF_3-NDI•PXY into the light yellow of the CF_3-NDI•Form I (Figure 8). The formation of solvates in organic semiconductors materials is somewhat uncommon and rarely reported, nonetheless there are already some publications that report the formation of solvates. [37–39]

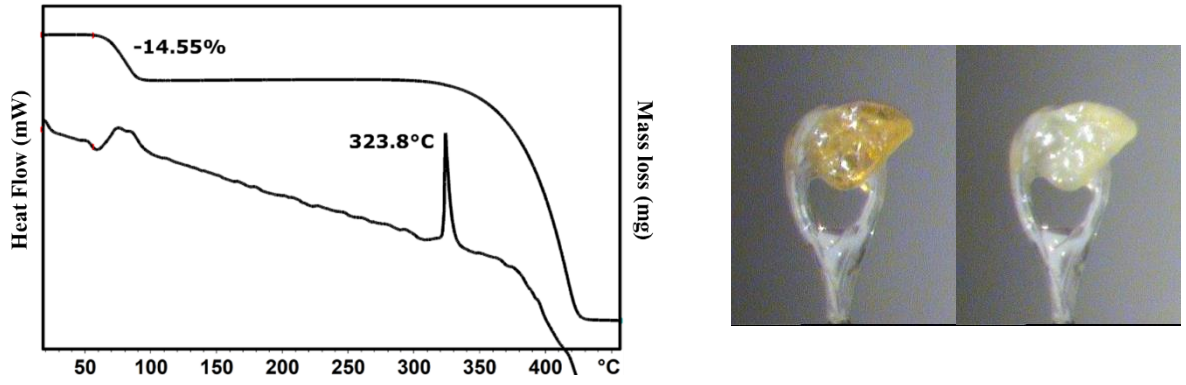

Figure 8 – Loss of solvent of CF_3-NDI•PXY visualized by: a) TGA curve, b) pictures of crystal before and after desolvation it is worth noting that in this case the desolvation led to a crystal suitable for X-ray diffraction, and the cell determination confirmed the presence of CF_3-NDI•form I.

HSM of C_3F_7-NDI•Form I showed a complex behaviour in the heating. The crystals show a high thermal expansion mainly along the long axis of the crystals which can be followed under the microscope, Figure 9, upon cooling the crystals shrink to the starting dimensions. At around 200°C a partial sublimation and recrystallization on the top glass cover is observed. At 302°C a double thermal event is present by simultaneously melting and crystallization of the material into C_3F_7-NDI• Form II, followed by the complete melting at 304°C consistent with the DSC curve. In the cooling the crystallization of C_3F_7-NDI happens at 284°C which we attributed to the Form II since at 251°C a solid-solid transition is observed which is ascribable to the transition C_3F_7-NDI•Form II → C_3F_7-NDI•Form I.

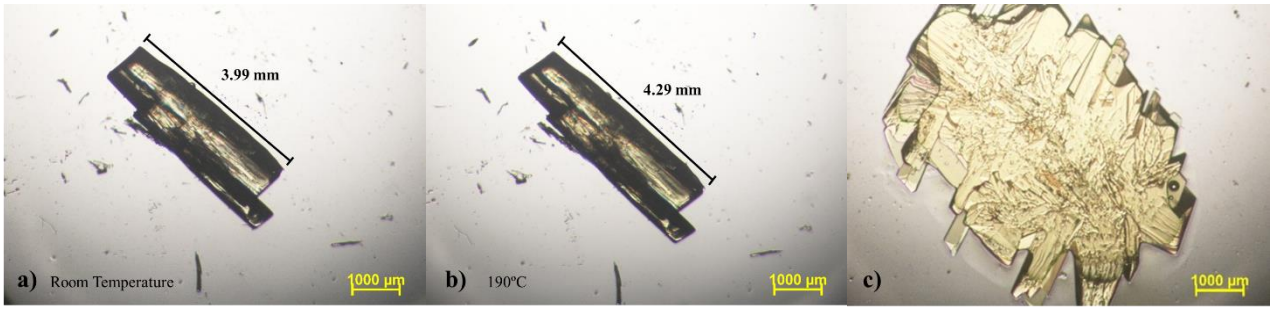

Figure 9 -Pictures from hot stage microscopy of C_3F_7-NDI, a) initial state of C_3F_7-NDI• Form I crystal, b) expanded crystal after thermal expansion and respective dimension, c) melting and crystallization at 302°C.

A cycle of heating, cooling, and heating again was performed on DSC analysis with heating rates of 2°C/min, 5°C/min and 20°C/min. Using the rate of 2°C/min it was possible to identify the first melting followed by recrystallization and second melting as observed in HSM, see Figure 10. Upon cooling, only the recrystallization is observed, which disagrees with the observation in HSM, where it was clear a solid-solid transition. The solid obtained by recrystallization is Form II, in fact by heating it directly melts at 304°C. To confirm the presence of the different forms we characterized by XRPD the material recovered after the DSC analysis of several batches and the crystal phases obtained were not consistent and different results were obtained, namely pure C_3F_7-NDI• Form I and a mixture of C_3F_7-NDI• Form II and C_3F_7-NDI• Form I. These results suggest that C_3F_7-NDI crystallizes into Form II which is metastable and can be easily converted in C_3F_7-NDI• Form I. Only inside the DSC pan the environment allowed to obtain pure Form II at RT, while different cooling rates or even impurities can promote the transition from C_3F_7-NDI• Form II to C_3F_7-NDI• Form I.

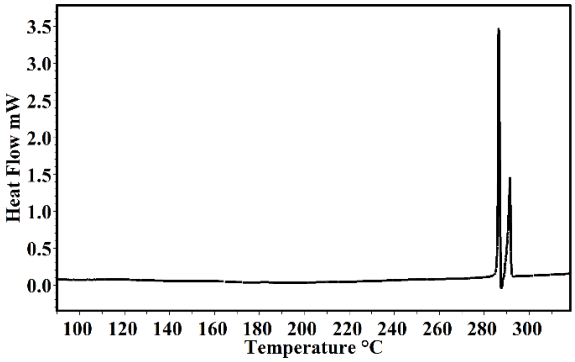

Figure 10 – DSC analysis of C_3F_7-NDI, showing the presence of melting and crystallization followed by a complete melting.

To better understand the thermal expansion of C_3F_7-NDI, VT-XRPD was performed by heating until 200°C and sequent cooling (Figure 11). The XRD patterns during the heating show a variation of the peaks position, related to the thermal expansion also observed by HSM, to confirm the importance of the thermal expansion we used PASCal to quantify the expansion coefficients, and the cell parameters used as input for PASCal are described at Table S3. One of the principal axes shows a big thermal expansion with a positive thermal expansion (PTE) of 320 MK^{-1}, the values of the principal axes' coefficients and their orientation can be consulted at Table S4. This variation is reversible and in the cooling the peaks match to the original XRD pattern of each temperature.

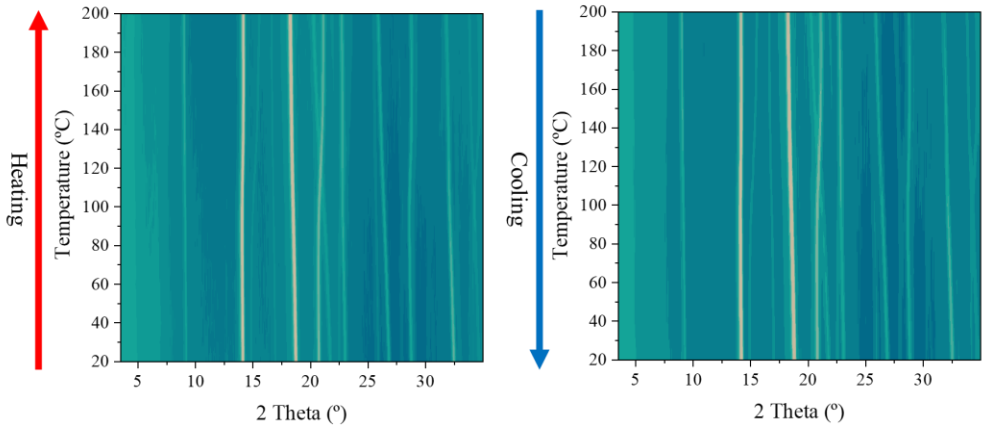

Figure 11 – VT-XRPD of C_3F_7-NDI in heating and cooling, showing the same behaviour for both since the thermal expansion of C_3F_7-NDI is reversible.

In the case of C_4F_9-NDI•Form I, DSC analysis was based on heating, cooling, and a second heating cycle. During the first heating, it is present a solid-solid transition around 276°C ascribed to the transition C_4F_9-NDI•Form I → C_4F_9-NDI•Form II, followed by the melting point at 283°C. This transition is not reversible therefore on cooling it is only observed the crystallization peak into C_4F_9-NDI•Form II which is stable until room temperature. Through the second heating, it is confirmed the presence of C_4F_9-NDI•Form II since no transition is observed and the melting point coincides with the melting point of the first heating C_4F_9-NDI•Form II → liquid. The non-reversible transition C_4F_9-NDI•Form I → C_4F_9-NDI•Form II is confirmed by the data from VT-XRPD with a slight change in the temperature of transition around 258°C (Figure 12).

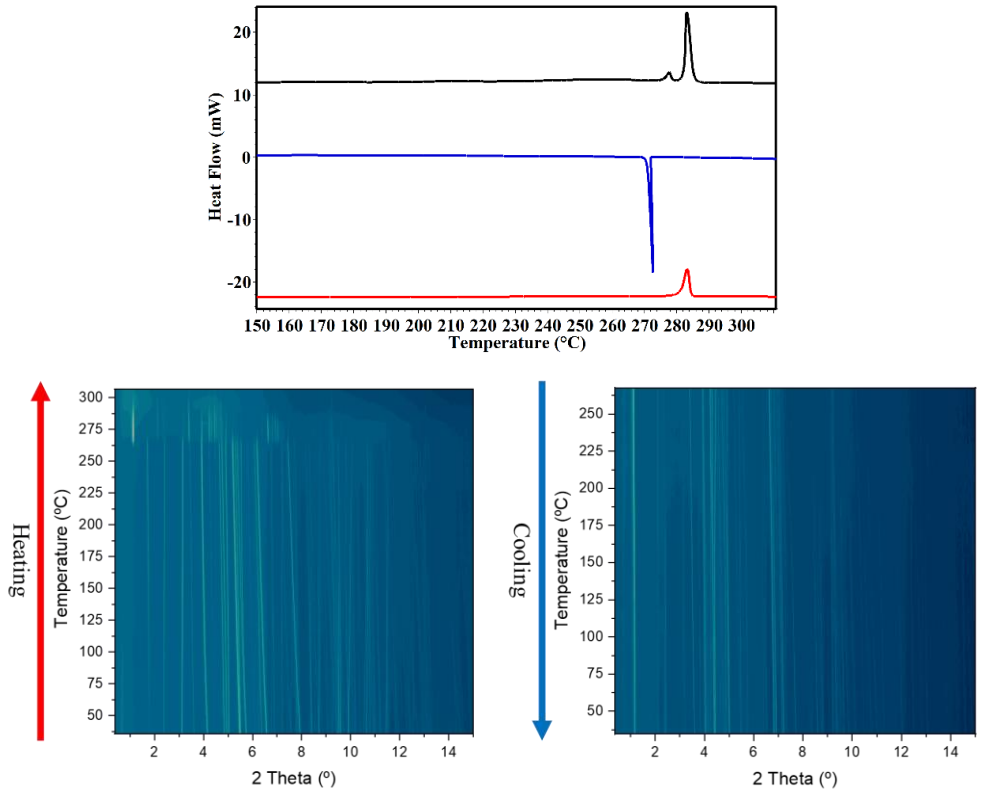

Figure 12 – Confirmation of non-reversible transition C_4F_9-NDI•Form I → C_4F_9-NDI•Form II by DSC and VT-XRPD.

The VT-XRPD reveals that C_4F_9-NDI•Form II has an intense peak at a low angle, normally associated to the length of the molecules as observed for NDI-C6 in our previous work.[24] The presence of a low angle peak, ascribable to a long axis suggests that the C_4F_9-NDI molecules of in Form II pack in a less interdigitated way what causes the increase of the d-spacing. The VT-XRPD also shows a big thermal shift of the peaks position during the heating, before the transition occurs. To have better insight of the thermal expansion mechanism, we used PASCal to analyse C_4F_9-NDI•Form I with the values reported at Table S5 as input. Table 2 summarizes the values of the principal axes' coefficients and their orientation. The principal axes are a set of orthogonal axes along which the material responds in a purely linear manner, and they do not correspond to the unit-cell axes in the case of triclinic systems.[31] Overall, the thermal expansion of C_4F_9-NDI•Form I is very anisotropic and quite significant, with an expansion of 9% of the volume, corresponding to an expansion coefficient of 398 MK^{-1}. This value is much higher than the normally observed in common organic systems, that typically present a volume expansion coefficient of 168 MK^{-1}.[40] C_4F_9-NDI•Form I have negative thermal expansion (NTE) along one principal axis, this behaviour is not unique for this material since it has been reported in a CSD study that approximately 34% of organic crystals have NTE in at least one orthogonal axis.[40] More specifically, in the area of semiconductors some examples have also already been described, such as BHH-BTBT and NDI-C6. [24,41,42] Along the two other axes the expansion is positive, being the highest considered a colossal thermal expansion (X3=287 MK^{-1}).[43]

Table 2 - Values (α_X) of the principal axis of thermal expansion (X1, X2 and X3) and their orientation in regards of the cell axis, a, b and c of C_4F_9-NDI•Form I.

	Principal axis	α_X (MK^{-1})	a	b	c
Form I	X1	-79	0.1583	0.9250	-0.3454
	X2	184	0.9955	-0.0135	0.0939
	X3	287	-0.0673	0.5127	0.8559
	Volume	**398**			

C_4F_9-NDI•ACN crystals are very unstable, so their XRPD pattern was collected in the presence of some mother liquor to avoid the desolvation. In fact, C_4F_9-NDI•ACN rapidly loses the solvent converting into C_4F_9-NDI•Form III. This last Form is characterized by a low crystallinity with peaks not ascribable to Form I nor Form II, as shown in Figure 13.

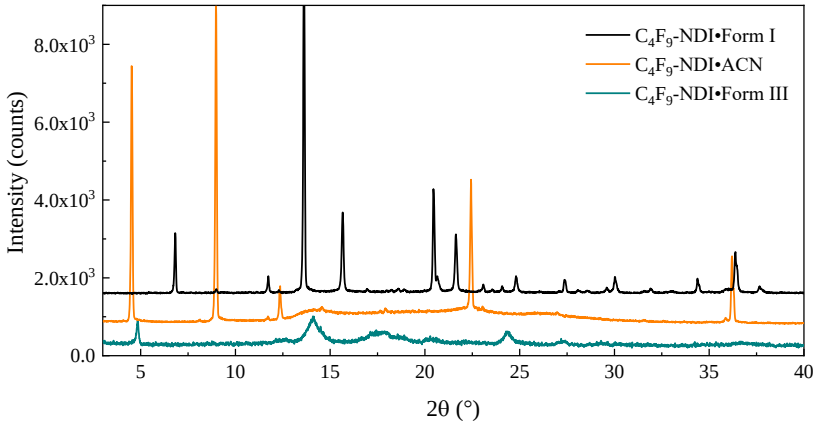

Figure 13 – XRD pattern of C_4F_9-NDI•Form I, C_4F_9-NDI•ACN and C_4F_9-NDI•Form III

The DSC analysis performed on C_4F_9-NDI•Form III, shows an exothermic peak with an onset around 78°C (Figure 14) due to the transition of C_4F_9-NDI•Form III into the more crystalline phase Form II (higher melting point). C_4F_9-NDI•ACN crystals immersed in fomblin were monitored by HSM and it is clearly visible the solvent release at around 78°C, Figure S9. Moreover, changes in the crystal morphology are also observed. Once the loss of solvent happens so fast, to observe the release of solvent of C_4F_9-NDI•ACN crystals by HSM it was necessary to keep the crystals in the mother liquor until the moment of characterization.

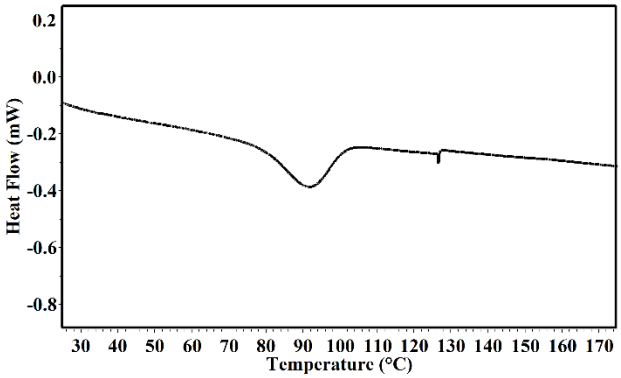

Figure 14 - DSC curve of C_4F_9-NDI•Form III, transition from C_4F_9-NDI•Form III to C_4F_9-NDI•Form I

Conclusions

We studied the polymorphic behaviour of three core-chlorinated NDIs with fluoroalkyl chains compounds CF_3-NDI, C_3F_7-NDI and C_4F_9-NDI which are appealing for the field of organic electronics and in particular C_3F_7-NDI and C_4F_9-NDI are proved to have satisfactory electrical behaviour. In the case of CF_3-NDI, we did not find any evidence of different polymorphs, only one pure crystal phase was observed but we isolated a p-xylene solvate form and serendipitously a solid solution was also discovered. The solid solution is obtained by a partial decomposition of the original compound in DMSO during the recrystallization process and it was not expected. The crystal structure of the three crystal forms of CF_3-NDI were solved and compared with the known crystal structures of C_3F_7-NDI and C_4F_9-NDI. Even though CF_3-NDI•Form I also packs in a $P\bar{1}$

space group with slip-stacked molecular packing like C_3F_7-NDI and C_4F_9-NDI, the molecules are not interdigitated as observed for the compounds with longer chains, in fact CF_3-NDI•Form I have a slip plane of 1.574Å between stacks. CF_3-NDI•SS shows a packing very different from CF_3-NDI•Form I, with a shorter distance between π-planes (3.277 Å) and interdigitated chains, making it a good option for device fabrication in theory, however, to be a good candidate for charge transport it would be ideal to be a pure compound instead of a solid solution. The polymorph screening carried out for C_3F_7-NDI and C_4F_9-NDI gave rise to two new crystal forms for each compound. Both compounds present a ACN solvate very unstable outside the mother liquor which rapidly converts into a poorly crystalline form with main peaks not ascribable to the other polymorphs, namely C_3F_7-NDI•Form III and C_4F_9-NDI•Form III. Furthermore, we also studied in detail the thermal behaviour of the three different compounds. CF_3-NDI shows the simplest thermal behaviour among the three materials, without any temperature dependent transitions. C_3F_7-NDI has a more complex behaviour with a big thermal expansion upon heating that can even be visualized by the change in dimensions of the crystal by HSM, at 302°C simultaneously melting and crystallization of the material into C_3F_7-NDI•Form II is observed followed by the complete melting at 304°C. Even though C_3F_7-NDI• Form II can be observed at RT it is normally as a mixture of C_3F_7-NDI•Form I and C_3F_7-NDI•Form II since C_3F_7-NDI•Form I is the thermodynamically stable form. In the case of C_4F_9-NDI it is present an endothermic solid-solid transition around 276°C ascribed to the transition C_4F_9-NDI•Form I → C_4F_9-NDI•Form II, followed by the melting point at 283°C. Since the transition is not reversible the material ends up as C_4F_9-NDI•Form II at RT. The transition and the thermal behaviour were also followed by VT-XRPD that shows a big thermal shift of the peaks position during the heating before the transition occurs. The thermal expansion was quantified using PASCal and we observed that there is an expansion of 9% of the volume, corresponding to an expansion coefficient of 398 MK^{-1}. This value is much higher than the normally observed in common organic systems.

References

(1) Gao, X.; Zhao, Z. High Mobility Organic Semiconductors for Field-Effect Transistors. *Sci. China Chem* **2015**, *58* (6), 947–968. https://doi.org/10.1007/s11426-015-5399-5.

(2) Zhao, C.; Li, A.; Chen, X.; Ali, M. U.; Meng, H. Hysteresis Effect in Organic Thin Film Transistors Based on Naphthalene Tetracarboxylic Diimide Derivatives. *Applied Physics Letters* **2021**, *118* (193302). https://doi.org/10.1063/5.0045183.

(3) Fukuda, K.; Takeda, Y.; Mizukami, M.; Kumaki, D.; Tokito, S. Fully Solution-Processed Flexible Organic Thin Film Transistor Arrays with High. **2014**, No. 20 V, 4–11. https://doi.org/10.1038/srep03947.

(4) Joon Hak Oh. High-Performance Air-Stable N-Type Organic Transistors Based on Core-Chlorinated Naphthalene Tetracarboxylic Diimides. *Adv. Funct. Mater.*

(5) Zaumseil, J.; Sirringhaus, H. Electron and Ambipolar Transport in Organic Field-Effect Transistors. *Chem. Rev.* **2007**, *107* (4), 1296–1323. https://doi.org/10.1021/cr0501543.

(6) Katz, H. E.; Lovinger, A. J.; Johnson, J.; Kloc, C.; Siegrist, T.; Li, W.; Lin, Y.-Y.; Dodabalapur, A. A Soluble and Air-Stable Organic Semiconductor with High Electron Mobility. *Nature* **2000**, *404* (6777), 478–481. https://doi.org/10.1038/35006603.

(7) He, T.; Stolte, M.; Würthner, F. Air-Stable n-Channel Organic Single Crystal Field-Effect Transistors Based on Microribbons of Core-Chlorinated Naphthalene Diimide. *Adv. Mater.* **2013**, *25* (48), 6951–6955. https://doi.org/10.1002/adma.201303392.

(8) Kim, R.; Amegadze, P. S. K.; Kang, I.; Yun, H.; Noh, Y.; Kwon, S.; Kim, Y. High-Mobility Air-Stable Naphthalene Diimide-Based Copolymer Containing Extended π -Conjugation for n-Channel Organic Field Effect Transistors. **2013**, 1–9. https://doi.org/10.1002/adfm.201301197.

(9) Gogoi, G.; Bhattacharya, L.; Sahoo, S. R.; Sahu, S.; Sarma, N. S.; Sharma, S. Enhancement of Air-Stability, π-Stacking Ability, and Charge Transport Properties of Fluoroalkyl Side Chain Engineered n-Type Naphthalene Tetracarboxylic Diimide Compounds. *RSC Adv.* **2021**, *11* (1), 57–70. https://doi.org/10.1039/D0RA08345C.

(10) Kang, M. J.; Doi, I.; Mori, H.; Miyazaki, E.; Takimiya, K.; Ikeda, M.; Kuwabara, H. Alkylated Dinaphtho[2,3-b:2′,3′-f]Thieno[3,2-b]Thiophenes (Cn-DNTTs): Organic Semiconductors for High-Performance Thin-Film Transistors. *Adv. Mater.* **2011**, *23* (10), 1222–1225. https://doi.org/10.1002/adma.201001283.

(11) Zhan, X.; Facchetti, A.; Barlow, S.; Marks, T. J.; Ratner, M. A.; Wasielewski, M. R.; Marder, S. R. Rylene and Related Diimides for Organic Electronics. *Adv. Mater.* **2011**, *23* (2), 268–284. https://doi.org/10.1002/adma.201001402.

(12) Geng, Y.; Wu, S.-X.; Li, H.-B.; Tang, X.-D.; Wu, Y.; Su, Z.-M.; Liao, Y. A Theoretical Discussion on the Relationships among Molecular Packings, Intermolecular Interactions, and Electron Transport Properties for Naphthalene Tetracarboxylic Diimide Derivatives. *J. Mater. Chem.* **2011**, *21* (39), 15558. https://doi.org/10.1039/c1jm12483h.

(13) Stolte, M.; Suraru, S.-L.; Würthner, F.; Oh, J. H.; Bao, Z.; Brill, J.; Könemann, M.; Qu, J.; Zschieschang, U.; Klauck, H. Organic N-Channel Thin Film Transistors Based on Dichlorinated Naphthalene Diimides; Bao, Z., McCulloch, I., Eds.; San Diego, California, 2010; p 777804. https://doi.org/10.1117/12.859829.

(14) Wen-Ya Lee; Joon Hak Oh; Sabin-Lucian Suraru; Wen-Chang Chen; Frank Würthner; Zhenan Bao. High-Mobility Air-Stable Solution-Shear-Processed N-Channel Organic Transistors Based on Core-Chlorinated Naphthalene Diimides. *Adv. Funct. Mater.* **2011**, *21*, 4173–4181.

(15) Chen, X.; Zhang, D.; He, Y.; Ali, M. U.; Wu, Y.; Zhao, C.; Wu, P.; Yan, C.; Wudl, F.; Meng, H. Fluoro-Alkyl Substituted Isothianaphthene Bisimides as Stable n-Type Semiconductors. *Mater. Chem. Front.* **2020**, *4* (12), 3578–3584. https://doi.org/10.1039/D0QM00137F.

(16) Jones, B. A.; Facchetti, A.; Wasielewski, M. R.; Marks, T. J. Tuning Orbital Energetics in Arylene Diimide Semiconductors . Materials Design for Ambient Stability of n-Type Charge Transport. **2007**, *56* (12), 15259–15278. https://doi.org/10.1021/ja075242e.

(17) Ze-Fan Yao; Jie-Yu Wang; Jian Pei. Control of Π−π Stacking via Crystal Engineering in Organic. *Cryst. Growth Des* **2018**, *18*, 7−15.
(18) Canola, S.; Negri, F. Anisotropy of the N-Type Charge Transport and Thermal Effects in Crystals of a Fluoro-Alkylated Naphthalene Diimide: A Computational Investigation. *Phys. Chem. Chem. Phys.* **2014**, *16* (39), 21550–21558. https://doi.org/10.1039/C4CP03231D.
(19) Bhosale, S. V.; Kobaisi, M. A.; Jadhav, R. W.; Morajkar, P. P.; Jones, L. A.; George, S. Naphthalene Diimides : Perspectives and Promise. *Chemical Society Reviews* **2021**, *50*, 9845–9998. https://doi.org/10.1039/d0cs00239a.
(20) Gao, X.; Hu, Y. Development of N-Type Organic Semiconductors for Thin Film Transistors : A Viewpoint of Molecular Design. *Journal of Materials Chemistry C* **2014**, No. 17, 3099–3117. https://doi.org/10.1039/c3tc32046d.
(21) Lovrinčić, R.; Trollmann, J.; Pölking, C.; Schöneboom, J.; Lennartz, C.; Pucci, A. Orientation of Nonplanar Molecules in Polycrystalline Layers from Infrared Spectra: Core-Chlorinated Naphthalene Tetracarboxylic Diimides. *J. Phys. Chem. C* **2012**, *116* (9), 5757–5763. https://doi.org/10.1021/jp211077t.
(22) Zhen, Y.; Dong, H.; Jiang, L.; Hu, W. Tailoring Crystal Polymorphs of Organic Semiconductors towards High-Performance Field-Effect Transistors. *Chinese Chemical Letters* **2016**, *27* (8), 1330–1338. https://doi.org/10.1016/j.cclet.2016.06.023.
(23) Purdum, G. E.; Telesz, N. G.; Jarolimek, K.; Ryno, S. M.; Gessner, T.; Davy, N. C.; Petty, A. J.; Zhen, Y.; Shu, Y.; Facchetti, A.; Collis, G. E.; Hu, W.; Wu, C.; Anthony, J. E.; Weitz, R. T.; Risko, C.; Loo, Y.-L. Presence of Short Intermolecular Contacts Screens for Kinetic Stability in Packing Polymorphs. *J. Am. Chem. Soc.* **2018**, *140* (24), 7519–7525. https://doi.org/10.1021/jacs.8b01421.
(24) de Oliveira Martins, I.; Marin, F.; Modena, E.; Maini, L. On the Crystal Forms of NDI-C6: Annealing and Deposition Procedures to Access Elusive Polymorphs. *Faraday Discuss.* **2022**, *235*, 490–507. https://doi.org/10.1039/D1FD00100K.
(25) Riera-Galindo, S.; Tamayo, A.; Mas-Torrent, M. Role of Polymorphism and Thin-Film Morphology in Organic Semiconductors Processed by Solution Shearing. *ACS Omega* **2018**, No. 3, 2329–2339. https://doi.org/10.1021/acsomega.8b00043.
(26) Chung, H.; Diao, Y. Polymorphism as an Emerging Design Strategy for High Performance Organic Electronics. *Journal of Materials Chemistry C* **2016**, *4* (18), 3915–3933. https://doi.org/10.1039/c5tc04390e.
(27) Fauth, F.; Peral, I.; Popescu, C.; Knapp, M. The New Material Science Powder Diffraction Beamline at ALBA Synchrotron. *Powder Diffr.* **2013**, *28* (S2), S360–S370. https://doi.org/10.1017/S0885715613000900.
(28) Fauth, F.; Boer, R.; Gil-Ortiz, F.; Popescu, C.; Vallcorba, O.; Peral, I.; Fullà, D.; Benach, J.; Juanhuix, J. The Crystallography Stations at the Alba Synchrotron. *Eur. Phys. J. Plus* **2015**, *130* (8), 160. https://doi.org/10.1140/epjp/i2015-15160-y.
(29) Macrae, C. F.; Bruno, I. J.; Chisholm, J. A.; Edgington, P. R.; McCabe, P.; Pidcock, E.; Rodriguez-Monge, L.; Taylor, R.; van de Streek, J.; Wood, P. A. It Mercury CSD 2.0 – New Features for the Visualization and Investigation of Crystal Structures. *Journal of Applied Crystallography* **2008**, *41* (2), 466–470. https://doi.org/10.1107/S0021889807067908.
(30) Macrae, C. F.; Sovago, I.; Cottrell, S. J.; Galek, P. T. A.; McCabe, P.; Pidcock, E.; Platings, M.; Shields, G. P.; Stevens, J. S.; Towler, M.; Wood, P. A. It Mercury 4.0: From Visualization to Analysis, Design and Prediction. *Journal of Applied Crystallography* **2020**, *53* (1), 226–235. https://doi.org/10.1107/S1600576719014092.
(31) Cliffe, M. J.; Goodwin, A. L. PASCal: A Principal Axis Strain Calculator for Thermal Expansion and Compressibility Determination. *Journal of Applied Crystallography* **2012**, *45* (6), 1321–1329. https://doi.org/10.1107/S0021889812043026.
(32) Tam, T. L. D.; Xu, J. W. The Role of Fluoride in Anion–π Interaction with Naphthalene Diimide. *Chem. Commun.* **2019**, *55* (44), 6225–6228. https://doi.org/10.1039/C9CC01795J.

(33) Spackman, P. R.; Turner, M. J.; McKinnon, J. J.; Wolff, S. K.; Grimwood, D. J.; Jayatilaka, D.; Spackman, M. A. *CrystalExplorer* : A Program for Hirshfeld Surface Analysis, Visualization and Quantitative Analysis of Molecular Crystals. *J Appl Crystallogr* **2021**, *54* (3), 1006–1011. https://doi.org/10.1107/S1600576721002910.
(34) Spackman, M. A.; Jayatilaka, D. Hirshfeld Surface Analysis. *CrystEngComm* **2009**, *11* (1), 19–32. https://doi.org/10.1039/B818330A.
(35) Gavezzotti, A. Are Crystal Structures Predictable? *Acc. Chem. Res.* **1994**, *27*, 309—314.
(36) Gavezzotti, A.; Filippini, G. Geometry of the Intermolecular X-H.Cntdot..Cntdot..Cntdot.Y (X, Y = N, O) Hydrogen Bond and the Calibration of Empirical Hydrogen-Bond Potentials. *J. Phys. Chem.* **1994**, *98* (18), 4831–4837. https://doi.org/10.1021/j100069a010.
(37) Pandey, P.; Demitri, N.; Gigli, L.; James, A. M.; Devaux, F.; Geerts, Y. H.; Modena, E.; Maini, L. Discovering Crystal Forms of the Novel Molecular Semiconductor OEG-BTBT. *Crystal Growth & Design* **2022**, *22* (3), 1680–1690. https://doi.org/10.1021/acs.cgd.1c01203.
(38) Courté, M.; Ye, J.; Jiang, H.; Ganguly, R.; Tang, S.; Kloc, C.; Fichou, D. Tuning the π–π Overlap and Charge Transport in Single Crystals of an Organic Semiconductor *via* Solvation and Polymorphism. *Phys. Chem. Chem. Phys.* **2020**, *22* (35), 19855–19863. https://doi.org/10.1039/D0CP03109G.
(39) Marin, F.; Tombolesi, S.; Salzillo, T.; Yaffe, O.; Maini, L. Thorough Investigation on the High-Temperature Polymorphism of Dipentyl-Perylenediimide: Thermal Expansion *vs.* Polymorphic Transition. *J. Mater. Chem. C* **2022**, *10* (20), 8089–8100. https://doi.org/10.1039/D1TC06132A.
(40) van der Lee, A.; Dumitrescu, D. G. Thermal Expansion Properties of Organic Crystals: A CSD Study. *Chem. Sci.* **2021**, *12* (24), 8537–8547. https://doi.org/10.1039/D1SC01076J.
(41) Lee, A. V. D.; Roche, G. H.; Wantz, G.; Moreau, J. J. E.; Dautel, O. J.; Filhol, J. S. Experimental and Theoretical Evidence of a Supercritical-like Transition in an Organic Semiconductor Presenting Colossal Uniaxial Negative Thermal Expansion. *Chemical Science* **2018**, *9* (16), 3948–3956. https://doi.org/10.1039/c8sc00159f.
(42) Liu, Z.; Gao, Q.; Chen, J.; Deng, J.; Lin, K.; Xing, X. Negative Thermal Expansion in Molecular Materials. *ChemComm* **2018**, *54*, 5164–5176. https://doi.org/10.1039/c8cc01153b.
(43) Goodwin, A. L.; Calleja, M.; Conterio, M. J.; Dove, M. T.; Evans, J. S. O.; Keen, D. A.; Peters, L.; Tucker, M. G. Colossal Positive and Negative Thermal Expansion in the Framework Material Ag3[Co(CN)6]. *Science* **2008**, *319* (5864), 794–797. https://doi.org/10.1126/science.1151442.

This page intentionally left blank

Chapter 5: Synthesis and characterization of charge transfer complexes based on NDI derivatives and BTBT derivatives

Overview

In the last part of my thesis project, I worked on the synthesis and characterization of novel organic D-A co-crystals based on NDI derivatives as acceptors and BTBT and ditBu-BTBT as donors to obtain Charge Transfer (CT) complexes. The NDI derivatives chosen for this project were the same as those studied in the previous chapter, which have four chlorine in the core and $C_3F_7Cl_2$-NDI (4,9-dichloro-2,7-bis(2,2,3,3,4,4,4-heptafluorobutyl)benzo[lmn][3,8]phenanthroline-1,3,6,8(2H,7H)-tetraone) that is known as a semiconductor with good performance in devices, which has two chlorines in the core, to study how the core substitutions affect the formation of D-A co-crystals. By recrystallization I obtained six D-A co-crystals that were solved and analyzed thoroughly. Although the crystal looked suitable for SCXRD they are highly disordered structures mainly in the BTBT molecules and it was challenging to obtain publishable structures. To investigate the charge transfer interaction in the new compounds, ATR-FTIR spectroscopy was carried out in collaboration with Dr Tommaso Salzillo, giving me the chance to expand my knowledge of this technique.

This project started close to the end of my PhD and I did not have enough time to carry out an exhaustive characterization of the materials. I focused on the darkest co-crystals which are the most promising for CT complex. Moreover, I had only 100 mg of each NDI compounds limiting the number of experiments of recrystallization and characterization.

This page intentionally left blank

Synthesis and characterization of charge transfer complexes based on NDI derivatives and BTBT derivatives

Introduction

Organic semiconductors (OSCs) have drawn a great amount of attention since they can be employed in flexible substrates through low-cost and solution-based processing and are easily tailored through possible chemical modifications for specific applications in optoelectronic devices such as OFETs, OPVs and OLEDs. [1–3] Although a lot of studies have been done on crystals based on monomolecular compounds, both with p-type materials such as pentacene or rubrene and n-type materials like PDIs and NDIs, more recently it has grown an increasing interest in binary charge-transfer (CT) organic crystals. [4,5]

Organic charge-transfer complexes are two-component systems with a specific stoichiometry, that can have different degrees of charge transfer (ρ), one component is an electron donor (D) and the other is an electron acceptor (A), which normally are unipolar semiconductors in their pristine form.[2,6] The D-A cocrystal structures may have unique optical or electrical properties, such as high conductivity and ambipolar charge carrier transport. Much like n-type semiconductors, air-stable ambipolar materials are also very uncommon, therefore it is extremely important to study and develop new air-stable ambipolar and n-type materials since they are essential unit blocks in organic electronics.

However, it is still challenging the design and growth of D-A cocrystals mainly for molecules with low solubility since they tend to self-aggregate separately into donor or acceptor assemblies alone instead of D-A cocrystals. [1,4,7–10] The supramolecular arrangement of D-A organic solid co-crystals is a critical parameter for device performance because it affects the degree of charge transfer (ρ), which depends on the intermolecular interactions that are normally van der Waals, π-π interactions and halogen/hydrogen bonding. [3,11–13]

The supramolecular arrangement determines the bandwidth of the highest occupied molecular orbital (HOMO) of D and the lowest unoccupied molecular orbital (LUMO) of A, hence by modifying the supramolecular arrangement, it is possible to tune the bandgap, defined as approximately the energy difference between the LUMO of A and the HOMO of D, and consequently the charge carrier transport.[11,13,14]

Typically D-A organic cocrystals can be divided into two main families, one which shows segregated stacking (…-D-D-D-… and …-A-A-A-…), where the molecules form separated D and A stacks and normally display high electrical conductivity, and one which shows a mixed stack (…-D-A-D-A-…), where the D and A molecules pack in an alternate way along the stack and usually are insulators or semiconductors. [4,6,11,15]

Like single-component systems, multi-component CT crystals can also exhibit polymorphism. Furthermore, the range of crystal forms of CT systems can be significantly extended since the same D and A can crystalize with different stoichiometries of the two species, this phenomenon is

called stoichiomorphism. That is why it is vital to study the crystal packing of CT complexes and to understand when specific π-conjugated systems can generate well-defined π-stacks. [4,5,14,16–18]

Napthalene diimide (NDI) derivatives due to their relatively low reduction potentials are a well-known π-conjugated electron acceptor, usually used as an n-type semiconductor, which can be used as a building block of charge transfer complexes. In fact, there are several reports of CT complexes using NDI as acceptor component. [8,19,20]

In this work we study the formation of CT complexes composed of NDI derivatives as acceptor and BTBT and ditBu-BTBT as donors, the chemical diagram of all the components used in the CT complexes are shown in Figure 1. The main focus is to understand how different substitutions and different chain lengths of the NDI molecules influence the formation of CT complexes. The crystal structures of six different D-A complexes were studied and analyzed. Moreover, the thermal behavior and a preliminary analysis of the optical gap of the two D-A co-crystals obtained using compound 2 ($C_3F_7Cl_2$-NDI) was investigated.

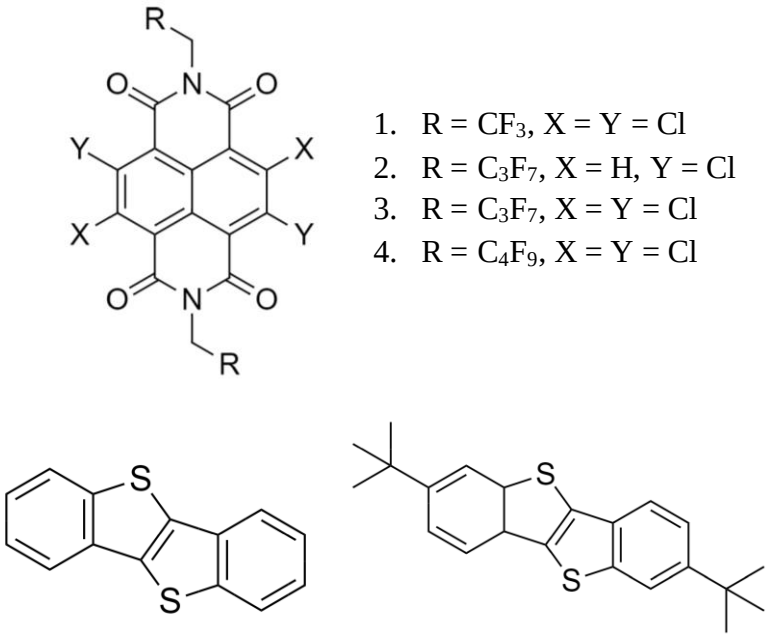

Figure 1 - Chemical diagram of the acceptors (NDI derivatives) and donors (BTBT derivatives) used for the co-crystallization of the CT complexes.

Experimental Section

Materials

All the core-chlorinated NDIs with fluoroalkyl chains compounds were provided by BASF SE (Ludwigshafen am Rhein, Germany) while the BTBT compounds were provided by Université Libre de Bruxelles (ULB). The available amount of each compound was limited and in the case of the NDIs less than 100 mg of each compound was available.

Co-crystallization of CT complexes

The CT complexes were all obtained by slurry at room temperature in toluene, and different D-A ratios were tested, in all cases the amount used was approx. 2-3 mg of powder and 200-250 µL of solvent. After filtration, the solid material was left to dry under ambient conditions.

The BTBT:$C_3F_7Cl_2$-NDI complex was obtained by mixing in five separate batches BTBT and $C_3F_7Cl_2$-NDI with different molar ratios in a toluene medium (1.5:1, 1.75:1, 2:1, 2.3:1 and 2.8:1). A bright red color saturated solution was produced and left to stir constantly for 1-2h at room temperature, in all cases the solvated CT complex BTBT:$C_3F_7Cl_2$-NDI•TOL was obtained.

ditBu-BTBT and $C_3F_7Cl_2$-NDI were mixed in 1:1, 1.8:1, 2:1 and 1:1.1 mol/mol ratios in a toluene medium. A light brownish yellow solution is obtained and stirred for 48h at room temperature causing the change of the solution's color to black, see Figure 2. In the case of 1:1.1 ratio, the only ratio with more $C_3F_7Cl_2$-NDI than ditBu-BTBT, the CT complex was not obtained even after 96h of slurry, the solution did not change color and remained light brownish yellow.

BTBT and $C_3F_7Cl_4$-NDI were mixed in 1.7:1, 2.5:1, 2.8:1 and 3.2:1 mol/mol ratios and stirred in a toluene solution for 1-2h at room temperature. The solution turned dark red and for all the experiments we obtained the same CT complex BTBT:$C_3F_7Cl_4$-NDI.

The solid ditBu-BTBT:$C_3F_7Cl_4$-NDI complex was arranged by mixing ditBu-BTBT and $C_3F_7Cl_4$-NDI with 1.2:1, 1.8:1, 2:1 and 2.2:1 mol/mol ratios and were slurried in a toluene medium for 1-2h. The solution obtained was dark green.

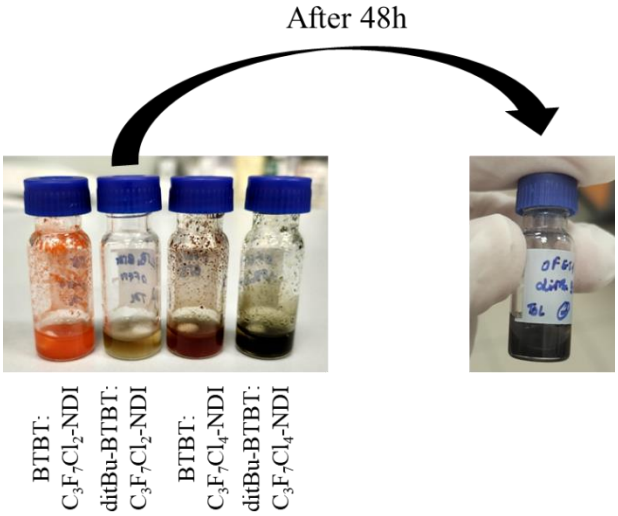

Figure 2 – Solid product of the DA complexes obtained by slurry after 2h, and 48h for ditBu-BTBT:$C_3F_7Cl_2$-NDI after changing visual aspect.

Single crystals isolation of CT complexes

Single crystals of six different CT complexes were crystallized, namely BTBT:$C_3F_7Cl_2$-NDI•TOL, ditBu-BTBT:$C_3F_7Cl_2$-NDI, BTBT:$C_3F_7Cl_4$-NDI, ditBu-BTBT:$C_3F_7Cl_4$-NDI, BTBT:CF_3Cl_4-NDI and BTBT:$C_4F_9Cl_4$-NDI. BTBT:$C_3F_7Cl_2$-NDI•TOL crystals were obtained by slow evaporation at

room temperature of a toluene solution. The solution was prepared by adding toluene to a 1:1 w/w mixture of $C_3F_7Cl_2$-NDI and BTBT and then heated at 60°C to facilitate the dissolution. In the case of ditBu-BTBT:$C_3F_7Cl_2$-NDI and ditBu-BTBT:$C_3F_7Cl_4$-NDI, the crystals were achieved by slow evaporation at room temperature of acetone solutions. In both cases the compounds were slurried in 200 μL of acetone in a 1:1 stoichiometric ratio for 5 min followed by the addition of 800 μL of acetone and left to evaporation. The crystals of BTBT:$C_3F_7Cl_4$-NDI were obtained by slow cooling crystallization from a toluene solution with a 1:1 weight ratio using a Technobis – crystallization systems Crystal16 instrument with a cooling rate of 0.125 °C/min. From this experiment it was observed two different crystal morphologies: needles and plates, possibly different polymorphs, and crystals of BTBT from the excess used. BTBT:CF_3Cl_4-NDI and BTBT:$C_4F_9Cl_4$-NDI crystals were crystallized from a mixture of solvents, by mixing a solution of NDI in acetone and a solution of BTBT in THF. The final solutions were left to evaporate slowly at room temperature.

X-ray powder diffraction (XRPD)

To identify the crystalline forms of the powder and crystals obtained by co-crystallization, it was performed XRD after every crystallization experiment and compared with the XRD patterns of the starting materials. The XRD patterns were obtained using a Rigaku MiniFlex 600 diffractometer in Bragg−Brentano geometry, with Cu Kα radiation (λ = 1.54178 Å) from a copper sealed tube with 40 kV and 15 mA, over the 2θ range of 3−40° with a step size of 0.01° and a speed of 10.0°/min.

Single crystal X-ray diffraction (SCXRD)

Data collection of single crystal X-ray diffraction of BTBT:$C_3F_7Cl_2$-NDI•TOL, ditBu-BTBT:$C_3F_7Cl_4$-NDI and BTBT:CF_3Cl_4-NDI was performed with a Rigaku Oxford Diffraction Xcalibur diffractometer with a Sapphire 3 detector using Mo Kα radiation (λ=0.71073 Å) at room temperature.

SCXRD measurements of ditBu-BTBT:$C_3F_7Cl_2$-NDI and BTBT:$C_4F_9Cl_4$-NDI crystals were made on a Bruker Apex-II diffractometer with a Photon II detector. Data collection was done with the Bruker APEX2 program and integrated and reduced with the Bruker SAINT software.

SCXRD data of BTBT:$C_3F_7Cl_4$-NDI was collected with the Bruker D8 Venture diffractometer with a microfocused source and Photon II detector using Mo Kα radiation (λ=0.71073 Å) at low temperature (200K).

The crystal structure was solved using OLEX 2-1.5 software by recurring to SHELXT codes that uses the intrinsic phasing and refined with SHELXL-2019/2 with least square L.S. command.

For visualization and image acquisition of the crystal structures it was used CCDC Mercury 2022.1.0.[21,22]

Differential Scanning Calorimetry (DSC)

The starting material and the crystals obtained were characterized by differential scanning calorimetry (DSC) using a Mettler-Toledo DSC-1 instrument. The samples were prepared by

accurately weighing approximately 1-4 mg of the powder in aluminum closed pans (40 μL) with a pinhole. The measurements were performed during two cycles of heating and cooling with a rate of 5°C/min under a dry N_2 atmosphere (flow rate 80 mL/min). All the data were analyzed using STARe software.

Thermo-Gravimetric Analysis-Evolved Gas analysis (TGA-EGA)

To characterize the solvate forms of the different materials, TGA-EGA was performed on Mettler-Toledo TGA coupled with a Thermo Nicolet iS 10IR FT_IR spectrometer with the scan rate of 10°C/min and analysed using STARe software.

FTIR spectroscopy

Infrared spectra of the CT crystals BTBT:$C_3F_7Cl_2$-NDI•TOL, ditBu-BTBT:$C_3F_7Cl_2$-NDI and their respective single components were recorded with a Bruker ifs66 Fourier transform IR (FT-IR) spectrometer coupled to an IR microscope Hyperion 1000 in transmission mode. The spectrometer is equipped with a liquid nitrogen cooled mercury cadmium telluride (MCT) detector.

Results and Discussion

Crystal structures

The structures of the CT complexes were obtained by single crystal X-ray diffraction. All the crystals used for the measurements have a needle like morphology, except BTBT:$C_3F_7Cl_4$-NDI that has a plate like morphology. Although the NDI molecules change only in the length of the fluorinated chains in the Cl_4-NDI series, the CT complexes show a dramatic variability in the crystal structure.

The first CT complexes considered have $C_3F_7Cl_2$-NDI as acceptor, with only two chlorines on the aromatic ring, and BTBT and ditBu-BTBT molecules as donor.

BTBT:$C_3F_7Cl_2$-NDI•TOL has a 1:1 D-A stoichiometry and the crystals are red and darker than the pristine reagents suggesting the presence of a stronger charge transfer. The crystal is a solvate with 1:1:1 ratio and was solved as triclinic P1 (see Table 2). The uncommon chiral group is due to the presence of the toluene molecule which cannot be described as disordered on the inversion center. The BTBT molecules are disordered over two positions, where one is predominant with 90% of occupancy, while the second position with 10% occupancy could only be described on the sulfur position. The D-A molecules pack in a 1:1 mixed stack where the donor and acceptor molecules alternate along the stacking direction with a distance between π-planes of 3.369 Å, Figure 3a). The molecular planes of BTBT and $C_3F_7Cl_2$-NDI are almost parallel with an inclination angle of 0.59° and there is a slight rotation of the molecules along their long axis of 13.09°, see Figure 3b). The solvent molecules are packed between the columns at the same plane as BTBT, as shown in Figure 3c).

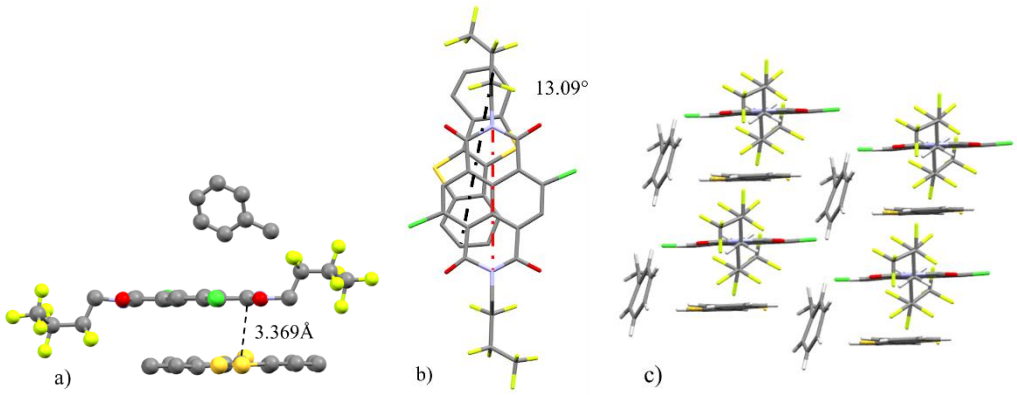

Figure 3 – Crystal structure details of BTBT:$C_3F_7Cl_2$-NDI•TOL without disorder of BTBT represented for better clarity, a) π-π stack distance, b) rotation angle, c) columnar arrangement of the DA stacks and solvent positioned between the columns.

In an attempt to avoid the presence of solvent in the crystal structure, we considered ditBu-BTBT supposing that its bulky chains could prevent the formation of voids in between the stacks and avoid solvent inclusion in the crystal structure. Indeed, the dark brown crystal of ditBu-BTBT:$C_3F_7Cl_2$-NDI appeared anhydrous and is monoclinic with space group P 2_1/n. Both the NDI and the ditBu-BTBT are on the inversion center and the molecular arrangement is in a 1:1 mixed stack D-A-D-A packing with a π-π stack distance of 3.395Å and a rotation displacement of the cores of 29.33°, Figure 4a) and 4b). There is also an inclination angle of 4.07° since the molecular planes of ditBu-BTBT and $C_3F_7Cl_2$-NDI are not parallel. It is worth noting that although the π-π distance is similar to the previous structure, the color is darker suggesting a better CT. The D-A stacking is parallel to the b axis the adjacent columns are generated by the symmetry operators, screw axis and glide, thus the molecules are arranged in a herringbone motif, as displayed at Figure 4 c).

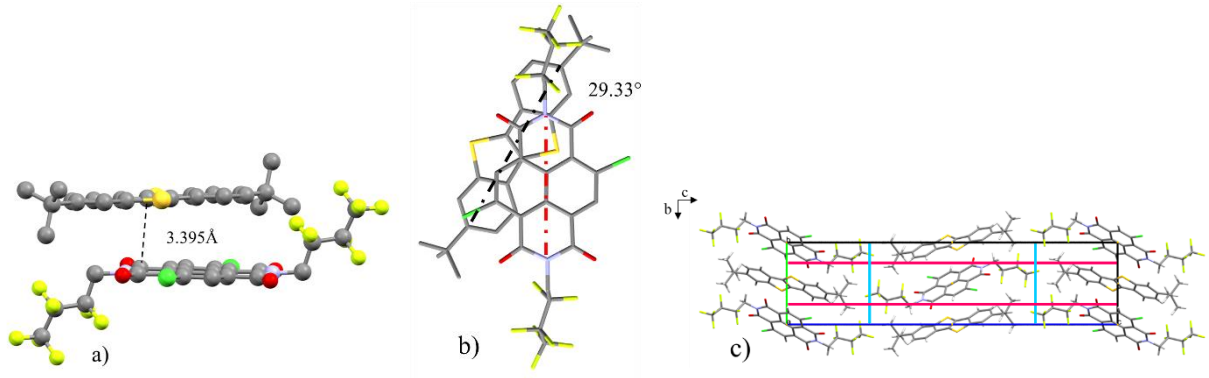

Figure 4 – Crystal structure details of ditBu-BTBT:$C_3F_7Cl_2$-NDI, a) π-π stack distance, b) rotation angle, c) herringbone motif formed by adjacent stacks due to symmetry elements, in pink glide operator and in blue screw symmetry.

We also explored the possibility to obatin CT complexes with the NDI with four chlorine atoms on the core. The higher substitution on the aromatic part increases the electronegativity of the acceptor and should promote the formation of CT. We used three different NDI molecules with different lengths of the fluorinated chains: CF_3-Cl_4-NDI, $C_3F_7Cl_4$-NDI, and $C_4F_9Cl_4$-NDI.

The co-crystals obtained are summarized in Table 1 and it is possible to verify that among the different combinations of donor and acceptors the behavior is quite different, in particular the crystals with C_3F_7Cl4-NDI which shows a different stoichiometry.

Table 1 – Co-crystals obtained with the series Cl_4-NDI as acceptor with different chain lengths and BTBT and ditBu-BTBT as donors, and their stoichiometry.

	BTBT	ditBu-BTBT
CF_3-Cl_4-NDI	1:1	---
$C_3F_7Cl_4$-NDI	1:2	1:2
$C_4F_9Cl_4$-NDI	1:1	---

BTBT:CF_3Cl_4-NDI crystallizes as $P2_1/c$ with both D and A molecules on the inversion center and with a 1:1 mixed stack packing, the D-A-D-A columns show a π-π stack of 3.408Å and an inclination of the molecular planes of 2.23°. The core of BTBT and CF_3Cl_4-NDI are almost aligned with a slight rotation angle of 4.60°. The BTBT is disordered over two positions flipped on the inversion center with occupancy 75:25.

The cell consists of two dimers of D-A that by translation along the shortest axis (c axis) form the stacking columns. These columns form a herringbone motif with the adjacent columns along the long axis (b axis) generated by the symmetry elements. The dark red color of the crystal suggests that the CT is not as strong as in the structures discussed above.

The CT complex of NDI with longest chains ($C_4F_9Cl_4$-NDI) and BTBT shows a very similar packing to BTBT:CF_3Cl_4-NDI: for this reason, it will be described later for sake of clarity and easier comparison.

The BTBT:$C_4F_9Cl_4$-NDI crystal is also monoclinic $P2_1/c$ with both D and A molecules on the inversion center, in the cell there are two dimers of D-A that create the stacking columns by translation along the short axis, that in this case is the a axis. As observed in BTBT:CF_3Cl_4-NDI, the stacking columns have a herringbone motif along the long axis (c axis) with the adjacent columns.

The columns have a D-A-D-A stack with a distance between π-planes of 3.417Å and an inclination angle of 1.85°. Contrary to BTBT:CF_3Cl_4-NDI, the core of the molecules is very twisted with a rotation angle of 66.78°. In this case, the BTBT is also disordered over two positions with occupancy ratio of 64:36.

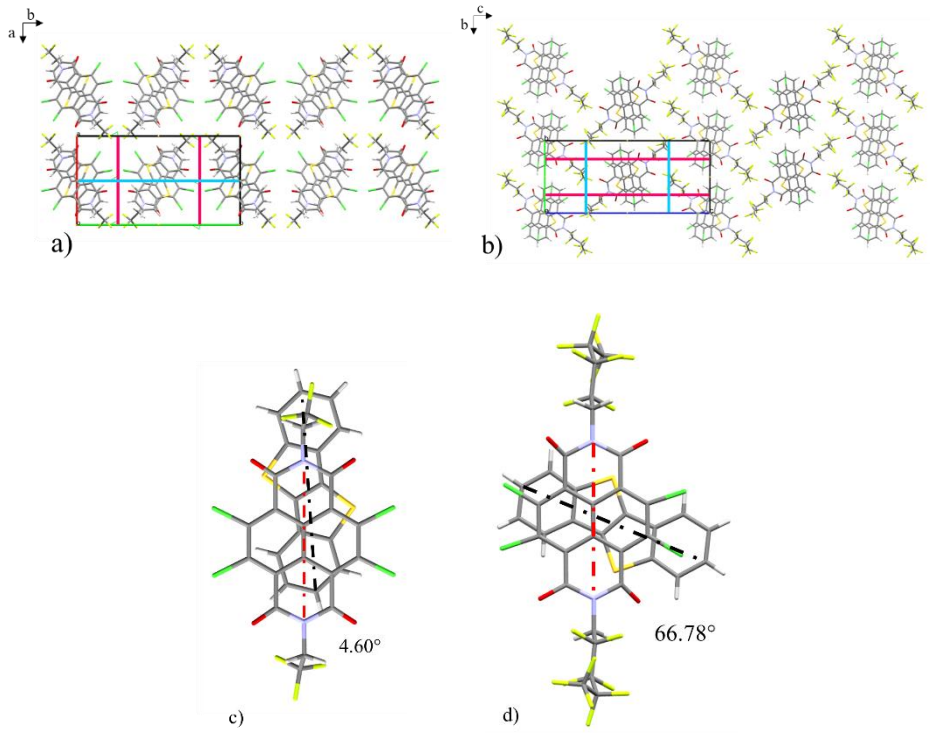

Figure 5 - Crystal structure details of BTBT:CF_3Cl_4-NDI (a and c) and BTBT:$C_4F_9Cl_4$-NDI (b and d), the BTBT disorder is not shown for better clarity. a) herringbone motif formed by adjacent stacks of BTBT:CF_3Cl_4-NDI, in pink glide operator and in blue screw symmetry, b) herringbone motif formed by adjacent stacks of BTBT:$C_4F_9Cl_4$-NDI, in pink glide operator and in blue screw symmetry, c) rotation angle of BTBT:CF_3Cl_4-NDI, d) rotation angle of BTBT:CF_3Cl_4-NDI.

In the case of $C_3F_7Cl_2$-NDI with BTBT and ditBu-BTBT, CT complexes obtained have a 1:2 D-A stoichiometry and very different arangements.

In BTBT:$C_3F_7Cl_4$-NDI the unit cell structure is triclinic with $P\bar{1}$ symmetry with one full NDI molecule and half BTBT in the asymmetric unit and BTBT positioned on the inversion centre. The BTBT molecules are disordered in two positions, with 75:25 occupancy ratio. The two positions are both located in the inversion centre with a rotation from each other of 54.80°, see Figure 6 a). The molecules pack in a A-D-A-A-D-A fashion, with BTBT molecules inserted in between the NDI pairs. The molecular planes of BTBT and $C_3F_7Cl_4$-NDI form an angle of 1.66° and are separated with a distance of 3.372Å. Furthermore, the long axis of the BTBT and $C_3F_7Cl_4$-NDI molecules form an angle of 62.19° and 60.99°, depending on the BTBT position, as depicted in Figure 6 b). The molecular planes of the NDI molecules are parallel and are separated by 3.351Å, but do not show a cofacial stack but rather a slipped stack with a shift along the short axis of the molecule of 3.59Å and along the long axis of 1.02Å, Figure 6 c).

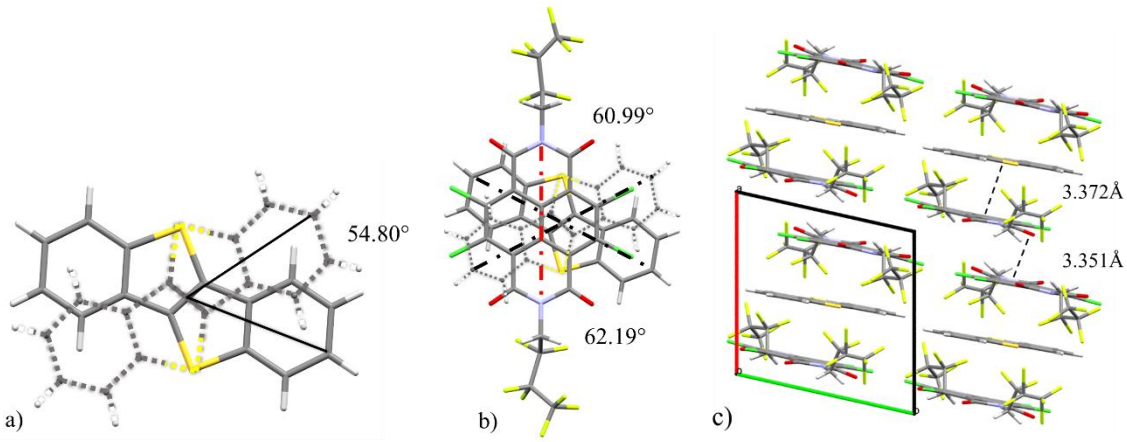

Figure 6 - Crystal structure details of BTBT:$C_3F_7Cl_4$-NDI, a) disorder of BTBT and angle between the two positions, b) rotation angle, c) columnar arrangement of the DA stacks and π-π plane distance.

The ditBu-BTBT: $C_3F_7Cl_4$-NDI crystal has a triclinic unit cell with $P\bar{1}$ space group, the asymmetric unit contains half molecule of ditBu-BTBT and two halves of NDI. Regardless the stoichiometry, the crystal structure forms 1:1 stacks in a D-A-D-A packing while the extra NDI molecule is placed aside of the D-A-D-A column with the aromatic ring almost perpendicular to the stacking plane, and are not directly involved in the CT. The chlorine atoms of the NDIs in the columns point towards the aromatic ring of the extra NDI molecule Figure 7 b). Inside the stack the π-planes are separated by 3.392Å and are not completely parallel with an inclination angle of 1.97°. In this case the molecules of ditBu-BTBT and $C_3F_7Cl_4$-NDI are also fairly rotated in relation to each other, more specifically with a rotation angle of 45.41°.

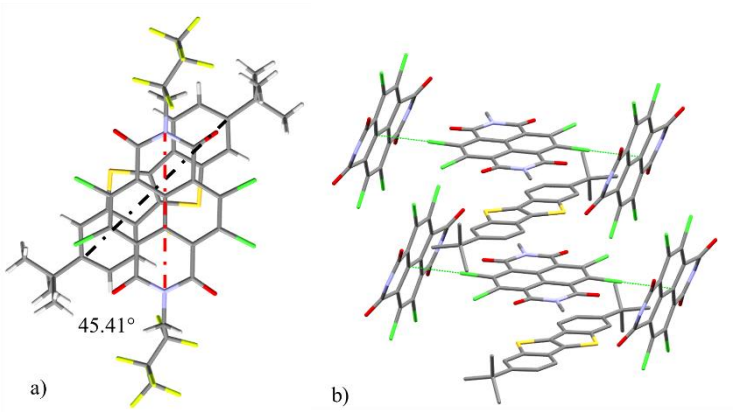

Figure 7 - Crystal structure details of ditBu-BTBT:$C_3F_7Cl_4$-NDI, a) rotation angle, b) columnar arrangement of the DA stacks, with the chlorine of the NDI pointing to the NDI molecules not involved in the CT.

Table 2 – Crystal structure parameters of BTBT:$C_3F_7Cl_2$-NDI•TOL, ditBu-BTBT: $C_3F_7Cl_2$-NDI, BTBT:$C_3F_7Cl_4$-NDI, ditBu-BTBT: $C_3F_7Cl_4$-NDI, BTBT:CF_3Cl_4-NDI and BTBT:$C_4F_9Cl_4$-NDI.

	BTBT: $C_3F_7Cl_2$-NDI •TOL	ditBu-BTBT: $C_3F_7Cl_2$-NDI	BTBT: 2($C_3F_7Cl_4$-NDI)	ditBu-BTBT: 2($C_3F_7Cl_4$-NDI)	BTBT: CF_3Cl_4-NDI	BTBT: $C_4F_9Cl_4$-NDI
Temperature (K)	RT	273	200	100	RT	110
Formula	$C_{22}H_6Cl_2F_{14}N_2O_4$, $C_{14}H_8S_2$, C_7H_8	$C_{22}H_6Cl_2F_{14}N_2O_4$, $C_{22}H_{24}S_2$	2($C_{22}H_4Cl_4F_{14}N_2O_4$) $C_{14}H_8S_2$	2($C_{22}H_4Cl_4F_{14}N_2O_4$), $C_{22}H_{24}S_2$	$C_{18}H_4Cl_4F_6N_2O_4$, $C_{14}H_8S_2$	$C_{24}H_4Cl_4F_{18}N_2O_4$, $C_{14}H_8S_2$
Molecular weight	1031.64	1051.72	1776.47	1888.67	808.36	1108.42
Crystal system	Triclinic	Monoclinic	Triclinic	Triclinic	Monoclinic	Monoclinic
Space group	P1	P 2_1/n	P$\bar{1}$	P$\bar{1}$	P 2_1/c	P 2_1/c
a (Å)	8.1612(15)	7.1095(3)	10.4799(3)	7.1978(6)	10.2799(13)	7.0950(5)
b (Å)	11.0641(15)	8.4838(3)	10.7924(2)	14.2198(9)	18.448(3)	10.9022(7)
c (Å)	12.273(2)	34.3099(13)	14.5090(3)	17.7108(15)	8.1620(19)	25.0163(17)
α (°)	91.280(13)	90	103.864(2)	96.318(6)	90	90
β (°)	109.228(17)	91.007(2)	90.0838(19)	101.537(7)	103.173(17)	91.356(3)
γ (°)	98.998(14)	90	102.219(2)	102.462(6)	90	90
V ($Å^3$)	1030.26	2069.1	1554.76	1711.87	1507.14	1934.5
Z/Z'	1/1	2/0.5	1/0.5	1/0.5	2/0.5	2/0.5
Density ($g.cm^{-3}$)	1.664	1.688	1.897	1.832	1.781	1.903
F(000)	518	1064	876	940	808	1096
GOF on F^2	1.030	1.049	1.094	1.155	1.001	1.065
R_1 (on F, $I>2\sigma(I)$/ R_{ex})	0.0837	0.0331	0.0744	0.1056	0.0669	0.0810
WR_2 (F^2 all data) R_{wp}	0.2135	0.0918	0.2170	0.1900	0.1241	0.2399

Thermal characterization

We performed DSC on the solid product of the CT complexes formed by $C_3F_7Cl_2$-NDI and $C_3F_7Cl_4$-NDI. Additionally, TGA was also performed on BTBT:$C_3F_7Cl_2$-NDI•TOL and ditBu-BTBT:$C_3F_7Cl_2$-NDI to investigate the thermal behavior. Not all the CT complexes were covered by thermal analysis due to proximity of thesis submission deadline: further characterization are programmed for future.

TGA and EGA analysis of BTBT:$C_3F_7Cl_2$-NDI•TOL confirmed the solvate nature of the phase suggesting a stoichiometry of 1:1:1 with a molecule of toluene for each molecule of BTBT and $C_3F_7Cl_2$-NDI. The toluene molecules are released from the crystal lattice above 80°C but if the solvate is stored exposed at room conditions appeared stable for more than one month. On contrary, ditBu-BTBT: $C_3F_7Cl_2$-NDI showed no mass loss in the TGA confirming the anhydrous nature as observed by single crystal XRD.

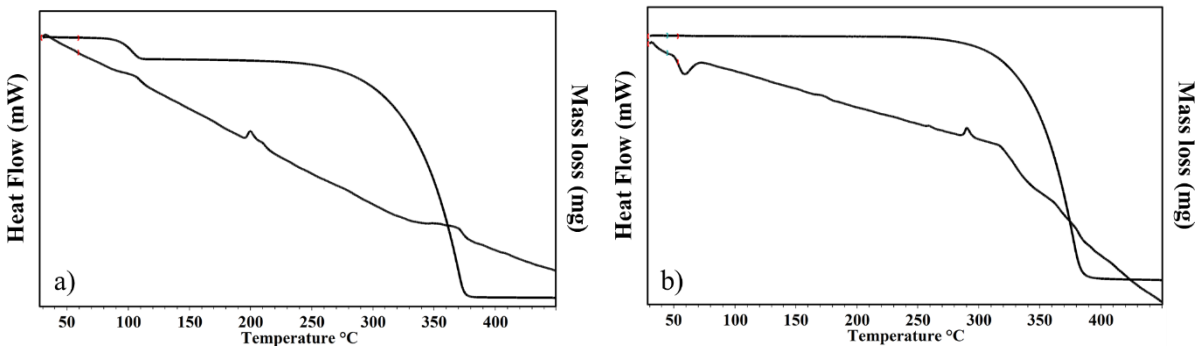

Figure 8 – TGA analysis of a) BTBT:$C_3F_7Cl_2$-NDI•TOL where it can be observed the loos of solvent, and b) ditBu-BTBT: $C_3F_7Cl_2$-NDI.

To study the unsolvated BTBT:$C_3F_7Cl_2$-NDI, we annealed the powder of BTBT:$C_3F_7Cl_2$-NDI•TOL at 80°C for 1h on a hot plate: a color change from the bright orange/red to a darker brownish red was observed, as shown in inset at Figure 9. After annealing, the new dark powder was characterized by XRPD. For better clarity the pattern of the new powder was compared with the calculated pattern obtained using the crystal structure of BTBT:$C_3F_7Cl_2$-NDI•TOL, since the experimental results have two peaks ascribable to the original material $C_3F_7Cl_2$-NDI. In the unsolvated material the main peaks of BTBT:$C_3F_7Cl_2$-NDI•TOL disappear, and a new powder pattern appeared with one peak at 4.7° indicating a longer d-spacing. Most importantly, these results show that after losing the solvent the CT complex does not lose crystallinity and packs in a new unsolvated molecular arrangement. The fact that the new form is darker suggests that the CT in the new complex is stronger than in BTBT:$C_3F_7Cl_2$-NDI•TOL, for that reason it would be very interesting to run some calculations on both forms.

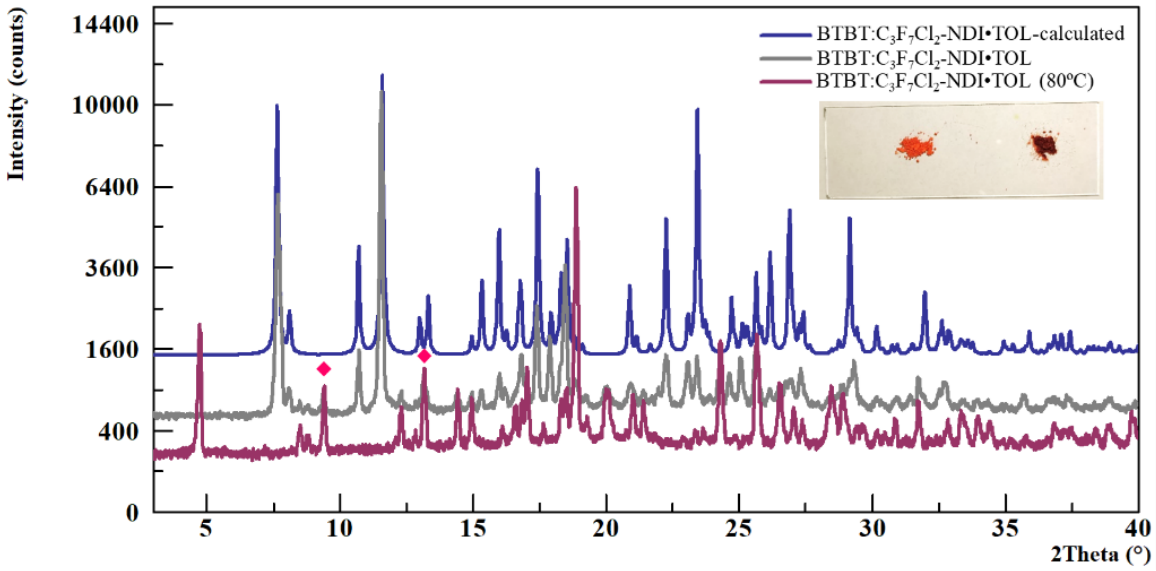

Figure 9 – XRD pattern of BTBT:$C_3F_7Cl_2$-NDI•TOL obtained experimentally (grey) and calculated (blue). XRD pattern of BTBT:$C_3F_7Cl_2$-NDI•TOL after annealing at 80°C and further desolvation (purple). Some peaks observed in the experimental patterns, highlighted with a pink symbol, are related to pure $C_3F_7Cl_2$-NDI.

For all the CT complexes, DSC analysis was performed with two cycles of heating and cooling.

The DSC profile of BTBT:$C_3F_7Cl_2$-NDI•TOL is displayed in Figure 10a).During the first heating, a broad endothermic event at 98°C (onset 81°C) ascribable to the release of toluene can be observed, a second sharp endothermic event at 200°C is followed by a broad small peak possibly related to a liquid crystal formation.

On the second heating, since the compound is no longer a solvate, there is no peak related to the loss of toluene but the behavior in the 200°C region appears slightly more complex, with one extra peak present.

At this stage it is not possible to clearly assign the nature of the events and further studies have been programmed (XRPD analysis after recrystallization from the melt).

The DSC analysis of ditBu-BTBT:$C_3F_7Cl_2$-NDI is reported in Figure 10b). The DSC profiles appeared more straight forward, with only two peaks present on the first heating, one at 168°C with low enthalpy and another attributed to the melting at 289°C. A small signal has been detected in the 80-100°C region during cooling and second heating as *exo*- and *endo*- respectively: at present day, no clear description of the event is proposed since further characterizations are still in progress.

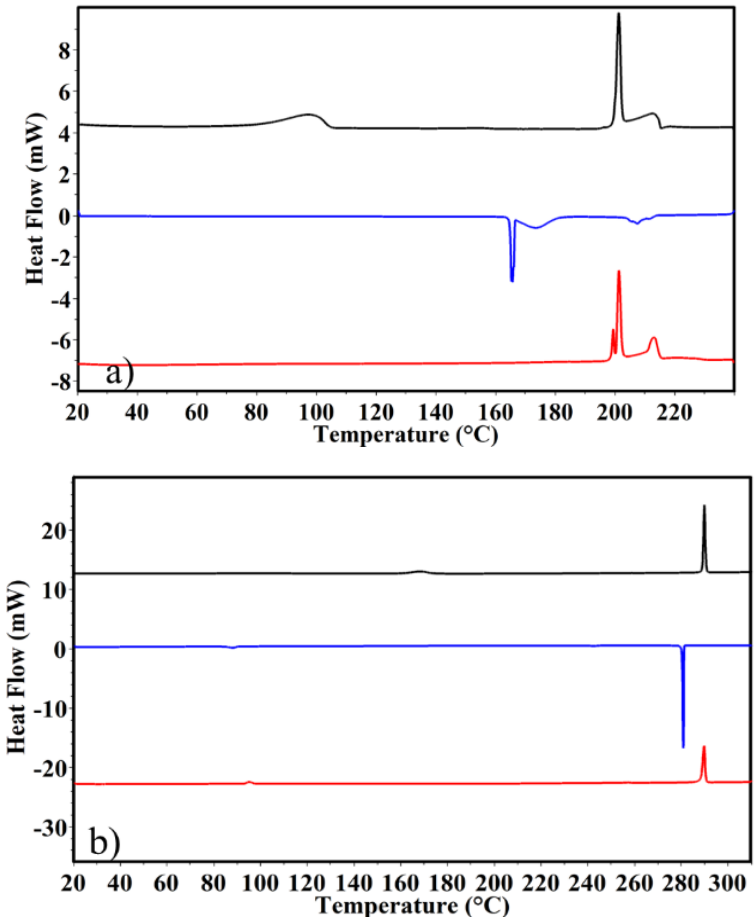

Figure 10 – DSC curves of a) BTBT:$C_3F_7Cl_2$-NDI•TOL and b) ditBu-BTBT:$C_3F_7Cl_2$-NDI, black line: first heating, blue line: cooling and red line: second heating.

The DSC analysis of BTBT:$C_3F_7Cl_4$-NDI, Figure 11a), on the first heating shows a complex endothermic peak in the 270-290°C region likely ascribable to sample melting even if degradative process involvement cannot be excluded.

The second heating showed endothermic peaks shifted to higher temperatures, as already stated above, at this stage it is not possible to clearly assign the nature of the events and further studies have been planned.

In the case of ditBu-BTBT:$C_3F_7Cl_4$-NDI, Figure 11b), no transitions were observed, and the endothermic peak associated to the phase melting at 263°C was observed in both heating cycles as well as the crystallization peak during the cooling branch at lower temperature (250°C).

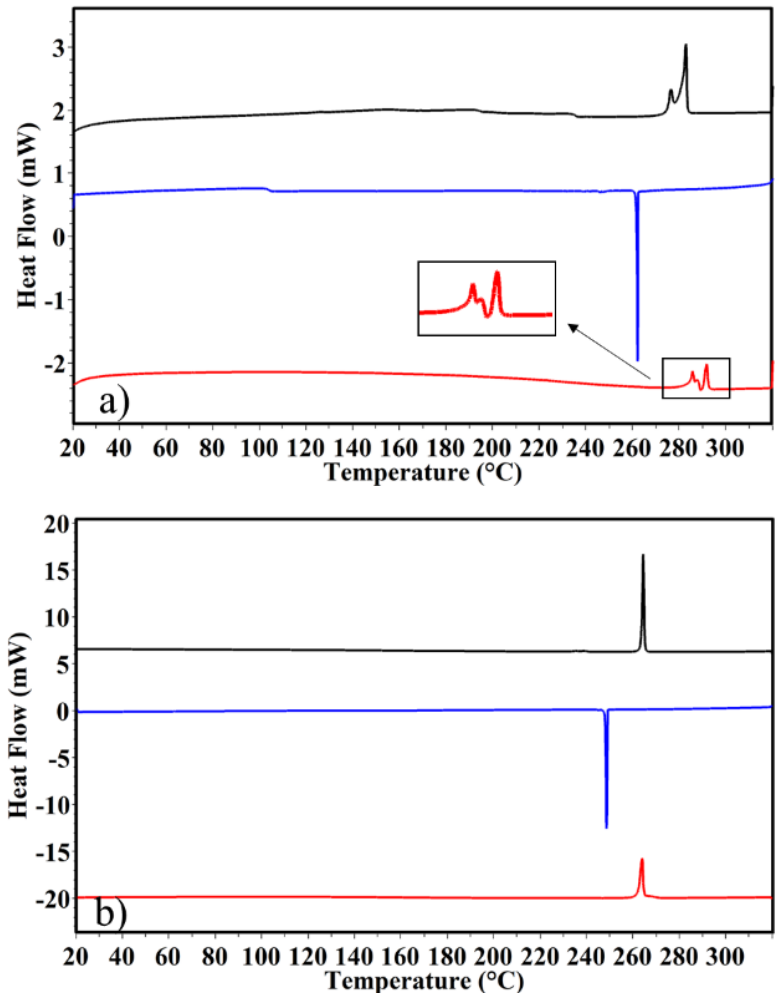

Figure 11 – DSC curves of a) BTBT:$C_3F_7Cl_4$-NDI and b) ditBu-BTBT:$C_3F_7Cl_4$-NDI, black line: first heating, blue line: cooling and red line: second heating.

Infrared Spectra

ATR-FTIR spectra of $C_3F_7Cl_2$-NDI, BTBT, ditBu-BTBT and respective CT complexes were collected in the region 4000-500 cm^{-1}.

Since there was not enough time to study all the co-crystals with infrared spectroscopy, we chose to study only BTBT:$C_3F_7Cl_2$-NDI•TOL and ditBu-BTBT:$C_3F_7Cl_2$-NDI. This choice was based on the very dark color of the crystals of ditBu-BTBT:$C_3F_7Cl_2$-NDI and to be able to compare the behavior of two D-A complexes with the same acceptor and different but similar donors.

The full spectra of $C_3F_7Cl_2$-NDI, BTBT and BTBT:$C_3F_7Cl_2$-NDI•TOL are displayed in Figure 12 a). In general, the spectrum of the CT complex is more similar to the one of NDI than the BTBT spectrum. Moreover, the CT complex spectrum shows a shift of several bands compared to the spectrum of the isolated components. The most significant shifts are observed in the region 1500-1000 cm^{-1} as shown in Figure 12 b): more specifically the characteristic bands from $C_3F_7Cl_2$-NDI at 1241, 1213, 1187 and 1108 cm^{-1} appear to shift frequency to 1235, 1219, 1206 and 1098 cm^{-1} respectively, this shifts confirms the electronic charge transfer transition.

The broad band at 3438 cm^{-1} suggests potential absorption of water by the CT complex, since this band is normally associated to a hydroxyl group O-H stretching vibration.

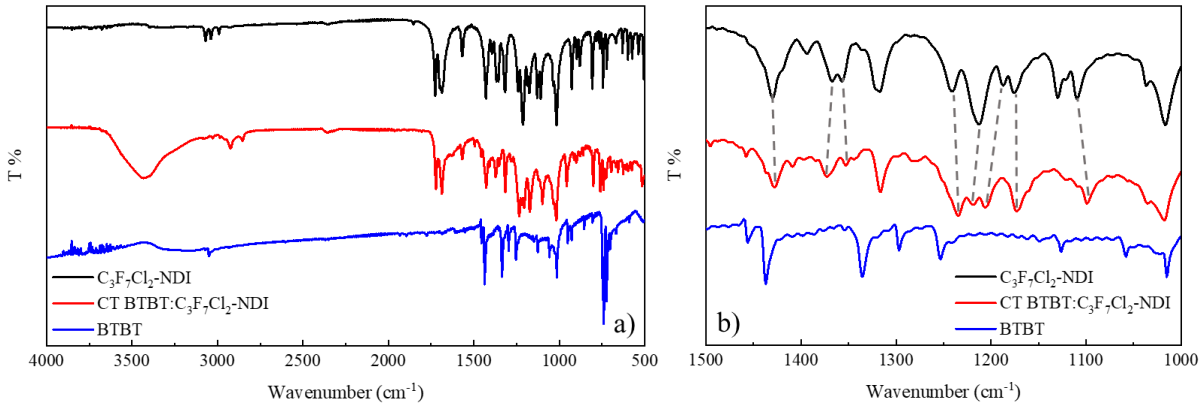

Figure 12 – ATR-FTIR spectra of BTBT:$C_3F_7Cl_2$-NDI•TOL, a) full spectra and b) 1500-1000 cm^{-1} region.

The CT complex ditBu-BTBT:$C_3F_7Cl_2$-NDI and its respective reactants were also characterized by ATR-FTIR and their spectra can be observed at Figure 13 a). In this case the spectrum of the CT complex appears to have a more significant contribution of the donor compared to the previous CT, nonetheless the most significant contribution continues to be from the acceptor. The spectrum of the complex seemed to have some bands shifted in relation to the original bands from both donor and acceptor. In the region 3000-2800 cm^{-1}, the CT complex have the same bands as the donor with a significant shift, precisely the donor bands at 2963, 2950, 2898 and 2865 cm^{-1} shift to 2983, 2966, 2924 and 2881 cm^{-1} respectively, Figure 13 a). In the region 1500-1000 cm^{-1} it also observed a shift in the bands but not as substantial, in this case the shifted bands are both from the BTBT derivative and the NDI derivative, once again the shift of the bands confirms the electronic charge transfer transition.

The assignment of the FT-IR bands was not performed at this stage and further in-depth investigation is programmed to gain more insight into the vibrational spectra interpretation.

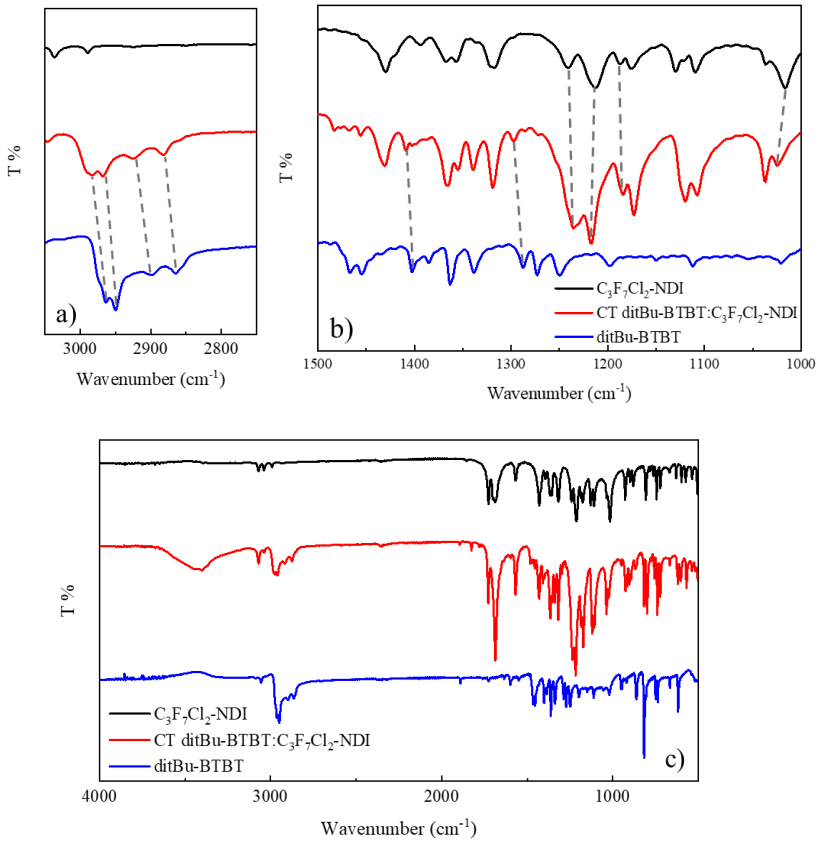

Figure 13 – ATR-FTIR spectra of ditBu-BTBT:$C_3F_7Cl_2$-NDI, a) 3000-2800 cm^{-1} region, b) 1500-1000 cm^{-1} region and c) full spectra.

Conclusions

We have reported the design of some novel CT co-crystals based on NDI derivatives and BTBT and ditBu-BTBT. We studied the crystal structure of six different complexes and found that depending on the starting single components very different packing arrangements and even different stoichiometries can be obtained.

The two co-crystals obtained with $C_3F_7Cl_2$-NDI are significantly different depending on the donor molecule. The D-A complex with BTBT was isolated as a solvate and when we replace the BTBT with a bulkier molecule such as ditBu-BTBT, the crystal obtained does not have present toluene molecules and it showed a much darker color indicating higher CT. In fact, when we anneal BTBT:$C_3F_7Cl_2$-NDI•TOL to promote the desolvation the solid product gets darker, suggesting that the packing without solvent may be closer to the one observed in the co-crystal with ditBu-BTBT.

In general, the most common stoichiometry observed is 1:1 but when using $C_3F_7Cl_4$-NDI as an acceptor the CT complexes formed with both BTBT and ditBu-BTBT have a 1:2 stoichiometry. Furthermore, we investigated the influence of chain length in the Cl_4-NDI family, by studying CT complexes formed with CF_3-Cl_4-NDI, $C_3F_7Cl_4$-NDI, $C_4F_9Cl_4$-NDI and BTBT. Surprisingly the

crystal structures that show bigger similarities are the one with the shortest chain length and the one with the longest.

We analyzed the thermal behavior of the CT complexes formed by $C_3F_7Cl_2$-NDI and $C_3F_7Cl_4$-NDI. In both cases the CT complexes with ditBu-BTBT have a much simpler behavior with a single sharp peak ascribable to the melting, while the BTBT complexes show several thermal events occurring close to the melting temperature.

By infrared spectroscopy we were able to confirm the D-A intimate interaction in the co-crystals of BTBT:$C_3F_7Cl_2$-NDI and ditBu-BTBT:$C_3F_7Cl_2$-NDI based on the shift of the bands observed especially in the region 1500-1000 cm^{-1}.

References

(1) Zhang, J.; Jin, J.; Xu, H.; Zhang, Q.; Huang, W. Recent Progress on Organic Donor–Acceptor Complexes as Active Elements in Organic Field-Effect Transistors. *J. Mater. Chem. C* **2018**, *6* (14), 3485–3498. https://doi.org/10.1039/C7TC04389A.

(2) Goetz, K. P.; Tsutsumi, J.; Pookpanratana, S.; Chen, J.; Corbin, N. S.; Behera, R. K.; Coropceanu, V.; Richter, C. A.; Hacker, C. A.; Hasegawa, T.; Jurchescu, O. D. Polymorphism in the 1:1 Charge-Transfer Complex DBTTF–TCNQ and Its Effects on Optical and Electronic Properties. *Adv. Electron. Mater.* **2016**, *2* (10), 1600203. https://doi.org/10.1002/aelm.201600203.

(3) Yee, N.; Dadvand, A.; Perepichka, D. F. Band Gap Engineering of Donor–Acceptor Co-Crystals by Complementary Two-Point Hydrogen Bonding. *Mater. Chem. Front.* **2020**, *4* (12), 3669–3677. https://doi.org/10.1039/D0QM00500B.

(4) Vermeulen, D.; Zhu, L. Y.; Goetz, K. P.; Hu, P.; Jiang, H.; Day, C. S.; Jurchescu, O. D.; Coropceanu, V.; Kloc, C.; McNeil, L. E. Charge Transport Properties of Perylene–TCNQ Crystals: The Effect of Stoichiometry. *J. Phys. Chem. C* **2014**, *118* (42), 24688–24696. https://doi.org/10.1021/jp508520x.

(5) Goetz, K. P.; Vermeulen, D.; Payne, M. E.; Kloc, C.; McNeil, L. E.; Jurchescu, O. D. Charge-Transfer Complexes: New Perspectives on an Old Class of Compounds. *J. Mater. Chem. C* **2014**, *2* (17), 3065–3076. https://doi.org/10.1039/C3TC32062F.

(6) Fijahi, L.; Salzillo, T.; Tamayo, A.; Bardini, M.; Ruzié, C.; Quarti, C.; Beljonne, D.; d'Agostino, S.; Geerts, Y. H.; Mas-Torrent, M. Charge Transfer Complexes of a Benzothienobenzothiophene Derivative and Their Implementation as Active Layer in Solution-Processed Thin Film Organic Field-Effect Transistors. *J. Mater. Chem. C* **2022**, *10* (18), 7319–7328. https://doi.org/10.1039/D2TC00655C.

(7) Wang, C.; Wang, J.; Wu, N.; Xu, M.; Yang, X.; Lu, Y.; Zang, L. Donor–Acceptor Single Cocrystal of Coronene and Perylene Diimide: Molecular Self-Assembly and Charge-Transfer Photoluminescence. *RSC Adv.* **2017**, *7* (4), 2382–2387. https://doi.org/10.1039/C6RA25447K.

(8) Yeh, M.-Y.; Lin, H.-C. Theoretical Analysis of the Intermolecular Interactions in Naphthalene Diimide and Pyrene Complexes. *Phys. Chem. Chem. Phys.* **2014**, *16* (44), 24216–24222. https://doi.org/10.1039/C4CP03879G.

(9) Nicholas Blagden; David J. Berry. Current Directions in Co-Crystal Growth. *New J. Chem.* **2008**, *32*, 1659–1672. https://doi.org/10.1039/b803866j.

(10) Zhang, J.; Xu, W.; Sheng, P.; Zhao, G.; Zhu, D. Organic Donor–Acceptor Complexes as Novel Organic Semiconductors. *Acc. Chem. Res.* **2017**, *50* (7), 1654–1662. https://doi.org/10.1021/acs.accounts.7b00124.

(11) Wang, J.; Zhang, S.; Xu, S.; Li, A.; Li, B.; Ye, L.; Geng, Y.; Tian, Y.; Xu, W. Morphology-Dependent Luminescence and Optical Waveguide Property in Large-Size Organic Charge Transfer Cocrystals with Anisotropic Spatial Distribution of Transition Dipole Moment. *Adv. Optical Mater.* **2020**, *8* (2), 1901280. https://doi.org/10.1002/adom.201901280.

(12) Liu, H.; Liu, Z.; Jiang, W.; Fu, H. Tuning the Charge Transfer Properties by Optimized Donor – Acceptor Cocrystal for FET Applications: From P Type to N Type. *Journal of Solid State Chemistry* **2019**, *274*, 47–51. https://doi.org/10.1016/j.jssc.2019.03.017.

(13) Solano, F.; Inaudi, P.; Abollino, O.; Giacomino, A.; Chiesa, M.; Salvadori, E.; Kociok-Kohn, G.; da Como, E.; Salzillo, T.; Fontanesi, C. Charge Transfer Modulation in Charge Transfer Co-Crystals Driven by Crystal Structure Morphology. *Phys. Chem. Chem. Phys.* **2022**, *24* (31), 18816–18823. https://doi.org/10.1039/D2CP01408D.

(14) Salzillo, T.; Masino, M.; Kociok-Köhn, G.; Di Nuzzo, D.; Venuti, E.; Della Valle, R. G.; Vanossi, D.; Fontanesi, C.; Girlando, A.; Brillante, A.; Da Como, E. Structure, Stoichiometry, and Charge Transfer in Cocrystals of Perylene with TCNQ-F_x. *Crystal Growth & Design* **2016**, *16* (5), 3028–3036. https://doi.org/10.1021/acs.cgd.5b01663.

(15) Mandal, A.; Choudhury, A.; Kumar, R.; Iyer, P. K.; Mal, P. Exploring the Semiconductor Properties of a Charge Transfer Cocrystal of 1-Aminopyrene and TCNQ. *CrystEngComm* **2020**, *22* (4), 720–727. https://doi.org/10.1039/C9CE01507H.
(16) Jin, J.; Wu, S.; Ma, Y.; Dong, C.; Wang, W.; Liu, X.; Xu, H.; Long, G.; Zhang, M.; Zhang, J.; Huang, W. Nucleation Control-Triggering Cocrystal Polymorphism of Charge-Transfer Complexes Differing in Physical and Electronic Properties. *ACS Appl. Mater. Interfaces* **2020**, *12* (17), 19718–19726. https://doi.org/10.1021/acsami.9b23590.
(17) Mori, T.; Inokuchi, H. Crystal Structure of the Mixed-Stacked Salt of Bis(Ethylenedithio)Tetrathiafulvalene (BEDT-TTF) and Tetracyanoquinodimethane (TCNQ). *Bull Chem Soc Jpn* **1987**, *60*, 402–404.
(18) Mori, T.; Kawamoto, T. Organic Conductors—from Fundamentals to Nonlinear Conductivity. *Annu. Rep. Prog. Chem., Sect. C: Phys. Chem.* **2007**, *103*, 134–172. https://doi.org/10.1039/B605647B.
(19) N. S. Saleesh Kumar. Evidence of Preferential π-Stacking a Study of Intermolecular and Intramolecular Charge Transfer Complexes. *ChemComm* **2010**, *46*, 5464–5466.
(20) Kobaisi, M. A.; Bhosale, R. S.; El-Khouly, M. E.; La, D. D.; Padghan, S. D.; Bhosale, S. V.; Jones, L. A.; Antolasic, F.; Fukuzumi, S.; Bhosale, S. V. The Sensitivity of Donor – Acceptor Charge Transfer to Molecular Geometry in DAN – NDI Based Supramolecular Flower-like Self-Assemblies. *Sci Rep* **2017**, *7* (1), 16501. https://doi.org/10.1038/s41598-017-15599-9.
(21) Macrae, C. F.; Bruno, I. J.; Chisholm, J. A.; Edgington, P. R.; McCabe, P.; Pidcock, E.; Rodriguez-Monge, L.; Taylor, R.; van de Streek, J.; Wood, P. A. It Mercury CSD 2.0 – New Features for the Visualization and Investigation of Crystal Structures. *Journal of Applied Crystallography* **2008**, *41* (2), 466–470. https://doi.org/10.1107/S0021889807067908.
(22) Macrae, C. F.; Sovago, I.; Cottrell, S. J.; Galek, P. T. A.; McCabe, P.; Pidcock, E.; Platings, M.; Shields, G. P.; Stevens, J. S.; Towler, M.; Wood, P. A. It Mercury 4.0: From Visualization to Analysis, Design and Prediction. *Journal of Applied Crystallography* **2020**, *53* (1), 226–235. https://doi.org/10.1107/S1600576719014092.

Chapter 6: Conclusions

The goal of this thesis was to compare in a critical way bulk and substrate-induced polymorphism for best-performing semiconductors. I focused my attention on naphthalene diimides (NDI) derivatives which show high conductivity as n-type semiconductors and have great versatility on deposition processing due to their high solubility. During the thesis, I have acquired good skills and competencies in polymorphic investigation and solid-state characterizations like structure determination by X-ray diffraction on single-crystal (SCXRD) and powder (XRPD), thermal characterization by DSC, TGA, variable-temperature X-ray diffraction (VTXRD) and hot stage microscopy.

In the first chapters, I explored and reviewed the crystal forms of N, N'-bis(n-hexyl) naphthalene-1,4,5,8-tetracarboxylicdiimide (NDI-C6) both in bulk and in thin film, with special attention to the thermal behavior. The measurements at variable temperature were collected at beam-line MS-X04SA of the PSI synchrotron, ID proposal 20201790. The results highlighted the interesting behavior of NDI-C6 which shows different solid-solid transitions depending on the thermal history and high thermal expansion of the material. The results were presented at the Faraday discussions: On the Crystal forms of NDI-C6: annealing and deposition procedures to access elusive polymorphs and published on the Faraday discussions journal.

During my secondment at the university of Graz, I studied the thin films of NDI-C6 to identify possible surface induced polymorphism of NDI-C6 and in particular the possibility to obtain the pure phases of NDI-C6. Thin films were characterized by X-ray reflectivity and grazing incidence X-ray diffraction, in the last case the measurements were collected at Elettra Sincrotrone Trieste at the X-ray Diffraction 1 (XRD1) beamline, and it was possible to confirm the presence of the new phase ε which was observed only as thin film.

Using the optimized conditions to get pure phases, I produced OFET devices and studied the morphology of the different polymorphs during my secondment at the University of Cambridge. Unfortunately, the devices characterized did not show a good performance and the small differences observed are likely related to the morphology of the films. Considering that none of

the phases shows good uniformity and coverage, it was impossible to compare the different polymorphs' charge transport and electrical properties as reported in the third chapter.

In the second part of my thesis, I focused on core-chlorinated NDIs with fluorinated side chains. These molecules were provided by BASF a partner of the UHMob consortium. Initially, I performed polymorph screening in three molecules with the same core (Cl_4-NDI) and different side chain lengths (CF_3, C_3F_7 and C_4F_9) as reported in the Chapter 4. To study the behavior of the systems at high temperatures I collected VT-XRPD at BL04-MSPD beamline of ALBA synchrotron, ID proposal 2020094721.

The formation of the solvate form of CF_3-NDI•PXY prompted me to study the formation of CT complexes. These types of co-crystals are being studied as new innovative materials. The NDIs show a high propensity to form donor-acceptor co-crystals with BTBT and ditBu-BTBT, six different D-A co-crystals were obtained. Chapter 5 covered the synthesis and characterization of the D-A co-crystals obtained by means of X-ray diffraction, and FTIR spectroscopy in collaboration with Dr Tommaso Salzillo (Univeristy of Bologna). Unfortunately, this fruitful field of my research started only during the last semester of the PhD, and I could not go into it properly due to lack of time.

The UHMob project also promoted networking and collaborations amongst the early-stage-researchers (ESRs) which were fundamental during my secondments, and the supportive network was reinforced during the semestral meetings of the UHMob project.

Appendix A

On the Crystal forms of NDI-C6: annealing and deposition procedures to access elusive polymorphs

Inês de Oliveira Martins[ab], *Francesco Marin*[b], *Enrico Modena**[a], *Lucia Maini**[b]

[a]PolyCrystalLine SPA, Via Della Cooperazione, 29 40059 – Medicina (BO) Italy
[b]Dipartimento di Chimica "G. Ciamician", via Selmi 2 −Università di Bologna, I-40126, Bologna, Italy

Supplementary information

Table S1 - List of Solvents used for solubility screening.

S. No	Solvent	abbreviation	Soluble
1	isopropanol	2PR	No
2	acetonitrile	ACN	No
3	acetone	ACT	No
4	chloroform	CHF	> 100g/L
5	dichloromethane	DCM	> 100g/L
6	dimethylformamide	DMF	~10 g/L @ 50°C
7	dimethyl sulfoxide	DMSO	~10 g/L @ 75°C
8	ethyl acetate	ETA	No
9	water	H2O	No
10	methanol	MET	No
11	p-xylene	PXY	~28mg/ml
12	toluene	TOL	~25mg/ml

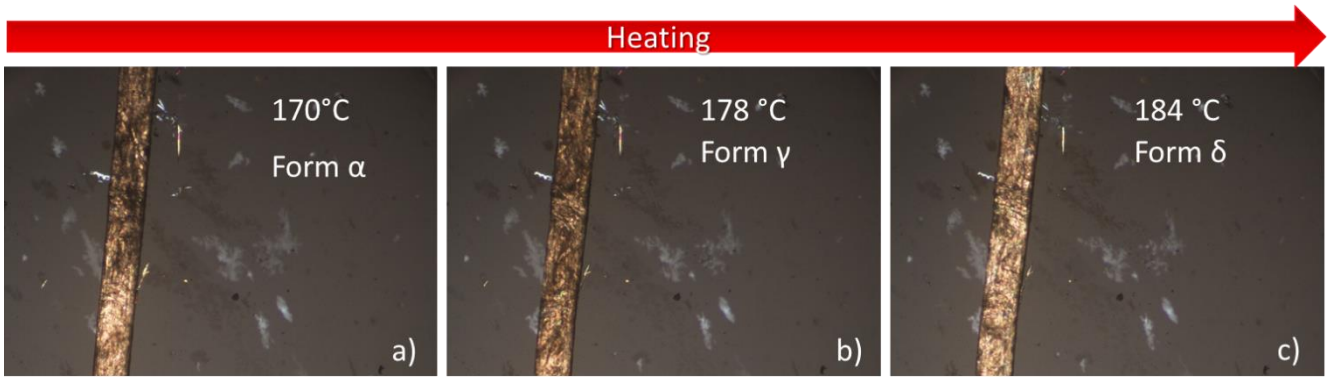

Figure S1 - Hot stage microscopy during the heating of a single crystal NDI-C6, a) Form α at 170°C, b) Form γ at 178°C, c) Form δ at 184°C.

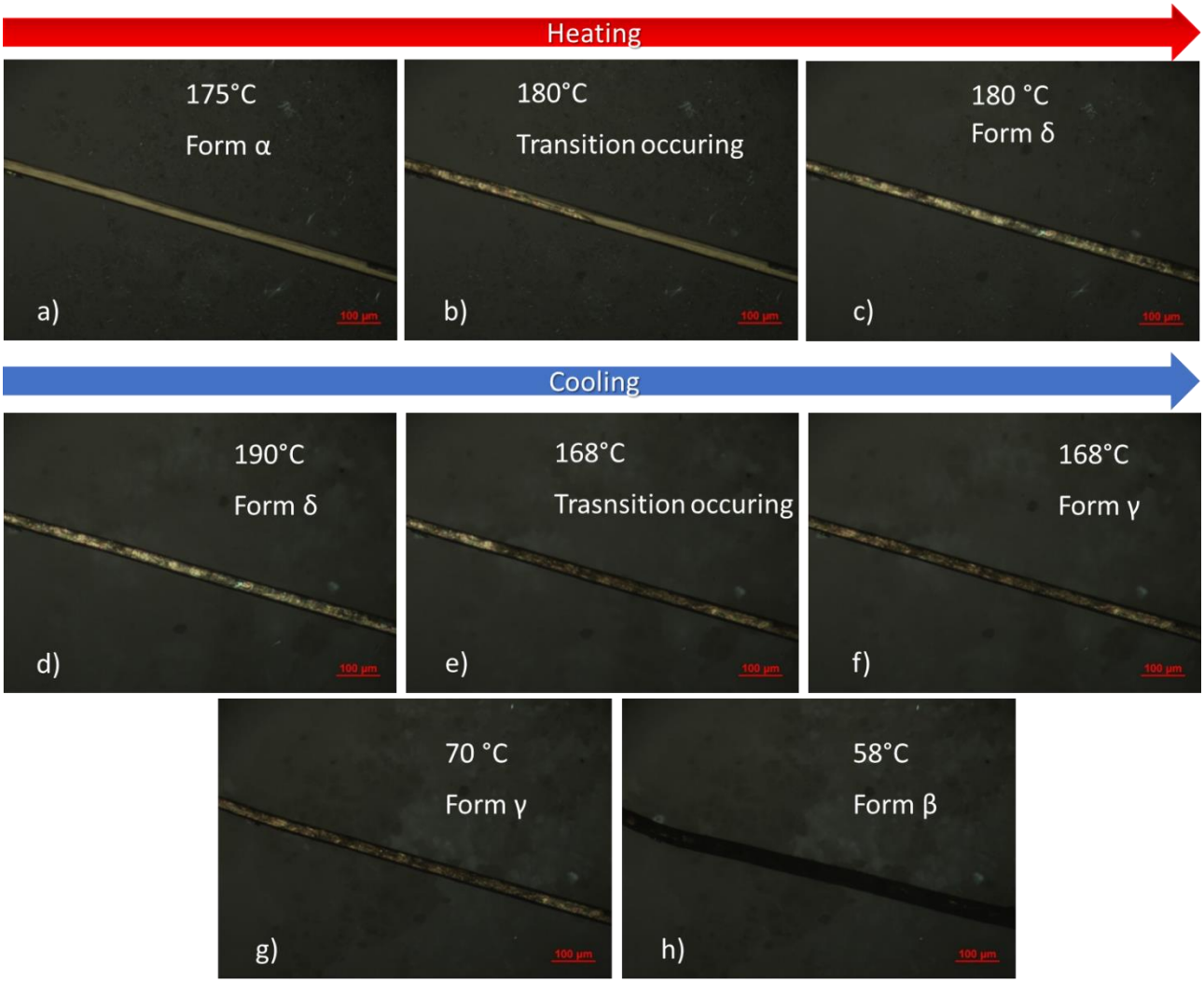

Figure S2 - Hot stage microscopy during the heating until before the melting of a single crystal NDI-C6, a) Form α at 175°C, b) Form α → Form δ transition starting at 180°C, c) transition into Form δ complete. Cooling starting from Form δ d) Form δ at 190°C, e) transition Form δ → Form γ occurring at 168°C, f) transition into Form γ complete, g) Form γ at 70°C, h) Form β at 58°C.

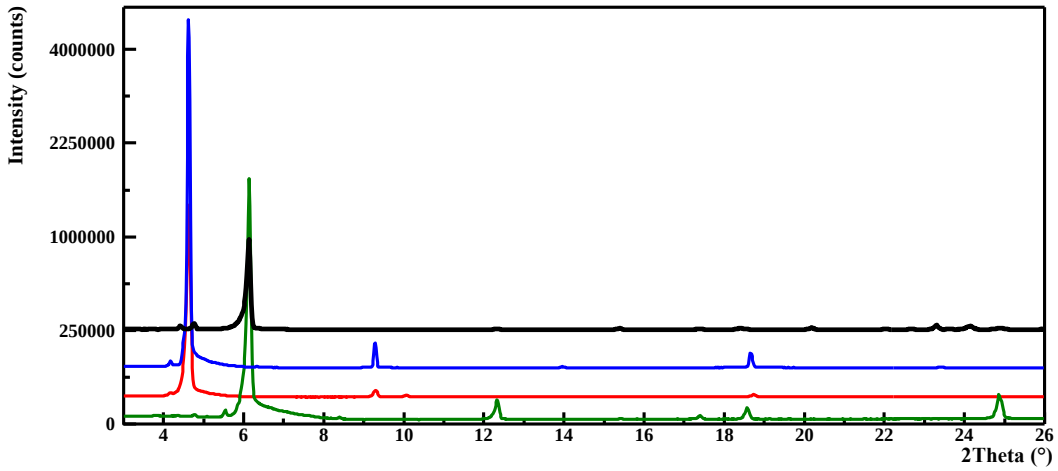

Figure S3 – VT-XRPD of NDI-C6, in green Form α at RT before heating, in red Form δ at 185°C before melting, in blue Form δ at 195°C at cooling after melt and in black Form α at RT after cooling from the melt.

More information about the transitions observed by DSC, such as temperature and enthalpy are summarized in Table S2.

Table S2 – Transitions observed in the DSC curves.

	Transition	Temperature (°C)	Enthalpy ($kJ.mol^{-1}$)
Without melting	Form α → Form γ Form γ → Form δ	178.7	15.7
	Form δ → Form γ	163.2	-9.6
	Form γ → Form β	56.4	-6.3
	Form β → Form γ	68.8	7.0
	Form γ → Form γ+α	100.3	-2.3
	Form α → Form γ Form γ → Form δ	176.7	15.7
With melting	Form α → Form γ Form γ → Form δ	178.2	14.9
	Form δ → Liquid	207.1	22.0
	Liquid → Form δ	204.7	-21.7
	Form δ → Form γ	164.9	-8.7
	Form γ → Form α	143.0	-3.6
	Form α → Form γ Form γ → Form δ	175.1	15.4
	Form δ → Liquid	207.0	21.9

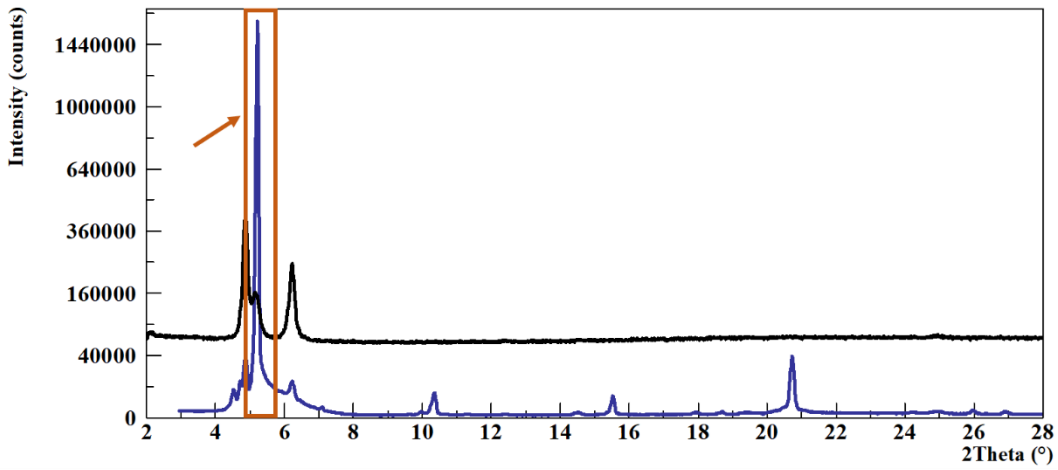

Figure S4 – Form ε on thin films produced with a DCM solution and Form ε obtained from quenching of the melt.

Table S3 – Cell parameters of Form α, Form β, Form γ and Form δ.

Form	**T_m (°C)**	**Lattice parameters**	**Volume (Å^3)**	**Space group**	**Z, Z'**	**Density (gcm^{-3})**	
Form α	RT	a=4.89482(5) Å b=8.2672 (2) Å c=14.5209 (1) Å α=96.293 (1)° β=98.064 (1)° γ=93.589 (2)°	577	P-1	1/0.5	1.25	Pawley refinement of the cell parameter of KEKJIU01
Form β	RT	a=22.855 Å (8) b=4.818 (1) Å c=32.052Å (2) α=90° β=91.833° (2) γ=90°	3528	P21	6/3	1.22	Pawley refinement of the cell parameter reported by Milita et al.
Form γ	54	a= 4.85556(6) Å b= 6.47166(7) Å c= 19.94656(13) Å α= 92.1464(13)° β= 95.834(2)° γ= 104.2269(12)°	603	P-1	1/0.5	1.20	Structure determination from Powder
Form δ	196.85	a=8.7946(1) Å b=8.0212(2) Å c=37.9396(4) Å α=90° β=90° γ=95.180(3)°	2665	$P112_1/b$	4/1	1.05	Pawley refinement of the cell parameter reported by Milita et al.

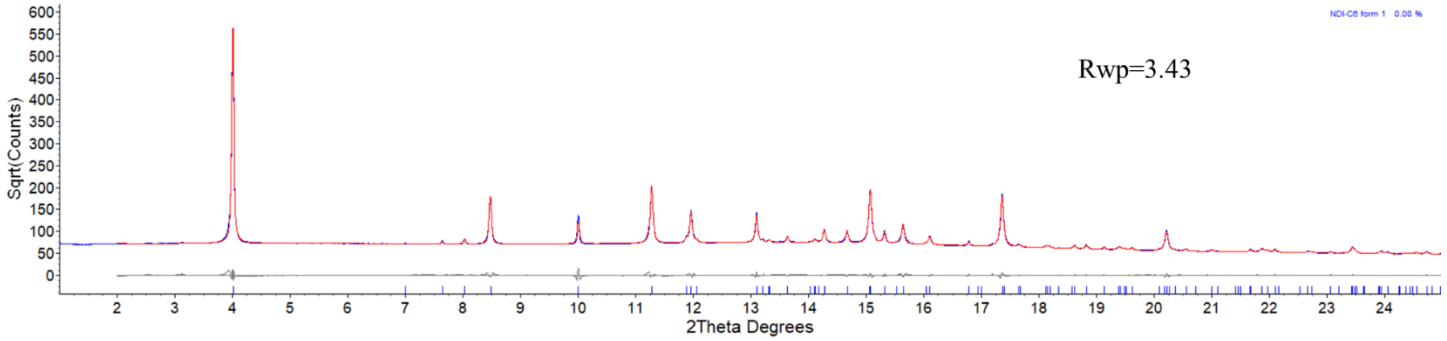

Figure S5 – Pawley Refinement of Form α at RT, with a Rwp of 3.43

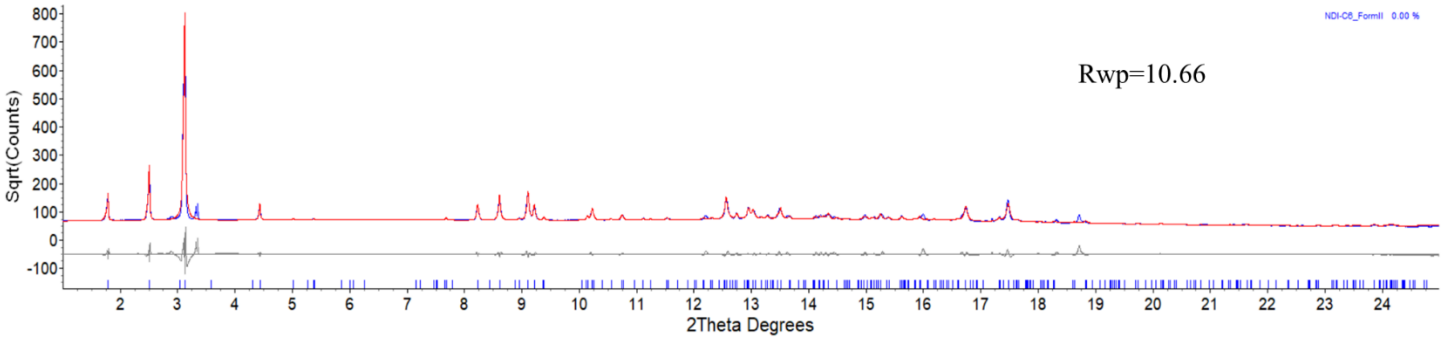

Figure S6 - Pawley Refinement of Form β at RT, with a Rwp of 10.66

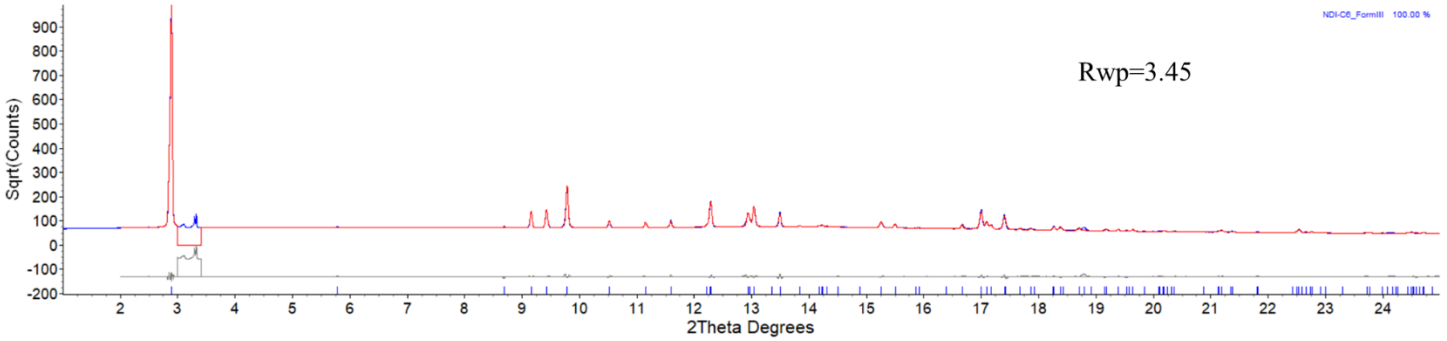

Figure S7 – Rietveld Refinement of Form γ at 54°C with a Rwp of 3.45, an interval of 2θ was excluded from the refinement since it was present peaks related to impurities.

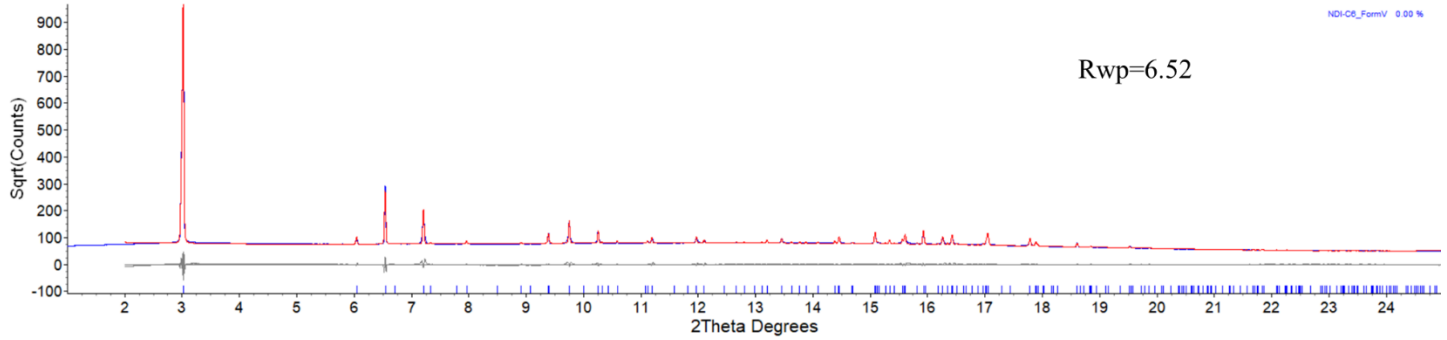

Figure S8 - Pawley Refinement of Form δ at 197°C, with a Rwp of 6.52

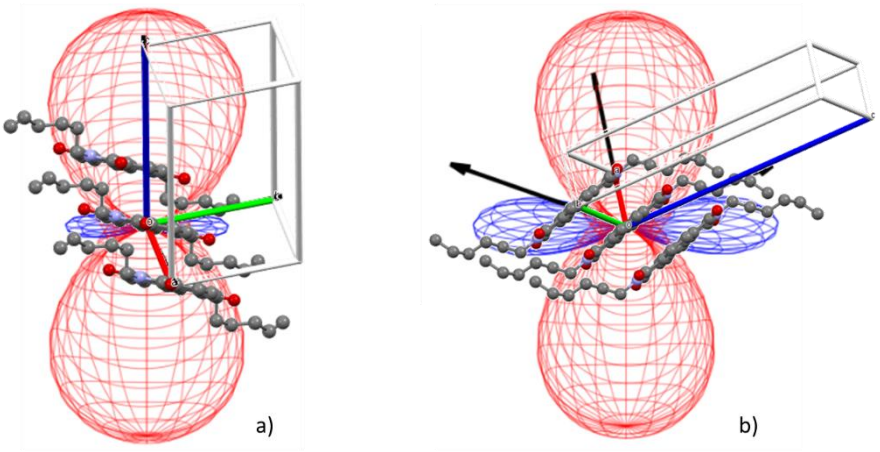

Figure S9 – Thermal expansion indicatrix with positive thermal expansion shown in red and NTE in blue. Crystal packing of each phase superimposed on the corresponding indicatrix to visualize the direction of the expansion regarding the crystal packing. a) Form α, b) Form γ.

Appendix B

Polymorph screening of core-chlorinated naphthalene diimides with different fluoroalkyl side chain lengths

Supplementary information

Table S1 - Summary of solubility assessment of CF_3-NDI, C_3F_7-NDI and C_4F_9-NDI

			Solubility (mg/mL)		
S. No	**Solvent**	**Abbreviation**	**CF_3-NDI**	**C_3F_7-NDI**	**C_4F_9-NDI**
1	Isopropanol	2PR	< 5	< 5	< 5
2	Acetonitrile	ACN	5	< 5	< 5
3	Acetone	ACT	10	20	5
4	Chloroform	CHF	< 5	< 5	< 5
5	Dichloromethane	DCM	< 5	5	< 5
6	Dimethylformamide	DMF	50	20	5
7	Dimethyl sulfoxide	DMSO	20	< 5	< 5
8	Ethyl acetate	ETA	5	10	5
9	Ethanol	ETH	< 5	< 5	< 5
10	Water	H2O	< 5	< 5	< 5
11	Methanol	MET	< 5	< 5	< 5
12	P-xylene	PXY	10	10	5
13	Tetrahydrofuran	THF	50	50	20
14	Toluene	TOL	10	10	5

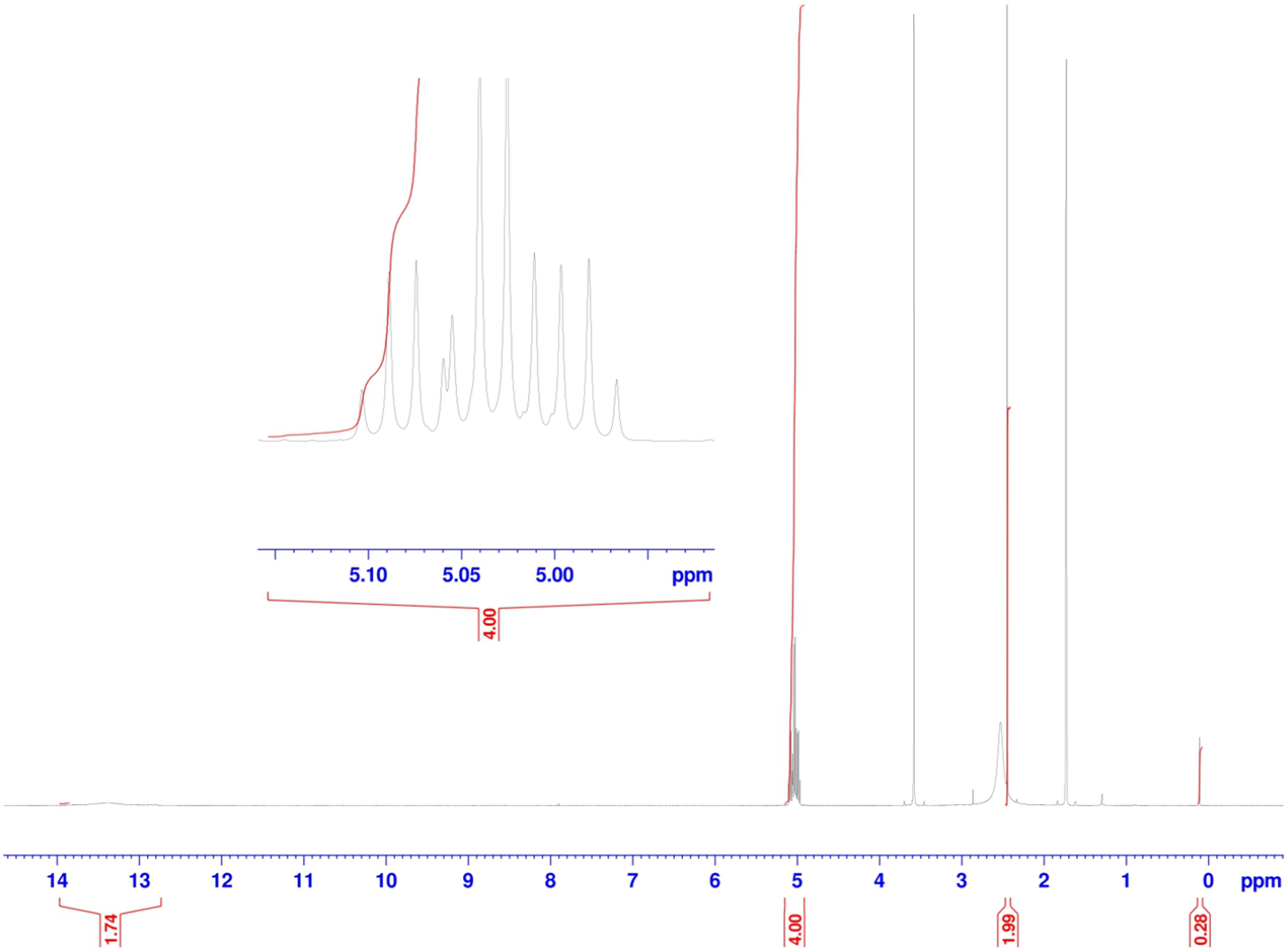

Figure S1 - H-NMR of CF_3-NDI•SS.

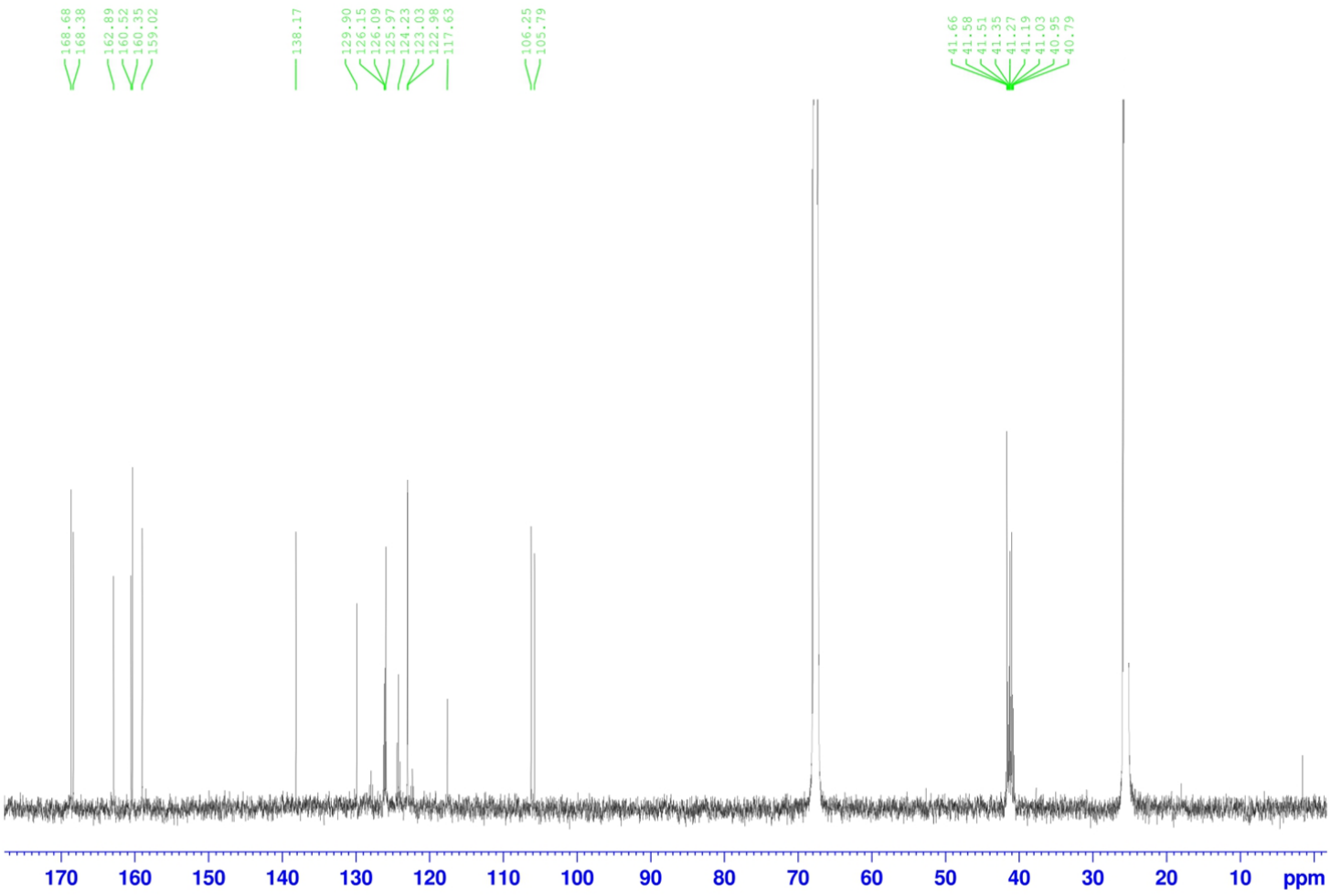

Figure S2 - C-NMR of CF3-NDI•SS.

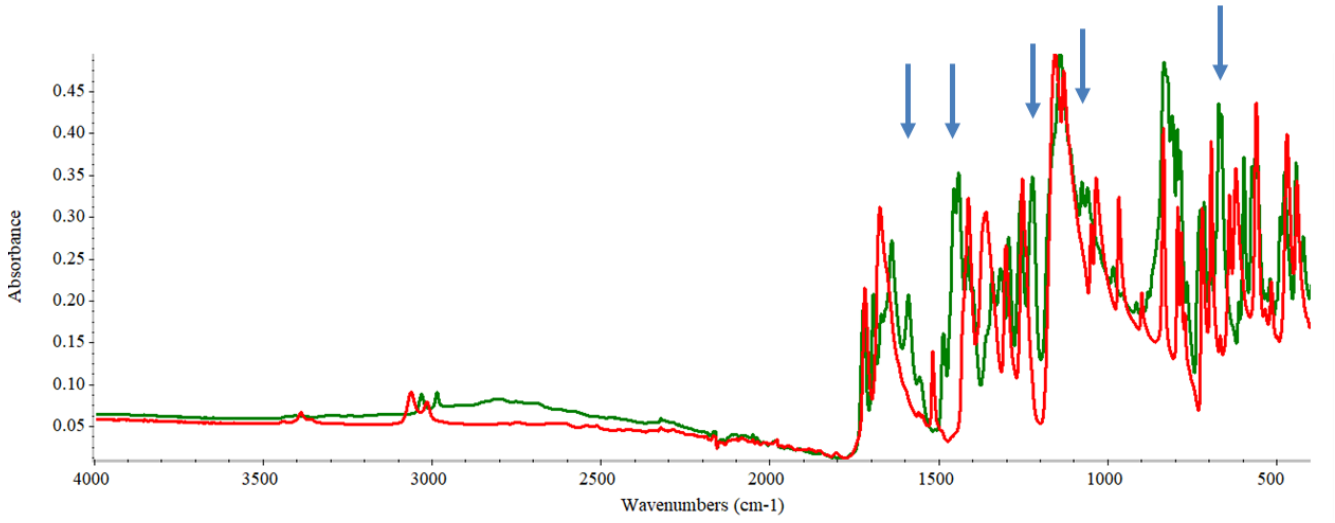

Figure S3 - FTIR of CF_3-NDI•Form I in red and CF_3-NDI•SS in green.

Table S2 - Packing parameters for all the crystal forms

	CF_3-NDI•Form I	CF_3-NDI•SS	CF_3-NDI•PXY	C_3F_7-NDI•Form I	C_4F_9-NDI•Form I
π-π stacking	3.413	3.277	3.395	3.423	3.401
Stacking vector	4.872	5.835	7.780	5.104	5.505
χ	74.92	75.66	46.41	72.77	78.53
ψ	49.37	38.39	55.22	48.44	40.88
Δx	1.268	1.445	5.364	1.512	1.095
Δy	3.173	4.573	4.438	3.386	4.162
Pitch	20.38	23.80	57.67	23.83	17.85
Roll	42.91	54.37	52.58	44.69	50.75
Torsion angle	0.69	0.15	1.07	7.2	1.5

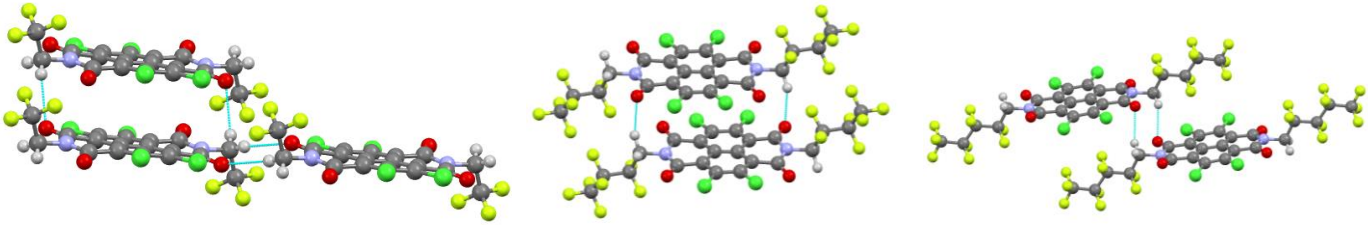

CF_3-NDI•Form I C_3F_7-NDI•Form I C_4F_9-NDI•Form I

Figure S4 - O--H interactions of Form I (thermodynamic stable form) of each molecule.

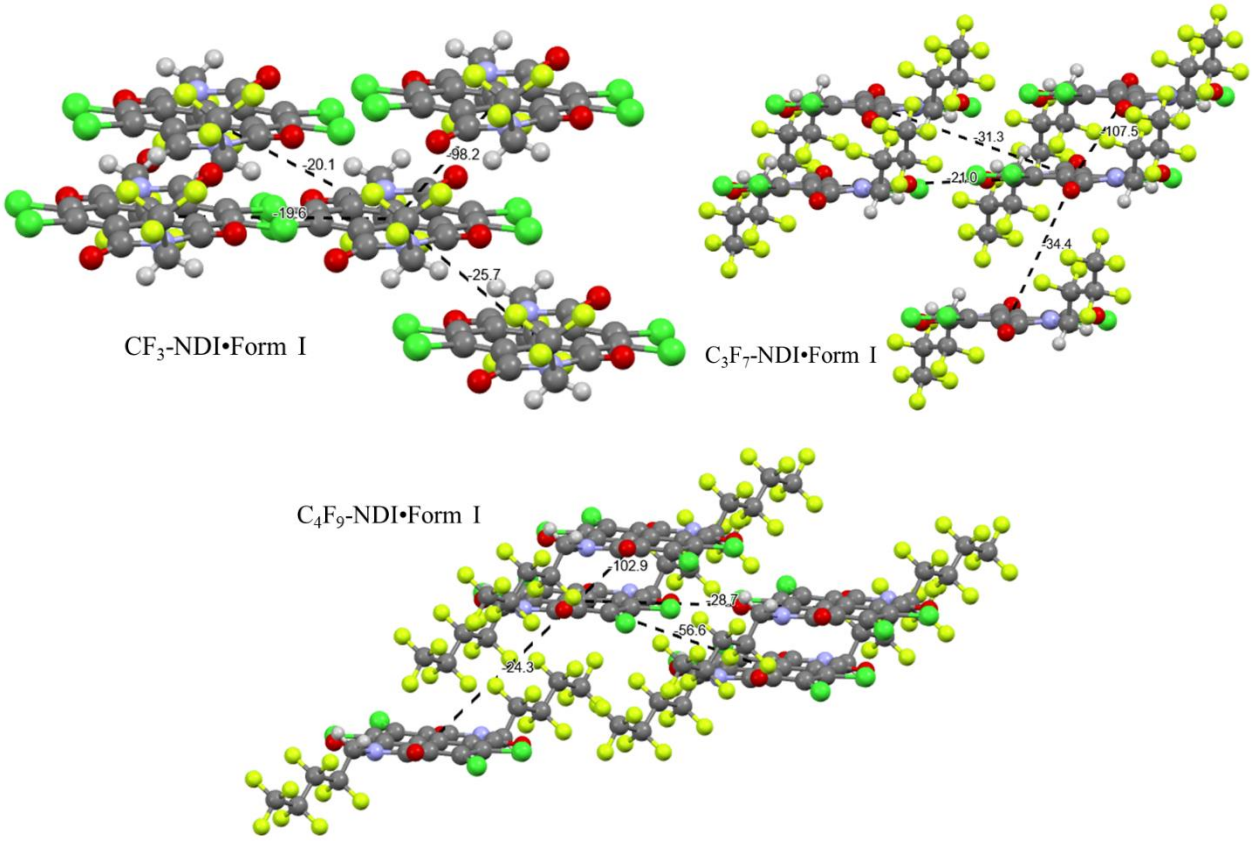

Figure S5 - Intermolecular potentials of CF_3-NDI•Form I, C_3F_7-NDI•Form I and C_4F_9-NDI•Form I

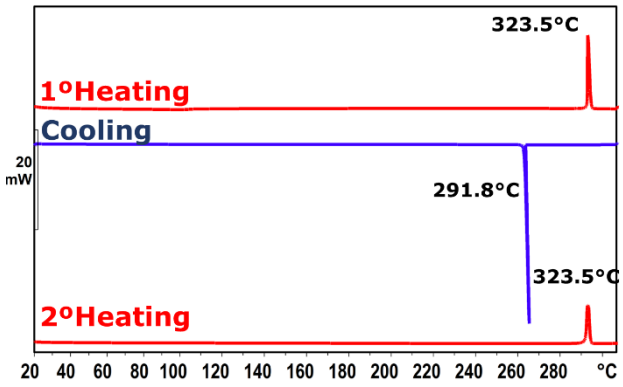

Figure S6 – DSC curves of CF_3-NDI•Form I, first heating (red line), cooling (blue line) and second heating (red line)

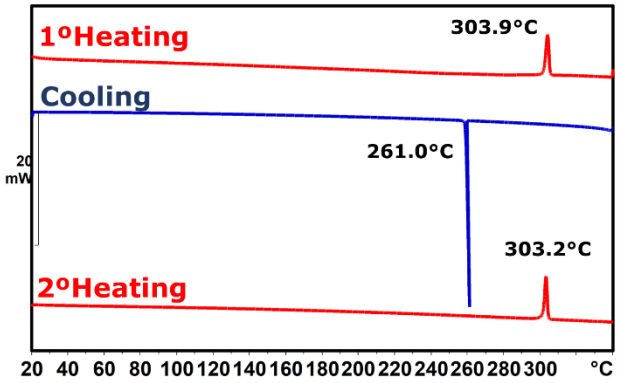

Figure S7 - DSC curves of CF_3-NDI•SS, first heating (red line), cooling (blue line) and second heating (red line)

Table S3 – Unit-cell parameters used as input for the PASCal calculation, obtained by Pawley refinement of the reported cell of C_3F_7-NDI•Form I at different temperatures.

Temperature (°C)	a (Å)	b (Å)	c (Å)	α (°)	β (°)	γ (°)
20	5.143578	10.49287	12.27007	112.1219	89.82593	97.03933
30	5.147791	10.50615	12.29644	112.1659	89.88528	97.03637
40	5.151659	10.51916	12.32627	112.2165	89.96531	97.02838
50	5.155901	10.52464	12.35416	112.247	90.01383	97.06119
60	5.161186	10.52294	12.39038	112.2709	90.0308	97.09506
70	5.16428	10.5062	12.46002	112.3641	89.97152	97.0008
80	5.168586	10.51111	12.50245	112.4523	89.99693	96.98892
90	5.171762	10.53045	12.52874	112.5727	90.11031	96.97994

Table S4 - Values (α_X) of the principal axis of thermal expansion (X1, X2 and X3) and their orientation in regards of the cell axis, a, b and c of C_3F_7-NDI•Form I

	Principal axis	α_X (MK^{-1})	a	b	c
Form I	X1	-11	0.7595	0.6002	0.2508
	X2	72	-0.9483	0.3169	-0.0179
	X3	320	-0.5319	0.0234	0.8465
	Volume	**383**			

Table S5 - Unit-cell parameters used as input for the PASCal calculation, obtained by Pawley refinement at different temperatures of the reported cell of C_4F_9-NDI•Form I.

Temperature (°C)	a (Å)	b (Å)	c (Å)	α (°)	β (°)	γ (°)
35.57941	5.55044	9.93215	13.27935	84.50596	99.43067	93.4246
38.80761	5.55125	9.93251	13.29235	84.43997	99.43392	93.43442
40.25474	5.5537	9.93269	13.3123	84.34762	99.4414	93.4711
47.26773	5.55599	9.93501	13.32761	84.2437	99.48624	93.49953
51.16383	5.55738	9.93803	13.34715	84.13745	99.49429	93.52905
50.49593	5.55899	9.93986	13.35905	84.07418	99.50869	93.54646
57.62024	5.56023	9.94343	13.37973	83.95292	99.51904	93.56005
59.40132	5.56174	9.9436	13.39068	83.89847	99.52992	93.57307
60.18054	5.56325	9.94374	13.40381	83.83398	99.53743	93.58894
65.96904	5.56559	9.94565	13.42297	83.73449	99.54974	93.61299
72.42544	5.56848	9.94672	13.44029	83.63698	99.5554	93.64258
72.31412	5.5699	9.94783	13.45069	83.58394	99.5606	93.65531
73.64993	5.57119	9.94846	13.46332	83.52425	99.56049	93.66212
77.43472	5.5743	9.9488	13.47989	83.44244	99.56597	93.69081
83.1119	5.57689	9.95035	13.49896	83.35051	99.57873	93.70905
89.23436	5.57957	9.95042	13.51438	83.28088	99.58314	93.73378
92.90783	5.58279	9.95115	13.52492	83.22739	99.59289	93.75406
95.80208	5.58442	9.9514	13.5347	83.17749	99.59059	93.76532
96.24735	5.58659	9.95117	13.54601	83.12474	99.58734	93.77783
97.13789	5.58933	9.95138	13.55826	83.07184	99.60114	93.79394
99.69819	5.59174	9.95141	13.57107	83.01267	99.59891	93.8059
104.4848	5.59519	9.95217	13.5845	82.94193	99.6031	93.82765
109.8281	5.59866	9.953	13.59779	82.87786	99.61348	93.84634
111.4978	5.60236	9.95204	13.61034	82.8244	99.62449	93.8614
116.6184	5.60575	9.95263	13.62184	82.76433	99.62571	93.87964
121.8503	5.609	9.95237	13.63489	82.71217	99.62403	93.88856
124.8559	5.61269	9.95225	13.64231	82.66795	99.63309	93.91095
129.8652	5.61642	9.95325	13.65441	82.60946	99.63579	93.92672
134.6518	5.61983	9.95149	13.66493	82.57168	99.64384	93.93602
137.7687	5.6229	9.95131	13.67591	82.52417	99.64643	93.95435

140.2177	5.62678	9.95012	13.68569	82.47873	99.65099	93.9689
139.6611	5.63036	9.9506	13.69697	82.43508	99.65488	93.98683
145.4496	5.63577	9.94914	13.71481	82.36953	99.66174	93.9994
148.1212	5.63828	9.94893	13.72096	82.34432	99.66715	94.00891
150.7928	5.64139	9.94871	13.72836	82.31692	99.67587	94.02017
155.1342	5.64504	9.94775	13.73995	82.26837	99.67301	94.02953
158.5851	5.65072	9.94767	13.7512	82.218	99.68681	94.05135
161.9246	5.6558	9.94564	13.76317	82.17584	99.69628	94.06457
164.7075	5.65944	9.94546	13.77296	82.14126	99.69984	94.07167
168.047	5.66337	9.94361	13.78198	82.10692	99.7094	94.07307
171.4979	5.66739	9.94352	13.79003	82.07373	99.71795	94.08217
175.1713	5.67112	9.94311	13.80125	82.0341	99.72535	94.08951
178.8448	5.67566	9.94221	13.81013	82.00232	99.72394	94.10217
181.9617	5.67973	9.94134	13.82082	81.96576	99.73347	94.1117
185.3012	5.6843	9.93906	13.83113	81.93652	99.74681	94.12299
188.5294	5.68788	9.93652	13.84132	81.89949	99.75237	94.12273
191.8689	5.69264	9.93601	13.85055	81.87355	99.76381	94.13089
195.6537	5.69672	9.93551	13.86058	81.83884	99.76954	94.14067
198.3253	5.70164	9.93235	13.87191	81.81491	99.76856	94.14988
202.1101	5.70578	9.931	13.88163	81.78914	99.7885	94.14998
205.6723	5.71056	9.92937	13.89265	81.75188	99.79846	94.15199
209.1231	5.71493	9.92765	13.90124	81.73048	99.80356	94.1571
212.24	5.7192	9.92687	13.91047	81.70107	99.8178	94.15741
215.4682	5.72351	9.92466	13.91885	81.67752	99.82879	94.1553
219.3643	5.72785	9.92162	13.93009	81.66468	99.84028	94.15657
222.8151	5.73302	9.91981	13.94274	81.6316	99.85197	94.15606
225.4868	5.73763	9.91723	13.95345	81.61904	99.85849	94.16447
229.2716	5.74174	9.91592	13.96255	81.58477	99.86208	94.15742
232.3884	5.74719	9.91356	13.97316	81.56326	99.87138	94.16951
235.8393	5.75169	9.90879	13.98753	81.55754	99.90492	94.1468
239.1788	5.75709	9.90671	14.00028	81.52773	99.90937	94.15149
243.0749	5.76202	9.90431	14.01019	81.50965	99.91215	94.15186
246.5257	5.76613	9.90308	14.0206	81.48496	99.92325	94.15633
249.6426	5.77044	9.89981	14.03033	81.47404	99.92389	94.15295
252.9821	5.77618	9.89172	14.05048	81.49136	99.96722	94.10425

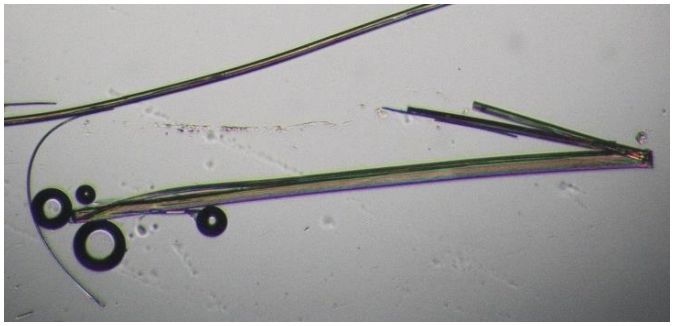

Figure S8 -Desolvation of C_3F_7-NDI•ACN

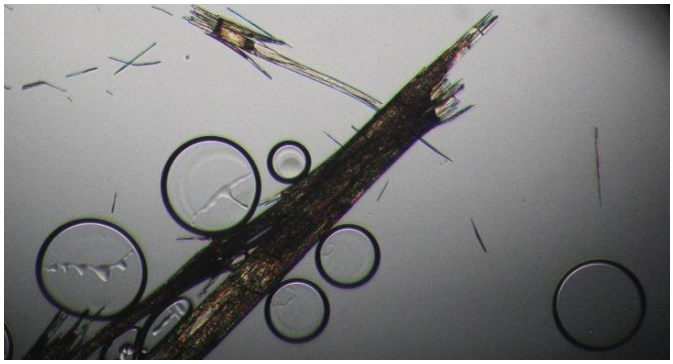

Figure S9 - Desolvation of C_4F_9-NDI•ACN